MULTI-FREQUENCY RADAR STUDIES OF THE HIGH LATITUDE MESOSPHERE

A Dissertation

Presented to the Faculty of the Graduate School

of Cornell University

in Partial Fulfillment of the Requirements for the Degree of

Doctor of Philosophy

by

Camilo Ramos

January 2007

MULTI-FREQUENCY RADAR STUDIES OF THE HIGH LATITUDE MESOSPHERE

Camilo Ramos, Ph.D.

Cornell University 2007

The radar signature of Polar Mesosphere Summer Echoes (PMSE), which are associated with Noctilucent Clouds (NLC) (the highest clouds over the Earth), has been studied using Medium-Frequency (MF), High-Frequency (HF), and Very-High-Frequency (VHF) radars deployed over the central Alaskan region. The echo morphology at the different frequencies is described in case studies wherein PMSE events were observed concurrently using at least two radar systems. The identity of MF and HF radar echoes as PMSE is resolved for the first time by means of simultaneous measurements made with VHF radars, the reference sensors employed traditionally for PMSE studies. Radar reflectivity estimates, derived from in-situ rocket measurements, suggest that HF radars are optimal for the observation of PMSE edge-dominated type of scatter. MF radars, on the other hand, show comparable reflectivity values for edge and turbulent scattering components, as may be expected for wider antenna beam systems that are exposed to other echo sources. The VHF scattering calculations validate previous research on PMSE, suggesting an increase of the Schmidt number to maintain irregularities of scale sizes in the order of a few meters or less. A large Schmidt number is not needed at MF/HF frequencies since the wavelengths are larger than the Kolmogorov micro-scale and mesospheric layers can be sustained at low charging levels. Rocket measurements

of mesospheric dust content and simultaneous analyzed MF radar backscattered power profiles show a similar type of structure. Dust particles are produced most likely by meteor trails reaching to the upper mesosphere region and may be related to some non-summer Mesospheric-radar Echoes (ME). On the basis of echo duration and signal strength, we suggest that HF radars are most favorable for PMSE monitoring. MF radars show highly organized PMSE layers quite often but are more susceptible to ionospheric absorption and higher altitude returns associated with geomagnetic activity. However, since a number of MF stations are located at polar or near polar latitudes, including Antarctica, it may be possible to use the PMSE signature studied here to investigate its long-term variability as well as its low latitude boundary. The latter could be an indicator of global change.

BIOGRAPHICAL SKETCH

Camilo Ramos was born in Aibonito, Puerto Rico. He attended public schools in the town of Barranquitas and the University of Puerto Rico in Mayagüez (UPRM), where he obtained Bachelor's and Master's degrees, both in Electrical Engineering, in 1996 and 1998, respectively. After graduating from UPRM, he moved to Boston, Massachusetts, where he worked for Raytheon Systems Company (Northeast Systems Engineering Center, Radar Systems Integration Department) between 1998 and 2000. In 2001, he began graduate studies in Electrical and Computer Engineering at Cornell University (Space Physics and Engineering Group) in Ithaca, New York. For about four years he conducted ionospheric research at the High Power Auroral Stimulation (HIPAS), Poker Flat Research Range (PFRR), and High Frequency Active Auroral Research Program (HAARP) radar facilities in Alaska, completing his PhD degree in December 2005.

To the Inuit, Yupik, Eskimos, Aleuts, and all the Alaska Native American pueblos.

ACKNOWLEDGEMENTS

I would like to thank all the technical staff at the High Power Auroral Stimulation (HIPAS) and High Frequency Active Auroral Research Program (HAARP) facilities for assisting me during all my research trips to Alaska. Special mentions to Eric Nichols, Mike McCarrick, Marty Karjala, David Seafolk-Kopp, and Troy Lawlor. Similarly, I am grateful to the Geophysical Institute of the University of Alaska in Fairbanks and the National Institute of Information and Communications in Japan for all the scientific collaboration they provided. Much gratitude is given to Tom Blix, from the Defense Research Establishment in Norway, and Lynette Gelinas, from the Aerospace Corporation, for providing rocket data. Thanks go to Chris Meek and Alan Manson from the University of Saskatchewan in Canada for kindly providing me Platteville MF radar data. Appreciation also goes to Professors Donald Farley and Wesley Swartz, from Cornell, and Frank Djuth and John Elder, from Geospace Research Inc., for all their technical advice on radars and signal processing. Thanks also is due to Laurie Shelton and Jamie Dal Cero for all their constant support while I was in Ithaca and abroad. To Professor Michael Kelley thanks for being an excellent advisor, great scientist, and for all the many travel opportunities, resources, support, and continuous interest in my research. To my advisor at UPRM Professor Mario Ierkic who stimulated me to become interested in the fields of radars and aeronomy, and taught me digital signal processing, scientific programming, and many other interesting areas. To all my colleagues at Raytheon, friends, and classmates at UPRM and Cornell thank you. Finally, to Papi, Mami, and my sister Idalia for advising, stimulating, and being the best examples for me.

The research work was sponsored by the Office of Naval Research under Grant N00014-00-1-0658.

TABLE OF CONTENTS

1 Introduction **1**

2 Polar Mesosphere Summer Echoes **9**
2.1 Why do we study the Polar Summer Mesosphere? 9
2.2 Historical Review of PMSE 15
2.3 Summary of Radar Observations 18
2.3.1 General Features 18
2.3.2 Other Frequency and Multi-instrument Observations 20
2.4 Theories for PMSE 22
2.4.1 VHF 23
2.4.2 UHF 25
2.4.3 Latest Developments in PMSE Research 26

3 Radar Facilities and Observations of PMSE **28**
3.1 Alaskan Radar Facilities for PMSE Studies 28
3.2 Radar Configurations and Data Sets 31
3.2.1 Poker Flat Medium Frequency Radar 31
3.2.2 HIPAS 33
3.2.3 HAARP 34
3.3 PMSE at MF/HF/VHF 37
3.3.1 Preliminary MF and HF Work 37
3.3.2 Winter/Summer Comparisons 39
3.3.3 Climatology Studies of PMSE 42
3.3.4 Multi-frequency Observations: Case Studies 52
3.4 Summary 61

4 Radar Scattering Predictions from Rocket Soundings **65**
4.1 Radar Scattering Theory 65
4.1.1 The Radar Equation 66
4.1.2 Turbulent Scatter 68
4.1.3 Edge Scatter 73
4.2 Rocket Data Analysis 78
4.2.1 Non-Summer: DYANA Campaign 79
4.2.2 Summer: MAC/SINE Campaign 79
4.2.3 Differences between the Non-summer and Summer Rocket Measurements 81
4.3 Wavelet Decomposition and Edge Reconstruction of Electron Density 82
4.4 Radar Reflectivity Calculations 87
4.4.1 Turbulent Scatter 87
4.4.2 Edge Scatter 87
4.5 Summary 89

5 On a Possible Relationship Between Mesospheric Dust and Medium Frequency (MF) Radio Scatter **91**
5.1 Radio Scattering at Medium Frequencies . . . 91
5.2 Mesospheric Dust Layers . . . 94
5.3 Radar and Rocket Observations of Mesospheric Dust . . . 94
5.4 The Dust Effect at MF/HF/VHF . . . 96
5.5 A Possible Explanation for the Dust Radar Mechanism . . . 101
5.6 Summary . . . 103

6 Discussion **104**
6.1 Multi-Frequency Radar Studies of Icy/Dusty Plasmas . . . 104
6.2 Scattering Estimation . . . 105
6.3 Dust Phenomena . . . 110
6.4 Climate Change, Radar Remote Sensing, and the Importance of Mesospheric Ice/Dust Research . . . 111

7 Conclusions and Future Work **113**

Appendices **118**
A.1 Radar Analysis and Mesospheric Observation System (RAMOS) . . 118
A.1.1 HF Radars at HIPAS and HAARP . . . 118
A.1.2 Data Acquisition System . . . 123
A.1.3 HF Radar Data Format . . . 132
A.1.4 An Example of a Data Collection Sequence . . . 132
A.1.5 HAARP HF Receiver . . . 134
A.2 Radar/Rocket Data Inventory . . . 139
A.3 Radar Equation Derivation . . . 144
A.3.1 Small (Point) Target . . . 144
A.3.2 Turbulent Scatter . . . 145
A.3.3 Edge or Fresnel Scatter . . . 146
A.4 Reflection Coefficient Derivation . . . 149
A.5 Rocket Wavelet Analyses . . . 152
A.6 Radar Reflectivity Estimates . . . 162

Bibliography **171**

LIST OF TABLES

3.1 System Parameters for the Alaskan HF Facilities. 30

6.1 Predicted radar reflectivity values for 85 km derived from non-summer (DYANA) and summer (MAC/SINE) rocket measurements of electron density. 109

7.1 Overview of PMSE observational research during the last 25 years and sample references. 116

A.1 Graphical-User-Interface (GUI) input fields for HF data acquisition 127

A.2 HF Header Data Structure 131

A.3 HF I/Q Data Format 133

A.4 Data size calculation for parameters listed in Table A.2 133

A.5 Radar Databases/Summer 2002 140

A.6 Radar Databases/Summer 2003 141

A.7 Radar Databases/Winter 2004 142

A.8 Rocket Databases 143

A.9 DYANA Rocket Analyzed Data 152

A.10 MAC/SINE Rocket Analyzed Data 153

LIST OF FIGURES

1.1 Long-term mesospheric radar observations at Poker Flat. Adapted from Ecklund and Balsley [1981]. 2

2.1 Noctilucent Clouds (NLC) © Pekka Parviainen. Adapted from: *http://lasp.colorado.edu/noctilucent_clouds*. 11
2.2 Polar Summer versus Polar Winter Mesosphere. Adapted from Lübken and von Zahn [1991]. 11
2.3 Global circulation driven by gravity waves. Adapted from Holton [1983]. 13
2.4 Power spectrum of refractive index fluctuations in a turbulent atmosphere. Approximate locations (in k-space) for Medium-Frequency (MF), High-Frequency (HF), and Very-High-Frequency (VHF) radar frequencies are superimposed. Adapted from Craig [2002]. 16
2.5 Polar and non-polar rocket spectra. The vertical dashed lines indicate Bragg scales for 2.5 MHz (MF), 5 MHz (HF), and 50 MHz (VHF) radar frequencies. Adapted from [Ulwick et al., 1988] (left), [Blix, 1988] (middle), and [Røyrvik and Smith, 1984] (right). 17
2.6 Radar and rocket concurrent observations during PMSE. Adapted from Kelley and Ulwick [1988]. 19
2.7 Concurrent lidar and radar observation. The lower dark patch, at around 83 km, shows the NLC/lidar scattering region that is coincident with the bottom part of the PMSE/radar echoes. Adapted from von Zahn and Bremer [1999]. 21

3.1 The Alaskan Radar Facilities. 29
3.2 Coherent Backscatter Radars at HIPAS and Poker Flat, Alaska. . . 31
3.3 Coherent Backscatter Radars at HAARP. 32
3.4 PMSE observations at multiple frequencies using the HAARP HF Facility [August 5, 2000]. 36
3.5 Concurrent radar observations at (a) Poker Flat (MF/2.43 MHz) and (b) HIPAS (HF/4.53 MHz) [July 6, 2001; 18:30-20:30 UT]. The solar geomagnetic index was reported as $k_p = 2$ for the same interval of time. 38
3.6 Concurrent MF radar observations over (a) Poker Flat, Alaska, and (b) Platteville, Colorado [July 14, 2002; 16:00-24:00 UT]. 40
3.7 (a) HF/4.9 MHz radar mesospheric backscattered signal versus altitude for summer and non-summer periods, (b) Same inter-seasonal comparison but at MF/2.43 MHz. 41
3.8 Typical MF radar power profiles for (a) summer and (b) non-summer periods [July 13, 2002 and January 13, 2002; 12:00-24:00 UT]. 43

3.9 (a) Long-term distribution of MF radar mesospheric echoes (or "power peaks") over Poker Flat, Alaska [January 1, 2002 - January 1, 2004], (b) Similar analysis but at VHF [Ecklund and Balsley, 1981]. 45
3.10 Seasonal distribution of zonal wind (top panel) and meridional wind (bottom panel) versus altitude over Poker Flat, Alaska, for year 2002. Eastward and northward winds are indicated by positive values. 47
3.11 Concurrent radar observations at (a) Poker Flat (MF/2.43 MHz) and (b) HIPAS (HF/4.53 MHz). Each power profile represents the mean of a 2-hour data segment (19-21 UT). The mean power profile for each seasonal database is plotted as a dashed line in both panels. 49
3.12 Diurnal MF backscattered power (top panel) and HF signal-to-noise ratio (bottom panel) for (a) Poker Flat and (b) HIPAS [July 29/30, 2002, 18-18 UT]. 51
3.13 Concurrent HF/VHF radar observations at HAARP [July 29, 2003; 18:00-19:00 UT]. 54
3.14 Poker Flat imaging riometer [July 29, 2003, 18:00-20:00 UT]. . . . 55
3.15 Concurrent HF/VHF radar observations at HAARP [July 14, 2003, 18:00-19:00 UT]. 56
3.16 Concurrent HF/VHF radar observations at HAARP [July 16, 2003, 21:00-23:00 UT]. 57
3.17 (a) MF/2.43 MHz and HF/4.53 MHz radar observations during high k_p conditions [June 18, 2002, 19:00-21:00 UT], (b) Average power profiles for 15-minute data segments centered at 19:10, 19:40, 20:10, and 20:40 UT. 59
3.18 PMSE observed at three frequencies: 2.43/4.9/139 MHz [July 03, 2003, 18:00-20:00 UT]. 60
3.19 Poker Flat imaging riometer [July 03, 2003, 18:00-20:00 UT]. . . . 61
3.20 Zonal and meridional mesospheric winds over Poker Flat [July 03, 2003; 18:00-20:00 UT]. 62
3.21 PMSE observed at three frequencies: 2.43/50/139 MHz [July 13, 2003; 01:30-02:30 UT]. 63
3.22 PMSE observed at three frequencies: 2.43/50/139 MHz [July 13, 2003; 23:00-01:00 UT]. 64

4.1 Power spectrum of refractive index fluctuations in a turbulent atmosphere. Adapted from Craig [2002]. 69
4.2 Mathematical and graphical representation for a typical radio scatterer in clear air. 72
4.3 a) Slab geometry of refractive index and reflection coefficient for two mediums of different refractive indices, n_1 and n_2, b) Reflection coefficient and refractive index profiles for slab geometry shown in a). Adapted from Hocking [2002]. 74

4.4 Reflected complex amplitude for a single step of refractive index. The two left panels show refractive index, reflection coefficient, and radar pulse variations in space or z-domain. The right panel shows a representation of the refractive index and radar pulse in inverse space or k-domain. 77
4.5 Rocket flights representing (a) non-summer and (b) summer mesospheric conditions. Fourier analysis performed on non-summer and summer electron density data, (c) and (d), respectively. Overplotted in (b) is shown radar reflectivity data collected simultaneously with the Sousy/53.5 MHz radar. 80
4.6 Wavelet analysis applied to a non-summer rocket data segment. The top panel shows de-trended electron density versus altitude. The bottom panel shows a Wavelet scalogram obtained for the data segment in the upper panel. 83
4.7 Wavelet analysis applied to a summer rocket data segment using the format of Figure 4.6. 84
4.8 Radar reflectivity, η_{turb} and η_{edge}, versus wavenumber, k, for (a) non-summer and (b) summer, and three different altitudes: 83, 84, and 85 km. The Driscoll and Kennedy model for turbulent reflectivity is superimposed for $S_c = 1$ on the left and $S_c = 100$ on the right. 90

5.1 Predicted power reflection coefficient profile for an MF/2.5 MHz radar derived from in-situ data collected during summer (MAC/SINE rocket). A sample MF power profile measured at Poker Flat (June 18, 2002, 19-21 UT) is over-plotted for comparison purposes. 92
5.2 Radar and rocket concurrent observations of MF power and charged dust density, respectively, over Poker Flat, Alaska (NASA Rocket Campaign, March 2002). 95
5.3 Dust peak profiles and MF power/radar history for (a) March 07, 2002; 08-16 UT, and (b) March 15, 2002, 08-16 UT, at Poker Flat, Alaska. 97
5.4 Typical summer and non-summer backscattering profiles for the (a) Poker Flat MF/2.43 MHz, (b) HAARP HF/4.9 MHz, and (c) Poker Flat VHF/50 MHz radars. The VHF results were adapted from Ecklund and Balsley [1981]. 99
5.5 Scattering model for turbulence fluctuations as a function of wavenumber or radar frequency. Two Schmidt numbers are displayed: $S_c = 1$ and $S_c = 100$. Adapted from Driscoll and Kennedy [1985]. 102

6.1 Received power reduction (P_{rN}) for N scattering elements smaller than 1-Fresnel zone. 106

6.2 Predicted radar reflectivity, η_{turb} and η_{edge}, versus wavenumber, k, for (a) non-summer and (b) summer periods. The Driscoll and Kennedy model for turbulent reflectivity is superimposed for S_c = 1/Non-summer and S_c = 100/Summer. 108

A.1 HIPAS HF Radar Receiver Setup 119
A.2 The HIPAS HF Receiving Station 120
A.3 HAARP HF Radar Receiver Setup 121
A.4 The HAARP HF Receiving Station 122
A.5 MATLAB® GUI for HF data acquisition [C. Ramos/2003] 128
A.6 Timing diagrams for HF radar transmissions 129
A.7 Input/Output Connector Pin Assignment for the PCI-6110E digitizer/card. Adapted from *PCI-6110E/6111E User Manual*, National Instruments Corporation, 1998. 130
A.8 La Salle HF Receiver Overview [Personal Communication with John Brosnahan, 2003] 138
A.9 The radar equation for a small (point) target 145
A.10 The radar equation for edge scatter 148
A.11 Normalized power reflection coefficient as a function of scale size for an edge of electron density centered at the radar range window. λ is the radar Bragg length. 151
A.12 DYANA Electron Density and Wavelet Scalogram: (a) 81 km, (b) 82 km 154
A.13 DYANA Electron Density and Wavelet Scalogram: (a) 83 km, (b) 84 km 155
A.14 DYANA Electron Density and Wavelet Scalogram: (a) 85 km, (b) 86 km 156
A.15 DYANA Electron Density and Wavelet Scalogram: (a) 87 km, (b) 88 km 157
A.16 MAC/SINE Electron Density and Wavelet Scalogram: (a) 81 km, (b) 82 km 158
A.17 MAC/SINE Electron Density and Wavelet Scalogram: (a) 83 km, (b) 84 km 159
A.18 MAC/SINE Electron Density and Wavelet Scalogram: (a) 85 km, (b) 86 km 160
A.19 MAC/SINE Electron Density and Wavelet Scalogram: (a) 87 km, (b) 88 km 161
A.20 Radar reflectivity versus wavenumber for DYANA: (a) 81 km, (b) 82 km 163
A.21 Radar reflectivity versus wavenumber for DYANA: (a) 83 km, (b) 84 km 164
A.22 Radar reflectivity versus wavenumber for DYANA: (a) 85 km, (b) 86 km 165

A.23 Radar reflectivity versus wavenumber for DYANA: (a) 87 km, (b) 88 km 166
A.24 Radar reflectivity versus wavenumber for MAC/SINE: (a) 81 km, (b) 82 km 167
A.25 Radar reflectivity versus wavenumber for MAC/SINE: (a) 83 km, (b) 84 km 168
A.26 Radar reflectivity versus wavenumber for MAC/SINE: (a) 85 km, (b) 86 km 169
A.27 Radar reflectivity versus wavenumber for MAC/SINE: (a) 87 km, (b) 88 km 170

Chapter 1

Introduction

"Vuelvo a calle Melancolía, esquina Tirso de Molina, cinco años más viejo." Javier Menéndez Flores/Sabina en Carne Viva/2006

Mesospheric radar targets have been studied for decades at sites all over the world. Radio probing applications of the mesosphere include measurements of wind velocity, which is notoriously difficult to study, and estimation of electron density [Murayama et al., 2000]. Although in operational use, the radar scattering mechanism producing mesospheric echoes is not yet fully understood. This is mainly due to the lack of in-situ instrumentation (e.g., balloons and satellites) that can be placed in those altitudes, which is very helpful for the interpretation and validation of the radar data. The situation becomes more complicated at high latitudes where the local geophysical conditions drive other types of phenomena. Polar Mesosphere Summer Echoes (PMSE) are an example of a radar phenomenon exclusive to high latitudes.

PMSE refers to a unique strong radar backscatter that occurs in the very cold summer high latitude mesosphere. Noctilucent Clouds (NLC) and Polar Mesospheric Clouds (PMC) are optical manifestations of the same phenomena. NLC are very high clouds that are visible from the ground during twilight conditions. PMC are similar clouds but observed from satellites orbiting the Earth. PMSE were first reported by Ecklund and Balsley in 1981 using a VHF radar at Poker Flat, Alaska (Figure 1.1). Notice the radar database covering two full years, 1979-1980, and extending from 50 km up to 110 km. The surprising result was that with their relatively modest sized radar they detected remarkably strong echoes

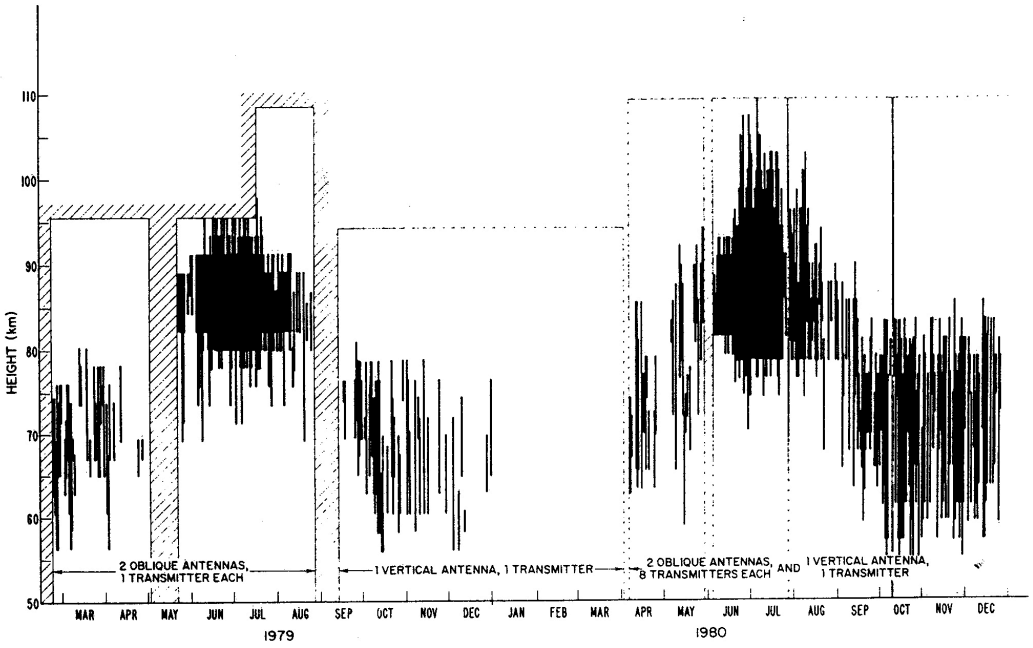

Figure 1.1: Long-term mesospheric radar observations at Poker Flat. Adapted from Ecklund and Balsley [1981].

centered near 85 km during the summer. At other times of the year sporadic and weaker mesospheric echoes were detected but only below 80 km. Since that time numerous radar studies have been conducted, mostly at frequencies at or above 50 MHz which Ecklund and Balsley used. Mesospheric echoes have been reported at 224 MHz [Röttger et al., 1988], 500 MHz [Hall and Röttger, 2001], 933 MHz [Röttger et al., 1990], and 1290 MHz [Cho et al., 1992a]. Strong radar echoes in the VHF and UHF frequency bands occur rarely since the corresponding Bragg wavelengths are deep within the viscous subrange of the neutral turbulence. This turbulence leads to variations in the index of refraction, or equivalently the electron density, which are responsible for atmospheric echoes.

PMSE are thought to be produced by the formation of charged ion clusters and ice particles near the mesopause region, at 88 km, where the minimum temperature

exists [Kelley et al., 1987]. As of today, attempts to establish a consistent theory to explain the PMSE scattering mechanism have been unsuccessful. Radar observations have indicated turbulent and non-turbulent scattering processes acting, simultaneously or separately, during PMSE events [Kelley and Ulwick, 1988]. Active experiments performed on PMSE using high power radio wave transmissions have shown evidence of both suppression and enhancement in the radar backscattered signal [Chilson et al., 2000; Havnes et al., 2003]. If pure ice particles are responsible for the radar returns, the echoes would be expected to disappear as a result of an increase in the plasma temperature of the medium. The increased number of NLC events observed over the last three decades and the direct relation of the clouds with water vapor content and low temperatures have suggested that NLC, and likewise PMSE, are possible indicators of global climate change [Thomas, 1991]. More recently, a PMC event was reported showing a strong correlation with a spacecraft launch [Stevens et al., 2003]. Space shuttles' exhaust systems introduce large amounts of water into the atmosphere, which could cause the formation of PMC, and possibly PMSE/NLC, in the very cold high latitude summer mesosphere. Undoubtedly, the physics underlying PMSE remain unclear and pose questions which are the focus of intense research work.

In order to extract more information on PMSE, and mesospheric phenomena in general, radars have been used occasionally in conjunction with sounding rockets and lidars to gain added information [Kelley and Ulwick, 1988; von Zahn and Bremer, 1999]. Traditionally, PMSE have been observed primarily with VHF radars in part due to the limited number of facilities operating at lower frequencies, i.e., the HF band, and the weak backscatter coefficient at higher frequencies, i.e., the upper VHF and UHF bands. Additionally, VHF radars are less exposed to returns

produced by other ionospheric sources. Bremer et al. [1996] and Huaman [1998] reported MF radar observations of the polar summer mesosphere but had little success clearly identifying PMSE. Karashtin et al. [1997] reported mesospheric summer echoes at HF but they gathered no data from higher frequencies to discriminate clearly the echoes as PMSE. Very few works have used multiple radars operating at different frequencies. Knowledge of the scattering properties of PMSE at various scale sizes or wavelengths could lead to highly valuable information on the many physical processes operating in the atmospheric medium.

Sounding rockets provide detailed information on the spatial structure of the scattering medium but they are constrained to a short period of time and provide only a one-dimensional view of the sampled region. Radar sensors, on other hand, surpass the temporal and coverage limitations of sounding rockets but the data they gather are constrained to a single scale size, e.g., 3-m corresponding to a 50 MHz radar frequency. An ideal scenario for PMSE investigation would be to have multiple radars operating concurrently at various frequency bands. Other types of sensors, e.g., rockets and lidars, would be a magnificent complement to any research effort since they can provide additional information on the geophysical conditions prevailing in the mesospheric medium.

In this work, we have studied mesospheric phenomena using a wider frequency range than have ever used in the past, i.e., Medium-Frequency (MF), High-Frequency (HF), and Very-High-Frequency (VHF) radar frequencies. This study places the main emphasis on PMSE phenomena. Comparisons of radar observations with rocket measurements of mesospheric dust are also reported for the first time. Dust particles at mesospheric altitudes can occur during any season and are caused primarily by the deposition of meteor ablated materials after they entry the Earth's

atmosphere. Dust particles may play an important role during the early stages of PMSE formation, providing a nucleus for ice and charge attachment [Gelinas et al, 1998; Havnes et al., 2001; Gelinas et al., 2005]. Our work was motivated by a successful detection of PMSE using one of the Alaskan HF heating/radar facilities, the High Auroral Activity Research Program (HAARP) Observatory located in Gakona, Alaska [Kelley et al., 2002]. We carried out the experiments during the First Polar Aeronomy and Radio Science Summer School, July/August of 2000, organized by the University of Alaska at Fairbanks. Further, we carried out HF observations at the second Alaskan heating/radar facility, the High Power Auroral Stimulation (HIPAS) Observatory located in Two Rivers, Alaska, during the summer of 2001, and that time the experimental sequence included concurrent lidar and MF radar measurements from the nearby Poker Flat Research Range [Collins et al., 2003; Ramos et al., 2006]. The idea was to validate the identity of the mesospheric echoes with different instrumentation and to make sure that, in fact, PMSE was the phenomenon under observation. Our group reported what are believed to be PMSE at multiple HF frequencies, identified for the first time in Alaska, and the second time ever, using the HAARP and HIPAS heating and radar facilities [Kelley et al., 2002; Collins et al., 2003]. Previously, following a suggestion by Kelley [personal communication, 1995], Karashtin et al. [1997] made the first HF observations of PMSE-like returns at the SURA facility in Russia.

Following the HF PMSE pioneer work at the Alaskan HF facilities, during 2000 and 2001, we guided our work through two paths. From one side we predicted MF/HF/VHF radar signal strengths using in-situ rocket data collected previously by scientists in Northern Europe. Prior PMSE investigations had shown the presence of two different scattering mechanisms (turbulence and steep edges of electron

density) at VHF/50 MHz, or 3-m scale sizes, by means of collocated radar and rocket observations [Kelley and Ulwick, 1988]. Prediction of VHF radar volume reflectivity using rocket measurements had been conducted previously by Røyrvik and Smith [1984], for the equatorial mesosphere, and Alcala et al. [2001b], for the polar summer mesosphere. The idea was to extend their work to lower frequencies, i.e., MF/HF bands, and see how well our radar observations agreed with predicted radar reflectivity estimates for turbulent and edge scattering components. Rocket databases collected during PMSE and non-PMSE seasons were used to perform the radar scattering predictions. The second path included expanding our PMSE observational program to multiple radar frequencies. We assumed that concurrent radar measurements at MF/HF/VHF would give us a better understanding of the different scattering mechanisms operating at scale sizes from as high as 60-m (corresponding to a frequency of 2.5 MHz) to as low as near 1-m (139 MHz). A more ambitious plan would have been to fly rockets over either HAARP or HIPAS in conjunction with making lidar and radar measurements at multiple frequencies. Funding and infrastructure limitations prevented us from carrying out the latter but radar measurements at multiple frequencies were possible.

The majority of the topics addressed in this thesis pertain to HF radar soundings of the polar summer mesosphere. For that purpose we configured two high power, high gain HF transmitters with low gain receiving antennas in Alaska's central region, at the HIPAS and HAARP HF facilities at Two Rivers and Gakona, respectively. HF observations were then conducted at HIPAS during the summer of 2002 and at HAARP during the summer of 2003. One key goal of the research work was to verify that the observed summer HF radar echoes were indeed PMSE. For that purpose, the study was complemented with observations made with perma-

nent MF/2.43 MHz and VHF/139 MHz radars located in Chatanika and Gakona, Alaska, respectively. Two portable VHF radars, operating at 28 and 50 MHz, were also used during a short period of time during the summer of 2003 at the HAARP site. Rocket data sets from Alaska and Norway were analyzed for comparison with our radar results. Quantitative predictions for radar volume reflectivity at the various frequencies were derived from the in-situ data, and turbulent and non-turbulent components. Both summer and non-summer geophysical conditions were considered. Mesospheric dust content measured by rockets and space/time collocated MF radar backscattered signals were also examined.

Below we describe the contents of this thesis. Chapter 1 introduces the concept of PMSE and the scientific problem under study. Current understanding of PMSE is summarized in Chapter 2. Chapters 3 to 5 present results of our work as well as interpretations of the collected data. Chapters 6 and 7 discuss the major findings of this thesis and recommendations for future work. The organization of the document is as follows:

Chapter 1: Introduction,

Chapter 2: Current knowledge of PMSE,

Chapter 3: MF/HF/VHF PMSE observations using Alaskan radar facilities,

Chapter 4: Scattering theory and radar reflectivity calculations using rocket data,

Chapter 5: Radar and rocket collocated observations of mesospheric dust,

Chapter 6: Discussion, and

Chapter 7: Conclusions and Future Work.

Additional plots showing complete radar and rocket data analyses, full descriptions of the radar and rocket databases, and mathematical derivations of expressions used in the main document are included in the appendices section.

Chapter 2

Polar Mesosphere Summer Echoes

A review on current knowledge of Polar Mesosphere Clouds (PMC) and/or Polar Mesosphere Summer Echoes (PMSE) is presented in this chapter. New trends in PMSE research are also discussed. The majority of the topics addressed in this chapter pertain to VHF/50 MHz radar observations, the reference sensors traditionally employed for PMSE studies. Very few observations have been reported at higher frequencies, i.e., UHF bands, due to the weak nature of the echoes. Radar studies at the MF and HF bands have been less successful in identifying PMSE returns due to the scattering from other types of phenomena (e.g., meteor trails, energetic particle precipitation, partial reflections, etc.) at similar altitudes, in addition to the limited number of facilities operating at those frequencies, particularly at HF. A major goal of this thesis, as we will see in the next chapters, is to prove that, under some circumstances, PMSE can be reliably detectable at MF and HF frequencies. The latter could provide many clues to the understanding of the well known but not fully comprehended PMSE.

2.1 Why do we study the Polar Summer Mesosphere?

The mesosphere is the atmospheric region lying on top of the stratosphere and below the thermosphere, approximately 50 km to 90 km in altitude. It is characterized by a nearly constant decrease in temperature as a function of height, $\frac{\delta T}{\delta z} < 0$, reaching temperatures as low as 100 K at its upper boundary, i.e., the mesopause [Lübken and von Zahn 1991; Schmidlin, 1992]. Our knowledge about the mesosphere is limited, compared to that of the lower and higher atmospheric

regions, due to the lack of in-situ instrumentation that can pass through it. Meteorological balloons do not get that high due to low air pressure, and satellites cannot orbit that low due to high atmospheric drag. Available techniques to probe the mesosphere include incoherent/coherent scatter radars, lidars, and rocket probes. Although radars operating in the incoherent scatter mode have been used to observe the mesosphere, that operational mode is less common due to the low ionization levels in the altitude range. In this thesis, we focus mostly on coherent scatter radar measurements but at times we refer to other types observational techniques, either remote or in-situ methods, in order to complement our findings and theories.

Interest in the polar summer mesosphere dates from the late nineteenth century when people began to observe unusual "shinning night clouds" over high northern and southern latitudes, and during the summer season. By means of optical triangulation, this intriguing phenomena, termed Noctilucent Clouds (NLC), was found to be occurring near 80 km in altitude [Jesse, 1887]. Figure 2.1 shows a picture of an NLC event over Northern Europe. Notice the wavy nature of the clouds, a typical consequence of the dynamics occurring near the mesopause region. A net increase in NLC has been observed over time after the initial sightings of the nineteenth century [Gadsden, 1990; Thomas, 1991].

It was during the International Geophysical Year (IGY) 1957-1958 when rocket measurements proved for the first time that the polar mesopause was in fact colder during the summer than in the winter [Stroud et al., 1959]. Figure 2.2 shows temperature profiles from the polar summer (left panel) and polar winter (right panel) mesosphere. Although both seasons show the same functional dependency for temperature in altitude, it is quite evident how the local minimum in temperature is dramatically smaller for the summer data sets ($T_{min} \sim 100$ K versus 200 K).

Figure 2.1: Noctilucent Clouds (NLC) © Pekka Parviainen. Adapted from: *http://lasp.colorado.edu/noctilucent_clouds*.

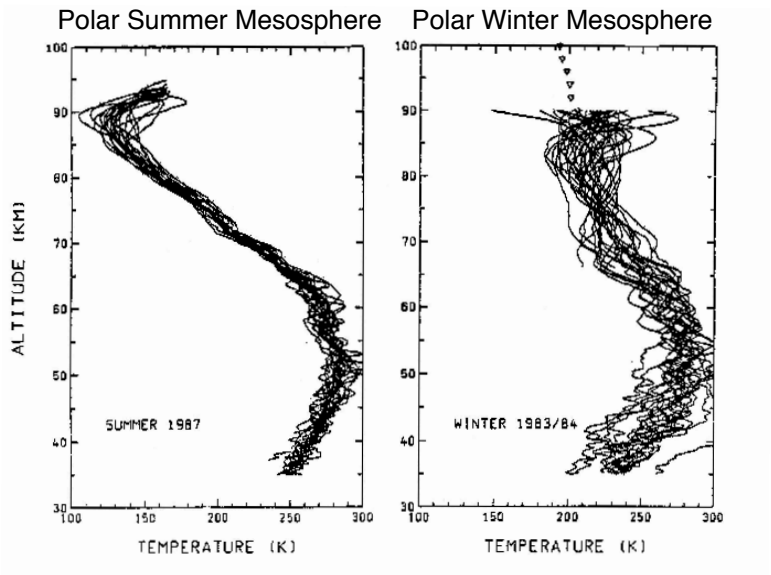

Figure 2.2: Polar Summer versus Polar Winter Mesosphere. Adapted from Lübken and von Zahn [1991].

An explanation for the summer/winter discrepancy in mesopause temperatures, using a global circulation model, is shown in Figure 2.3. Internal gravity waves (IGWs), which originate at lower altitudes, propagate vertically up to the mesopause region where they break up when the wave internal velocity or amplitude becomes larger than the wave propagation velocity, creating the so-called critical layer effect [Kelley, 2006]. Orlanski and Bryan [1969] express the breaking criterion for gravity waves as

$$\frac{\delta u}{c - \bar{u}} > 1, \tag{2.1}$$

where δu is wave perturbation or internal velocity, c is wave phase velocity, and $\bar{u}$ is the mean wind component parallel to wave propagation. In the summer hemisphere the jet stream flows westward, which makes it impossible for IGWs with a mean negative zonal wind to propagate through it. Only IGWs with a mean positive zonal wind will pass through the jet current, eventually depositing their energy at the upper part of the mesosphere where the breaking condition occurs, i.e., the wave's internal velocity exceeds its phase propagation speed, and momentum is transfered (Figure 2.3a). The wave breaking process introduces a net eastward motion into the background, which causes a superrotation and a southward flow in order to conserve angular momentum, i.e., the Coriolis effect. An upward motion at the pole is required to conserve mass, cooling adiabatically the polar summer mesosphere, in effect creating a gravity wave driven refrigerator. In the winter hemisphere, warmer air from the equator reaches the pole at mesospheric altitudes, producing downward flow/adiabatic heating, and northward motion at lower altitudes, i.e., the upper stratosphere [Holton, 1983]. This completes the global circulation cell shown in Figure 2.3b.

In 1981, Balsley and co-workers reported unique, strong radar reflectivities

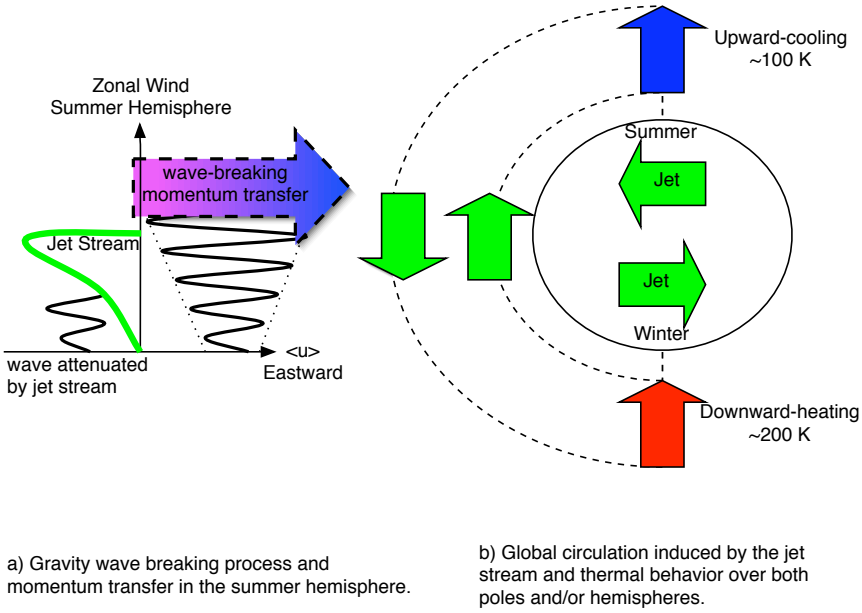

Figure 2.3: Global circulation driven by gravity waves. Adapted from Holton [1983].

from the Polar Summer Mesosphere, with signal-to-noise values of as high as 40 dB at times, using the Poker Flat 50 MHz radar in Alaska (see Figure 1.1). These radar echoes were later on termed Polar Mesosphere Summer Echoes (PMSE) by Röttger et al. [1988]. As more sources of mesospheric data began to be available during subsequent years, many more questions arose about the physics occurring in the polar summer mesosphere. The inherent capabilities of the radar technique, over optical and/or in-situ methods, made this instrument ideal to monitor the mesosphere and extract new information about the region.

NLC also occur in the polar summer mesosphere and their occurrence is linked to the low temperatures in that atmospheric region during the summer seasons of both hemispheres [Stroud et al., 1959; Lübken and von Zahn, 1991]. Thomas [1991] offers an extensive review of NLC studies during the last century. Satellite observations from space provided a more systematic way to observe NLC,

which were termed Polar Mesospheric Clouds (PMC). Prior to the rocket flights launched during the International Geophysical Years (IGY) of 1957-1958 [Stroud et al., 1959], the NLC connection with low temperatures was unknown. The extremely low temperatures in the polar summer mesosphere favor the formation of ice particles from water vapor reaching those altitudes. When these particles are big enough they can scatter sunlight and become visible from the ground as NLC. Extremely low temperatures are a necessary condition for the formation of NLC and/or ice due to the dry conditions of the mesosphere. Their first appearance back in 1885 is attributed to the explosion produced by the Krakatoa volcano in Indonesia [Backhouse, 1885]. Krakatoa injected water into the stratosphere that eventually became NLC when it reached to the higher altitudes of the mesosphere. Thomas et al. [1989] proposed that the anthropogenic increase in methane gas beginning in the industrial era was responsible for the steady increase in NLC occurrence over the years. Methane gases are produced from the combustion of fossil materials. At mesospheric heights methane reacts with natural oxygen producing water as a second order product. An increase in water in the polar summer mesosphere could cause an increase in ice formation or NLC. If NLC and/or PMC were truly indicators of global change, their relation to PMSE would make radar the ideal technique to monitor long-term trends of this phenomena. Still, many questions remain about the nature of PMSE and the interpretation of the radar derived information. Before discussing our results in subsequent chapters, we provide a historical review of PMSE studies and summarize current observations and theories in the next and concluding sections of this chapter.

2.2 Historical Review of PMSE

Up to the discovery of PMSE in the 1980s, only very large VHF atmospheric radars were thought to be suitable for clear air turbulence detection in the mesosphere since the radar Bragg scale ($l_{Bragg} = \lambda_{radar}/2$) occurs within the viscosity range where turbulent energy gets dissipated (see Figure 2.4). This is due to the increase of kinematic viscosity at the scale sizes relevant to VHF frequencies. All these ideas began to be questioned with the discovery of remarkably strong VHF radar echoes from the polar summer mesosphere between 1979 and 1985 over Poker Flat, Alaska [Ecklund and Balsley, 1981; Balsley et al., 1983]. These PMSE echoes were easily distinguishable from non-summer and non-polar data collected using the same 50 MHz radar system and/or similar radar systems at lower latitudes. The first explanations involved very strong turbulence, and/or gravity wave breaking, producing electron density inhomogeneities. But at PMSE altitudes, specifically between 80 and 95 km, the viscous cutoff scale (l_o)for neutral turbulence is much larger than the VHF radar Bragg scale. Note that the radar mechanism could be different at lower (MF or HF bands) frequencies since half the radar wavelength is in or near the inertial subrange. A major breakthrough came through the work of Ulwick et al. [1988]. Those authors compared polar and non-polar rocket spectra (Figure 2.5) and found an extended inertial subrange of turbulence in the polar data, which was non existent in polar winter and equatorial rocket data. More radar observations were conducted during subsequent years in an effort to understand the rocket measurements and explain the "intriguing" PMSE echoes. In the next section we summarize characteristics of PMSE radar observations conducted prior to the summer of 2002, when the author began to study this phenomena.

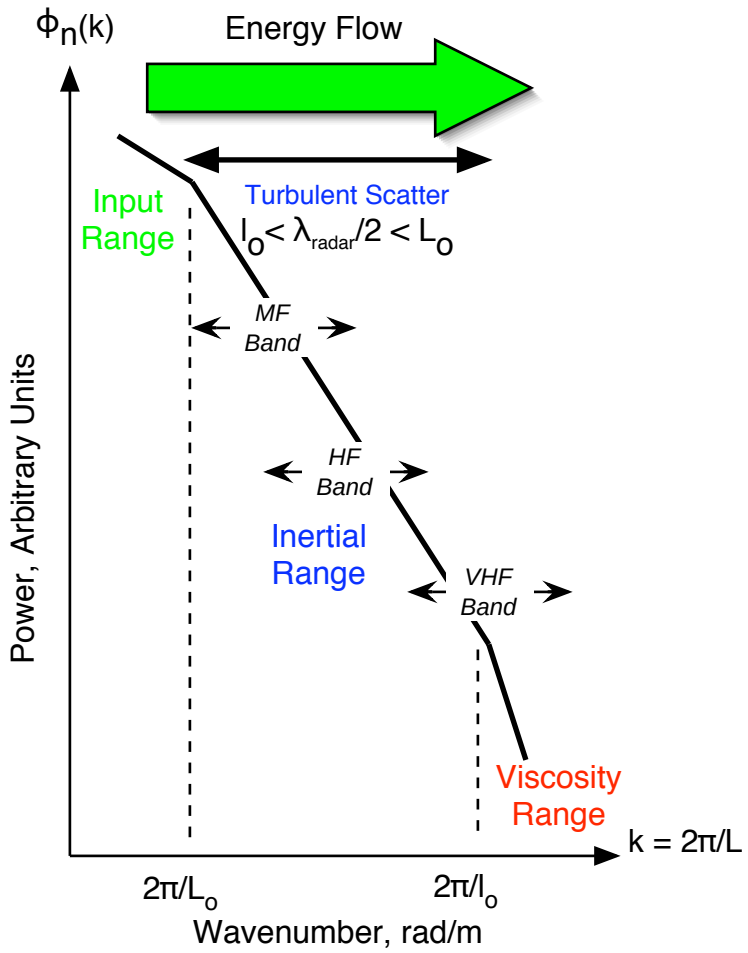

Figure 2.4: Power spectrum of refractive index fluctuations in a turbulent atmosphere. Approximate locations (in k-space) for Medium-Frequency (MF), High-Frequency (HF), and Very-High-Frequency (VHF) radar frequencies are superimposed. Adapted from Craig [2002].

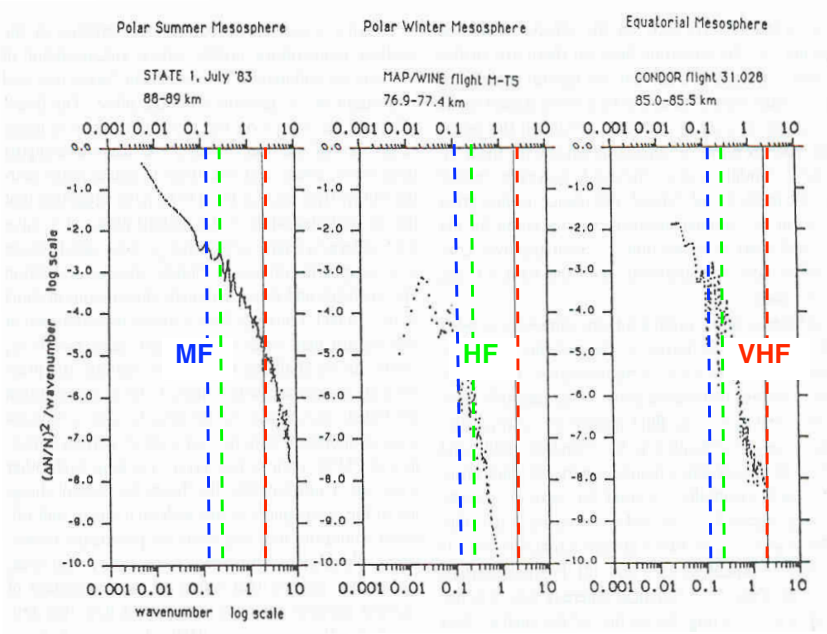

Figure 2.5: Polar and non-polar rocket spectra. The vertical dashed lines indicate Bragg scales for 2.5 MHz (MF), 5 MHz (HF), and 50 MHz (VHF) radar frequencies. Adapted from [Ulwick et al., 1988] (left), [Blix, 1988] (middle), and [Røyrvik and Smith, 1984] (right).

2.3 Summary of Radar Observations

Knowledge about PMSE has been extracted primarily from VHF radar observations, in part, as a result of the discovery of the radar echoes using a VHF/50 MHz radar system [Ecklund and Balsley, 1981], the availability of that type of radar, and their well known advantages (e.g., system portability, low cost/power consumption, moderate sky noise, etc.). The radar observations have been complemented with occasional rocket soundings to complement and validate the remotely sensed data.

2.3.1 General Features

PMSE, as the name suggests, refer to polar/summer phenomena because of the geographical location (above 50 degrees in latitude to our knowledge) and temporal occurrence (between end-of-May and mid-August) of the mesospheric radar echoes [Ecklund and Balsley, 1981; Balsley et al., 1983; Röttger et al., 1988]. They have been observed from altitudes as low as 75 km up to about 100 km, with maximum incidence at 86 km [Ecklund and Balsley, 1981]. Peak detections are reached between the months of June and July with diurnal maxima and minima at around 12 and 20 LT, respectively [Balsley et al., 1983; Czechowsky et al., 1989].

Patchiness in PMSE is manifested by the intermittence of the radar echoes with intensities varying by factors of as large as 20 dB over time scales of a few minutes [Collis et al., 1994; Bremer et al., 1996]. Doppler velocities show wavy motions with maximum vertical velocities of up to ± 10 m/s [Röttger and La Hoz, 1990]. The echoes are highly aspect-sensitive at 53.5 MHz [Czechowsky et al., 1988; Reid et al., 1988], an indication of non-turbulent mechanisms operating in the medium.

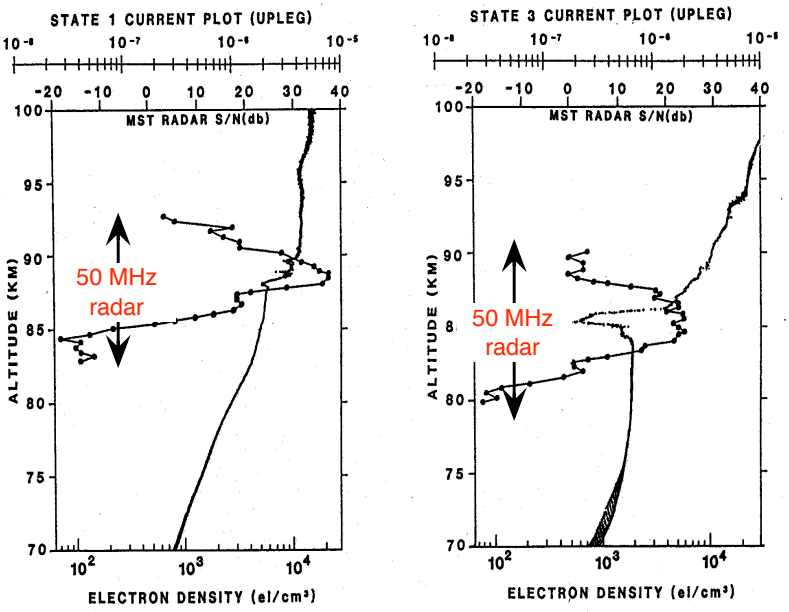

Figure 2.6: Radar and rocket concurrent observations during PMSE. Adapted from Kelley and Ulwick [1988].

Weaker PMSE have been reported at the South Pole [Balsley et al., 1993; Balsley et al., 1995]. One explanation, for this lack of PMSE, is the higher temperatures in the South Pole, as reported by satellites, or less water vapor concentration, which is an ingredient necessary for ice or aerosol formation. Similarly, PMC/NLC sightings have been fewer in the Antarctic pole, in agreement with the PMSE results [Olivero and Thomas, 1986].

A good correlation has been found between PMSE echo power and D-region electron density [Czechowsky et al., 1989; Kelley et al., 1990]. Echoes do not occur without some minimum level of electron density. No clear correlation between PMSE and auroral particle precipitation has been found [Luhmann et al., 1983; Kirkwood et al., 1995]. Variations in geomagnetic activity have shown little correlation with PMSE occurrence [Röttger et al., 1990; Kirkwood et al., 1995].

2.3.2 Other Frequency and Multi-instrument Observations

Since the pioneering PMSE work at Poker Flat [Ecklund and Balsley, 1981], observations at frequencies greater than 50 MHz have been carried out mainly at European radar facilities. Among these are the observations by Hoppe et al. [1988] at 224 MHz, Röttger et al. [1990] at 933 MHz (EISCAT UHF radar), and Cho et al. [1992b] at 1290 MHz (Sondrestrom radar). More recently, PMSE observations have been reported at MF (2.43 MHz) and HF (8-9 MHz) frequencies by Bremer et al. [1996] and Karashtin et al. [1997], respectively. Very few observations have been conducted with radars operating simultaneously at multiple frequencies, which makes it difficult to draw firm conclusions on the nature of the radar mechanism at multiple scale sizes. Kelley and Ulwick [1988] reported simultaneous rocket and 50 MHz radar measurements during a PMSE event (Figure 2.6). von Zahn and Bremer [1999] carried out concurrent lidar and radar observations of NLC/PMSE for the first time (Figure 2.7). Additional work includes the RF heating modulation of PMSE at the EISCAT facility [Chilson et al., 2000], newer HF observations at the HAARP facility in Alaska [Kelley et al., 2002], collocated lidar/HF radar observations [Collins et al., 2003], PMSE detection using SuperDARN radars [Ogawa et al., 2002], and MF/HF/VHF concurrent measurements of PMSE at the HIPAS, HAARP, and Poker Flat Alaskan facilities [Ramos et al., 2006].

The radar signature at 224 MHz shows similar features of PMSE at 50 MHz [Hoppe et al., 1988]. Röttger et al. [1988] reported examples of Doppler spectra too narrow for turbulent scatter, but quite broad spectra were also observed at other times during PMSE events. These observations are in agreement with the radar and rocket observations by Kelley and Ulwick [1988], where turbulent

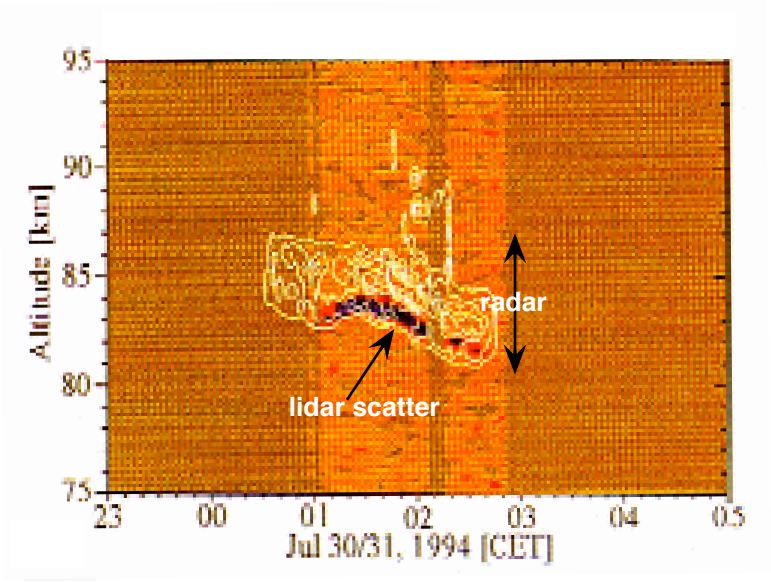

Figure 2.7: Concurrent lidar and radar observation. The lower dark patch, at around 83 km, shows the NLC/lidar scattering region that is coincident with the bottom part of the PMSE/radar echoes. Adapted from von Zahn and Bremer [1999].

and non-turbulent mechanisms were found within the range of maximum radar signal, 80-90 km (Figure 2.6). At higher frequencies, i.e., 933 and 1290 MHz, coherent radar echoes are discriminated from incoherent scatter by the high power and narrow width of the doppler spectra. Concurrent observations at 50 and 933 MHz, using the Cornell VHF and EISCAT UHF radars, respectively, showed a bite-out in electron density occurring at the same altitude of the VHF PMSE echo [Röttger et al., 1990]. Slowly descending PMSE layers, with Doppler velocities of $\sim$1 m/s, have shown up similarly at HF frequencies [Kelley et al., 2002]. Simultaneous MF (2.43 MHz) and VHF (224 MHz) observations by Bremer et al. [1996] seemed to be related but the echo structures were more difficult to distinguish at the lower frequency. All these assorted observations have contributed pieces to the understanding of PMSE although no one has studied PMSE systematically at MF/HF/VHF frequencies. The latter could add new information about this phenomena and possibly explain the quite often contradictory results.

2.4 Theories for PMSE

Radar scattering from the mesosphere is produced by irregularities in the radio refractive index of half the radar wavelength which results from variations in electron density. The major causes of electron density variations are: (1) random thermal motions, and (2) any structuring created by mechanical, electro-dynamical, and/or chemical effects. Mechanism 1 produces what is known as Incoherent Scatter. Mechanism 2 is associated with Coherent Scatter. Due to the high strength of the echoes and the narrow width of the Doppler spectra (i.e., few m/s) VHF PMSE is generally classified as coherent scatter but the situation can be somehow different at higher frequencies (i.e., the UHF band) as we describe below. To our

knowledge, few data sets are available and no theories explain what drives the MF or HF PMSE. We work along those lines in this thesis.

2.4.1 VHF

Early explanations suggested that VHF PMSE was the result of turbulence produced by shear instabilities and tidal modes [Balsley et al., 1983]. Turbulent activity produced by neutral gas motions would act as the generation mechanism to sustain electron density fluctuations at small scale sizes, e.g., 3-m or 50 MHz. Later, it was realized that turbulence alone would not be enough to account for the high strength of the echoes [Hoppe et al., 1988; Röttger et al., 1988; Röttger et al., 1990]. In other words, the amount of energy dissipation required to explain the radar signal strengths was unrealistic for the mesosphere.

Later on, a combination of turbulence and stratification, acting together or individually, were suggested as responsible for the radar scattering [Kelley and Ulwick, 1988; Cho and Kelley, 1993, and references therein]. The two extreme cases for this model are isotropic turbulent scatter, and Fresnel reflection. (Please refer to Chapter 4 for a detailed description of the different radar scattering mechanisms.) Intermediate levels would be anisotropic turbulence and Fresnel or edge scatter. Up to the moment, VHF PMSE observations are best explained as a combination of the last two, weak turbulent anisotropic scatter and Fresnel scatter, acting separately on different occasions [Thomas et al., 1992] and/or simultaneously in different layers [Lübken et al., 1993; Cho et al., 1993; Ulwick et al., 1993]. The occurrence of turbulence is supported by NLC observations, where the presence of saturated gravity waves is clearly distinguished in the clouds [Witt, 1962; Fritts et al., 1988]. Narrow spectral widths, derived from 224 MHz radar observations,

indicate the presence of weak turbulence during PMSE [Röttger and La Hoz, 1990]. Aspect sensitivity measurements show high degrees of anisotropy for small angles but a more smooth power fall-off for bigger angles [Czechowsky et al., 1988]. Rocket flights during PMSE events have reported sudden transitions in electron density accompanied by nearly homogeneous fluctuations in electron density with structure at scale sizes comparable to the Bragg length for a 50 MHz radar [Kelley and Ulwick, 1988; Lübken et al., 1993; Cho et al., 1993; Ulwick et al., 1993].

Diffusion mechanisms are frequently cited to explain the origin of PMSE echoes. Assuming that the generation of electron density variations is not constant, a reduction in diffusion would make it possible to sustain the fluctuations at smaller scales. For VHF PMSE, the radar Bragg lengths are smaller than the predicted microscale of turbulence; beyond it, molecular viscosity destroys the turbulent eddies. It is possible to extend the viscous cutoff of turbulence by increasing the so-called Schmidt number,

$$S_c = \nu / D \tag{2.2}$$

which is defined as the ratio of kinematic viscosity to the diffusion coefficient [Batchelor, 1959]. For a neutral atmosphere and plasma with low mass positive particles, S_c is 1. The viscous convective subrange, which occurs for $S_c > 1$, is an extension of the viscous range of turbulence (Figure 2.4) and would allow electron density structures to be maintained at VHF and possibly UHF wavelengths [Cho and Kelley, 1993]. Kelley and Ulwick [1988] analyzed rocket data during PMSE conditions and found electron density structures at scales smaller than the viscosity cutoff for neutral turbulence (Figure 2.5). Their results validate the above ideas of an extended viscous range produced by a reduction in diffusion and corresponding increase in S_c. Hall [1991] estimated S_c between 100 and 900 using rocket data

from the MAC/SINE campaign.

Similarly, a decrease in electron diffusivity would increase the probability for sharp edges to be maintained. Kelley et al. [1987] suggested that the presence of heavy hydrated ions, e.g., $H^+(H_2O)_n$, could slow down electrons via ambipolar electric fields. Cho et al. [1992b] deduced that if half the charge was tied to macro-particles, e.g., ice particles, then high Schmidt numbers would result. They calculated that a charge number, n, of at least 20 would be necessary in order to sufficiently reduce electron diffusion and raise S_c to the order of 100. This large charge value is very unlikely due to the high work function of ice particles. Havnes et al. [1990] suggested that ice impurities could decrease the work function of mesospheric particles and increase the chances of highly positive particles. More in-situ measurements are needed to determine what type of particles, either liquid or solid, are present in the upper mesosphere and the predominant charges of the ion-particle clusters.

2.4.2 UHF

At UHF frequencies, the Bragg scale is very small and the coherent scatter associated with a high Schmidt number is weak. But charged aerosols can also enhance incoherent scatter. This is known as "dressed aerosol scatter" [Cho and Kelley, 1993]. The Debye length, λ_D, a measure of the distance up to which the plasma shields out the electric potential of the charged aerosol, determines the amount of incoherent scatter. If $\lambda_D << \lambda_{radar}$, the electrons within the Debye shielding region will respond in phase and a net increase proportional to $|Z|$, where Z is the aerosol charge, occurs over normal incoherent scatter. Another way to determine contributions to radar scatter is by considering the ratio of the average

distance between aerosols to the Debye length. If this ratio is large compared to 1, the aerosols can be considered independent, and coherent backscatter will be considerably enhanced. The optimal mechanism in favor of these conditions would be a small number of highly charged aerosols, in opposition to a large number of particles with a low charge. The former is limited by the high work function of ice particles, which could explain the lack of UHF PMSE events.

2.4.3 Latest Developments in PMSE Research

Attempts have been made to produce a unified PMSE theory consistent with the range of experimental databases (in-situ, ground and space based techniques), mesospheric models, and knowledge about the physics of dusty plasmas and electron diffusivity in their surroundings. Rapp and Lübken [2004] suggest a model for PMSE occurrence rates (POR) based on turbulence occurrence rates (TOR) versus altitude, obtained from rocket soundings, and diffusion times for radar signals due to mesospheric particles of different sizes. Their predicted PMSE profiles show a good agreement with observational data sets and explain the lack of turbulence at the lower layers, e.g., below 85 km. Active and/or fossil neutral turbulence can both be used to explain a majority of the observed PMSE events according to those researchers.

Similarly, Rapp and Lübken [2004] have found good agreement between model calculations for volume reflectivity, $\eta(k)$, and VHF radar measurements under the assumption of (1) neutral turbulence combined with a large Schmidt number for electrons, (2) charged ice particles of radii larger than 10 nm, and (3) diffusion times of the order of minutes. Higher turbulence occurrence rates at the upper parts of PMSE, e.g., above 85 km, are confirmed by low aspect sensitivities re-

ported from those altitudes. Larger aspect sensitivities, and quite often, extremely narrow spectral widths reported from lower altitudes, are not yet completely understood [Cho and Kelley, 1993; Rapp and Lübken, 2004]. Two frequently mentioned candidates to explain PMSE at altitudes below 85 km are (1) anisotropic turbulence and (2) horizontal layering mechanisms, which are known to be responsible for specular reflections at HF [Thrane et al., 1981].

Careful temporal and spectral analysis of the radar signal allows one to discriminate turbulent from non-turbulent or previously turbulent PMSE events. The latter is known as fossil turbulence. PMSE is thought to be produced by a combination of all these mechanisms, where the electron variations detected by radars are triggered by a nearly constant generation of turbulent plasma structures or by previously created structures that remain present due to their long lifetimes.

In summary, and following the review work by Rapp and Lübken [2004], the most likely scenario to describe VHF PMSE, as of today, is a medium consisting of neutral air turbulence combined with a low electron diffusivity due to heavily charged ice particles. An extended inner scale for turbulent fluctuations, as a result of a high Schmidt number, would support the occurrence of radar echoes at VHF frequencies. This is not a necessary condition for radio observations at lower frequencies or bigger scale sizes. The long lifetime for plasma structures in the presence of large, charged ice particles is thought to be the cause of frequent temporal decoupling between PMSE and active turbulence [Rapp et al., 2003]. In other words, non-turbulent PMSE echoes could result from previously turbulent events where the irregularities in electron density are sustained by the high polar forces between the background plasma and the charged particles. The limited number of UHF data sets explain the lack of theories for PMSE at higher frequencies.

Chapter 3

Radar Facilities and Observations of PMSE

In this chapter we describe the radar data sets analyzed in this thesis. First we describe the radar facilities used for PMSE observations. Then, we show data collected at the different radar sites. Particular emphasis is given to the echo properties at the lower frequency bands where we show that PMSE is detectable, i.e., MF and HF, and where less work has been published. Proof-of-concept experiments were conducted in 2000 and 2001, while the majority of the observations were carried out during the summers of 2002 and 2003. The number of experiments were limited due to on-going construction at the HF facilities. For a detailed description of the radar databases (e.g., radar parameters, geographical locations, campaign dates, data format, etc.) please refer to Appendices A.1 and A.2.

3.1 Alaskan Radar Facilities for PMSE Studies

Early PMSE work concentrated on understanding the echo characteristics at VHF frequencies (i.e., 50 MHz with 3-m Bragg length) due to the limited number of observations at other frequencies. Radar observations at lower or higher frequencies are rare due to the small number of facilities operating at HF, the difficulty in identifying MF PMSE signatures, and the scarcity of echoes at the upper bands (upper-VHF and UHF). HF mesospheric summer echoes were first observed by Karashtin et al. [1997] at the SURA facility near Vasilsursk, Russia, although no supportive information was available to validate them firmly as PMSE. Our

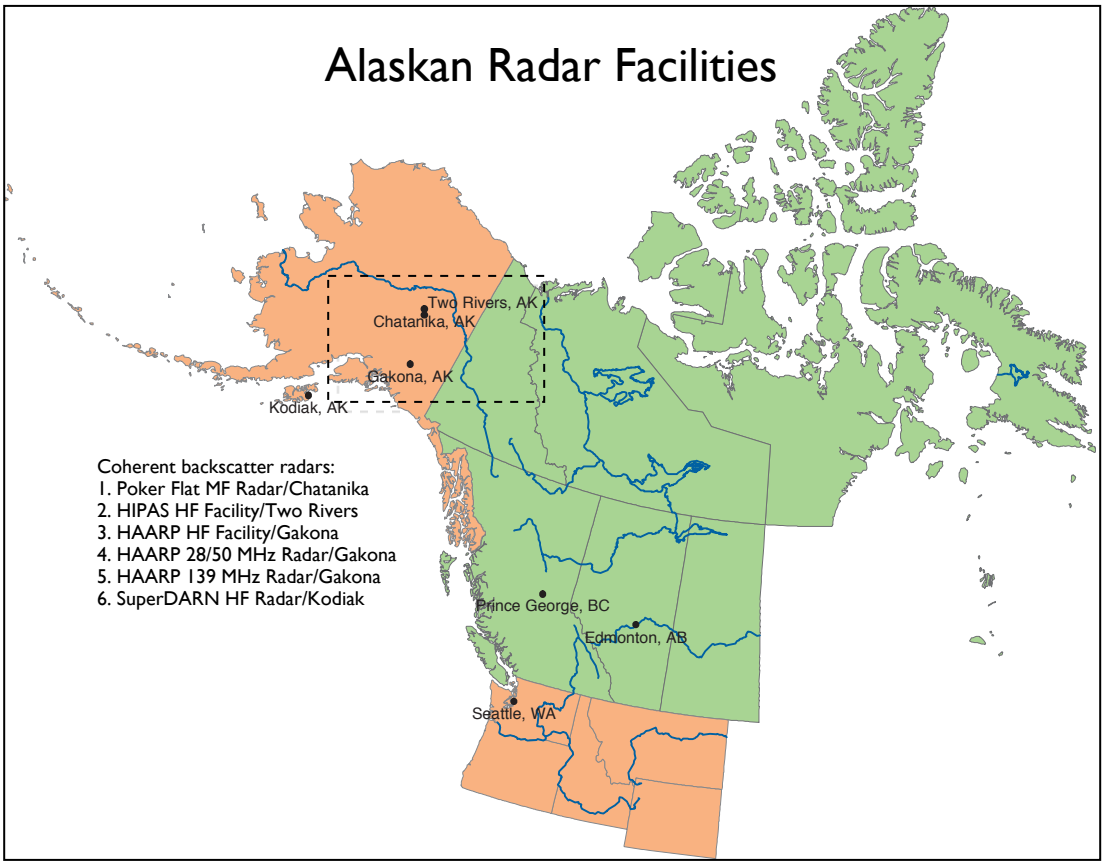

Figure 3.1: The Alaskan Radar Facilities.

Table 3.1: System Parameters for the Alaskan HF Facilities.

Radar Facility	Frequency (MHz)	Antenna Gain (dB)	Power (kW)	ERP[1] (MW)
HAARP	4.9	18.4	960	66.4
HIPAS	4.53	17.5	800	45.0

[1]Effective Radiated Power for chosen frequency without losses.

group has successfully observed PMSE at HF, for the first time in Alaska, and the second time ever, using the HAARP (High Auroral Activity Research Program) and HIPAS (High Power Auroral Stimulation) heating and radar facilities [Kelley et al., 2002 and Collins et al., 2003]. For an updated description of both ionospheric observatories please refer to the following websites: *www.haarp.alaska.edu* and *www.hipas.alaska.edu*. System parameters for HAARP and HIPAS are summarized in Table 3.1.

More recently we have had access to data from the Poker Flat Medium Frequency (PFMF) radar, located near Fairbanks, Alaska, which operates at a frequency of 2.43 MHz [Murayama et al., 2000], as well as the nearby HIPAS system. New developments at HAARP have also enabled us to extend observations to higher frequencies using portable 28 and 50 MHz radars. In addition, a new coherent backscatter radar, operating at 139 MHz, has been deployed permanently at HAARP, which we operated for several weeks during the summers of 2002 and 2003.

Figure 3.1 shows a map containing the locations of the Alaskan radar facilities referred to. Two main geographical areas along the Alaskan central region can be identified: the Chatanika or Fairbanks area: 65° N, where HIPAS and Poker Flat

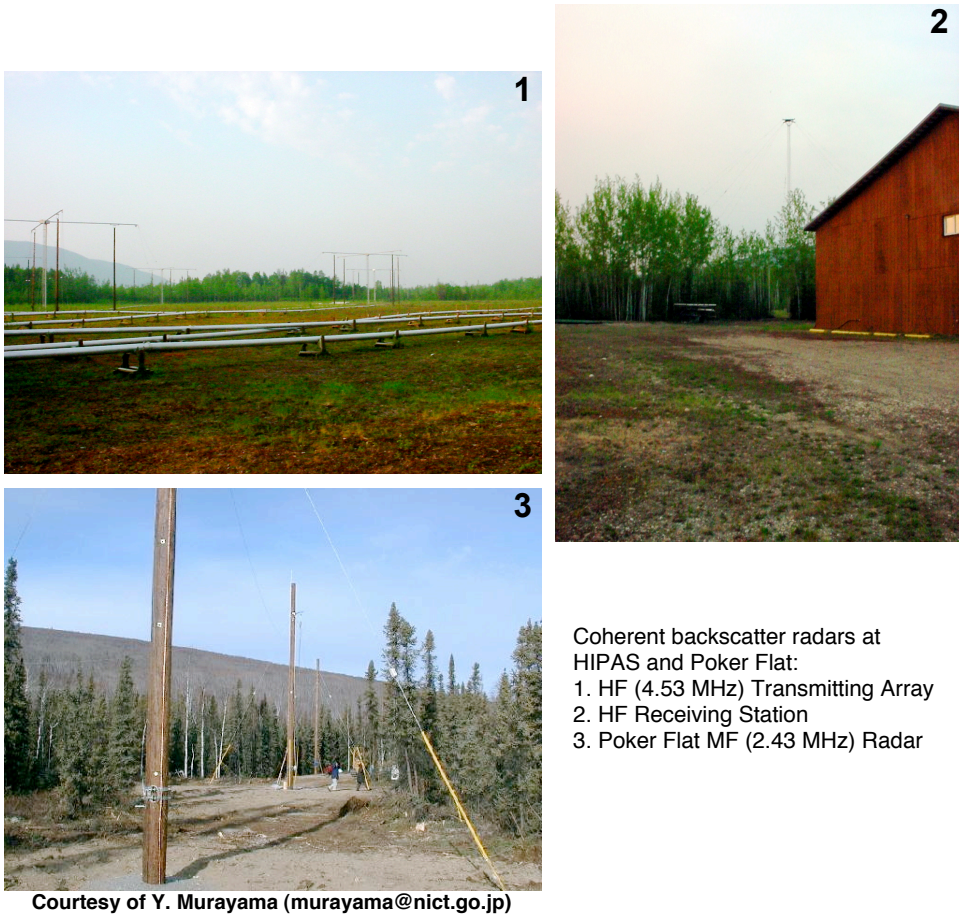

Figure 3.2: Coherent Backscatter Radars at HIPAS and Poker Flat, Alaska.

are located, and the Gakona area: 62° N, where the rest of the radar systems are located. Figures 3.2 and 3.3 show all the radar sites where the author conducted measurements. Data from all these radar systems is shown in section 3.3.

3.2 Radar Configurations and Data Sets

3.2.1 Poker Flat Medium Frequency Radar

The Poker Flat MF radar data were obtained through a collaboration between Cornell University, the University of Alaska at Fairbanks (UAF), and the National

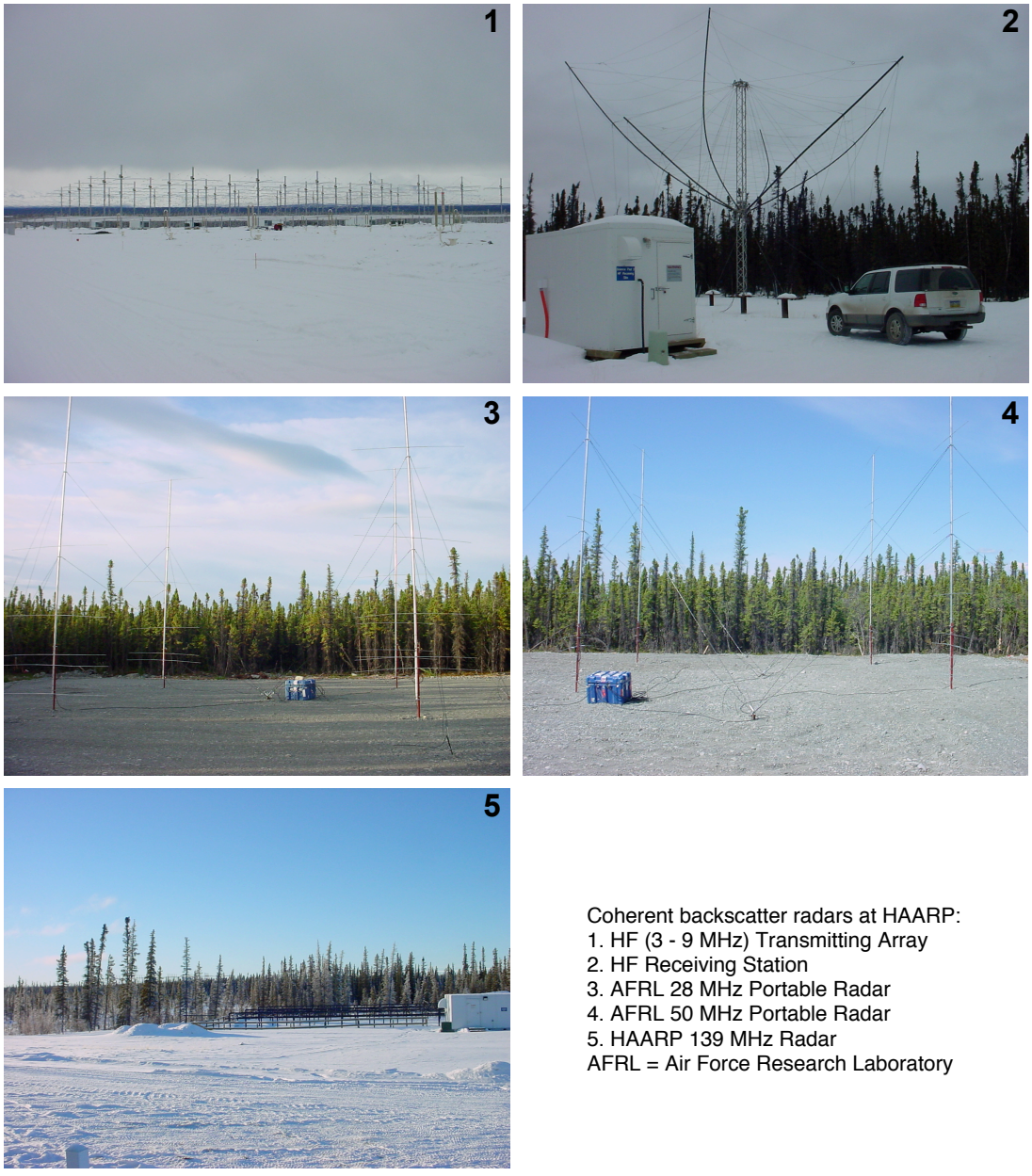

Figure 3.3: Coherent Backscatter Radars at HAARP.

Institute of Information and Communications Technology (NICT) in Japan. The MF system operates continuously at the Poker Flat Rocket Range (PFRR) near Chatanika, Alaska. The radar setup consists of five antennas, one used for transmission and four for reception. The radar transmitted power and frequency are 50 kW and 2.43 MHz, respectively, and the data are sampled between 60 and 100 km altitude, with a range resolution of 2 km. The backscattered signals, collected simultaneously with the four receivers, are analyzed to deduce horizontal winds, using the Full Correlation Analysis (FCA) technique, and electron density measurements, using the Differential Absorption Experiment (DAE) method [Murayama et al., 2000]. The post-processed data contain backscattered power as a function of altitude for the four different receiving stations. For our purposes, we chose to analyze data only from station number one due to the similarity of the results between the four receivers.

3.2.2 HIPAS

The HF PMSE data sets from the HIPAS Observatory were obtained during a seasonal radar campaign. Our first experiments at HIPAS, a proof of concept campaign, were carried out during the Summer of 2001. After a successful detection of PMSE during those few weeks we planned for a full season campaign in the summer of 2002. The goal was to study the climatology of PMSE as done by Balsley and co-workers in the early 1980s [Balsley et al., 1983] but at a lower frequency in the HF band. For a total of 20 days, at 2 hours per day, HIPAS was operated as an HF radar, transmitting at 4.53 MHz with a 10 us pulse and an Inter-Pulse-Period (IPP) of 15 ms. We show this seasonal data, spread out over the months of June to September of 2002, in section 3.3.3.

The data processing scheme at HIPAS begins with the sampling of the In-Phase and Quadrature received signals for a each individual transmitted pulse. The atmosphere is probed for a total of 3 ms, or 450 km, and beginning at 50 km. We are only interested in data from mesospheric altitudes (i.e., 50-100 km) but keep information from upper regions for other studies or future work. The raw data files consist of In-Phase and Quadrature values as a function of altitude and time or transmitted pulse. Coherent and/or in-coherent averaging are performed during off-line processing. Refer to Appendix A.1 for additional details about the HIPAS HF radar setup.

3.2.3 HAARP

At HAARP, we conducted shorter radar campaigns than at HIPAS (several weeks as opposed to the full season), which included two summer periods (June 2002 and July 2003) and one winter (March 2004). Limitations for observational time were mainly due to construction schedules since the facility is still in the developmental stage. HAARP gives a wide range of capabilities for experiments (e.g., computer pre-programmed transmission schedules, different modulation schemes, power stepping, beam angle, frequency selection, heating/pulsing modes, etc.), in addition to state of the art on-site instrumentation for ionospheric diagnostics (e.g., an ionosonde, riometer, magnetometer, other radars, etc.).

The current HF radar system at HAARP uses 48 crossed-dipole antennas for transmission, if transmitting at full power, and an off-site spira-cone antenna for reception (located about 1.5 km from the transmitter array). The spira-cone antenna is of the log-periodic type (right hand circular polarization) and is constructed as four interleaved spirals in a conical shape with the apex of the cone pointing

downward. This configuration provides a very broad range of HF frequencies for reception (2-30 MHz) where performance in both pattern and antenna impedance remain relatively constant. Detailed specifications of the antenna model can be found at the HAARP website. Reference and timing signals for Doppler measurements and data acquisition control are provided to the receiving station via a fiber optic line. Although multiple frequencies are available for transmission, we have done our observations mainly at 4.9 MHz due to the good compromise between atmospheric absorption and noise mitigation. Other parameters like pulse-width and inter-pulse-period have been kept similar to HIPAS for consistency purposes. The software and hardware for data acquisition/processing are based on the system previously developed for HIPAS (see Appendix A.1).

The AFRL (Air Force Research Laboratory) 28 and 50 MHz radars are portable systems and were deployed at HAARP during the Summer of 2003 for a short-term research campaign. Most of the PMSE data were collected using the 50 MHz system due to technical difficulties with the 28 MHz system. Both radars use arrays of 4 Yagi antennas for transmission and reception, pointed vertically. The 50 MHz transmitted pulse was Barker coded to improve the range resolution. In addition, a smaller IPP (compared to the HF system) was chosen to improve signal detection in both radars and the data were sampled up to about 120 km only. The transmitters, receivers, and the data acquisition system were provided by scientific staff from the Air Force Research Laboratory in Hanscom AFB, Massachusetts.

The 139 MHz radar was built by Geospace Research, Inc. and initially deployed at HAARP for testing purposes in May 2001. The antenna system used for transmission/reception consists of a Co-Co array with beam steering capability. A variety of geophysical phenomena have been studied since then, including

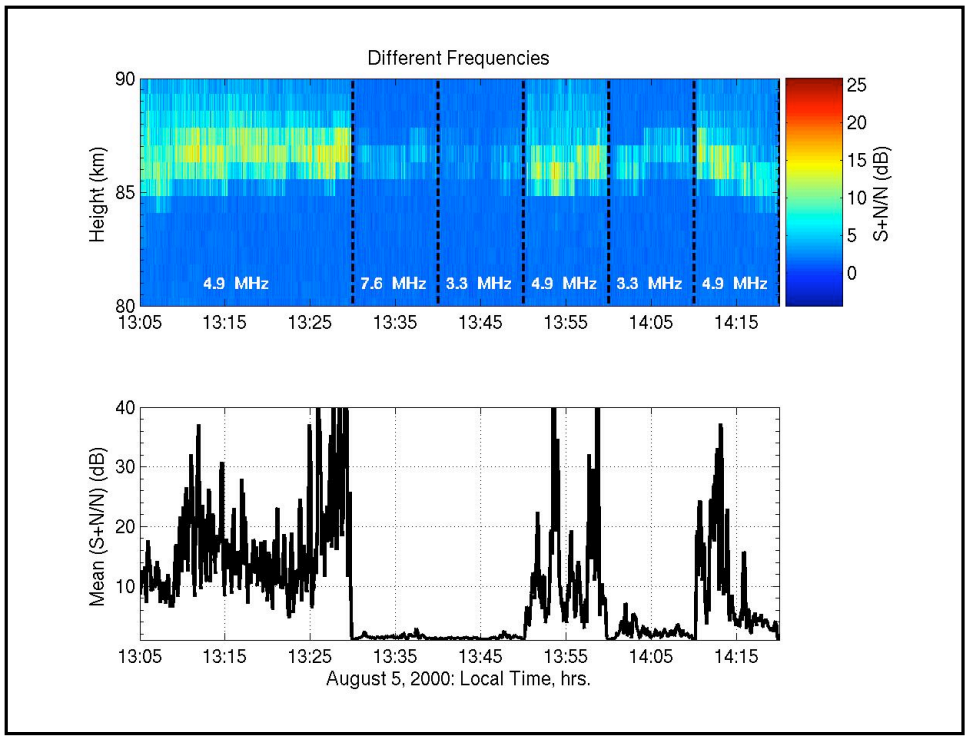

Figure 3.4: PMSE observations at multiple frequencies using the HAARP HF Facility [August 5, 2000].

meteors and PMSE [F. Djuth, personal communication, 2002]. Communications interference has been a main issue but an automated frequency retuning procedure has provided significant improvements for signal detection. Phase coding of the transmitted pulse, using Barker codes, aids greatly in signal detection as we will show in the data section.

The 139 MHz system was in operation continuously for about 20 days in July 2003. Power black-outs limited data collection for a longer period. We present data from selected days, in addition to concurrent data from the nearby HAARP HF/VHF systems, in section 3.3.

3.3 PMSE at MF/HF/VHF

3.3.1 Preliminary MF and HF Work

In the first exploratory experiments made by our group at the HAARP HF facility near Gakona, Alaska, a variety of frequencies were used as shown in Figure 3.4 (August 5, 2000; 13:05-14:15 LT). Layered echoes were detected at 3.3, 4.9, and 7.6 MHz with the optimum detections between 4 and 5 MHz [Kelley et al., 2002]. The first set of multi-band (MF/HF) radar observations of PMSE were conducted during the summer of 2001 near Fairbanks, Alaska. Figure 3.5 presents an example of a PMSE event observed concurrently at (a) Poker Flat (2.43 MHz) and (b) HIPAS (4.53 MHz) on July 6, 2001; 18:30-20:30 UT. The two systems are located about 20 km apart with beams that overlap the HIPAS facility. The latter antenna has a half power beamwidth of 22 degrees at 4.53 MHz while the MF antenna has a beamwidth of about 40 degrees. The color scale shows a well defined layer centered near 87 km at HF while the MF data show echoes coming from a wide range of altitudes. Next to the color scales we have plotted three power profiles at three different times for each radar. The layered nature of the HF data is clear in each case while the MF profiles show just a relative maximum near the 85-88 km height range. In fact, it is well known that the MF echo strength is almost a monotonic function of altitude worldwide [Murayama et al., 2000]. As an example of this feature we show simultaneous MF data from the Poker Flat radar and a very similar system at Platteville, Colorado in Figure 3.6 (July 14, 2002; 16:00-24:00 UT). The two power profiles were obtained at 18:30 UT. The echo strength for the Colorado system (bottom panels) increased monotonically with altitude while the high altitude signal had a distinct layer (top panels). The outstanding MF/HF

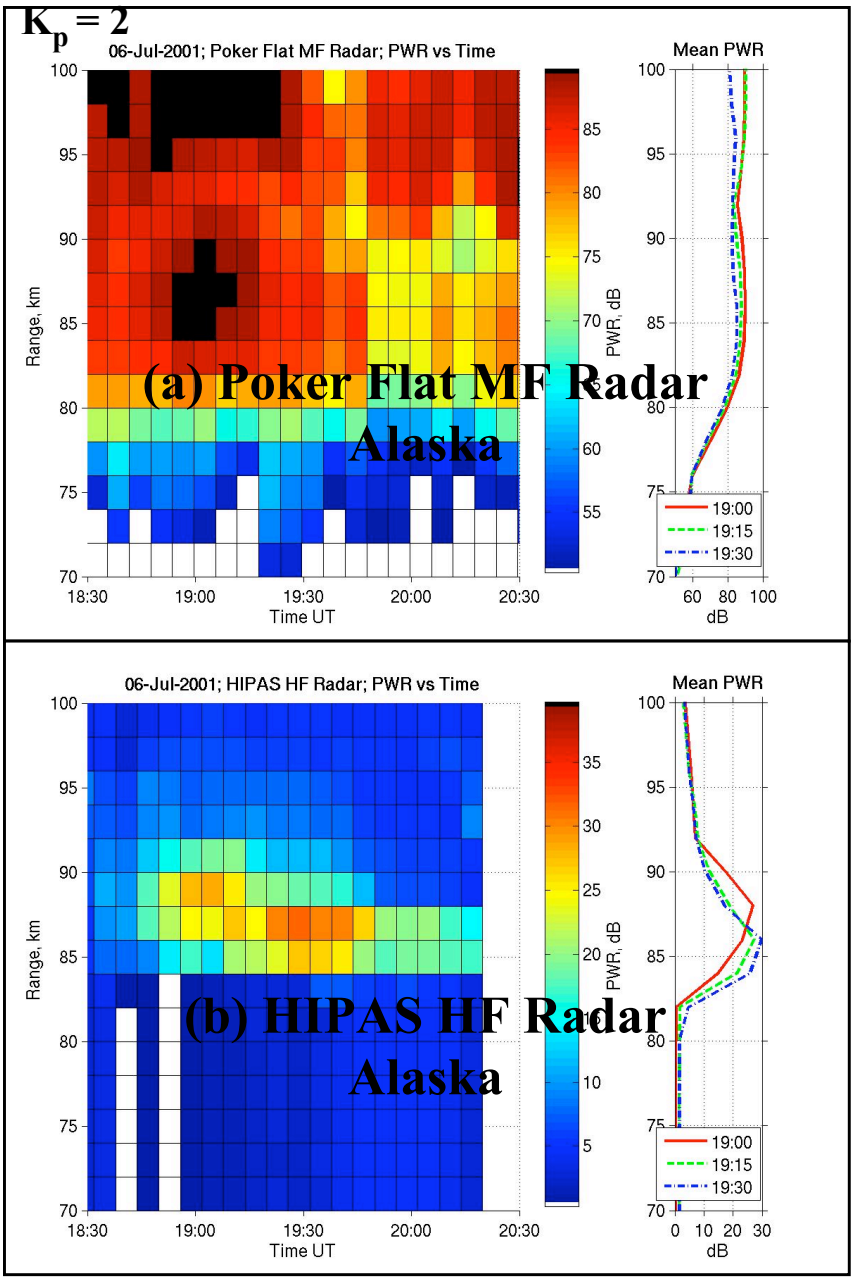

Figure 3.5: Concurrent radar observations at (a) Poker Flat (MF/2.43 MHz) and (b) HIPAS (HF/4.53 MHz) [July 6, 2001; 18:30-20:30 UT]. The solar geomagnetic index was reported as $k_p = 2$ for the same interval of time.

2001 results from Poker Flat and HIPAS motivated further radar observations for the upcoming summer seasons. We knew that PMSE was detectable at MF and HF frequencies but more data were necessary to support and explain our findings.

3.3.2 Winter/Summer Comparisons

Studying PMSE primarily at HF forced us to answer one fundamental question: are the HF mesospheric echoes exclusively detected during the summer season? The answer is yes. Figure 3.7a shows two 1-hour mean HF SNR profiles obtained from data collected at HAARP during one summer and one winter day (July 03, 2003 and March 25, 2004, respectively). Both measurements were obtained using the same transmission frequency (4.9 MHz) and during similar local times (19-20 UT). Although a very weak enhancement in radar signal is observed in the non-summer profile, the summer profile is evidently different with a maxima of 27 dB at 86 km. The on-site digisonde reported foE of 2.81 and 2.92 MHz during the non-summer and summer observational periods, respectively. There is no question that the summer echoes are PMSE. Other analyzed winter HF measurements showed a similar behavior during the time of the radar campaign, approximately 2 weeks. Figure 3.7b shows a similar type of comparison but using MF data from the Poker Flat MF radar. The summer mean power profile peak was found near 86 km while the non-summer peak was found near 78 km. A global view of the MF radar data used to produce the two profiles in 3.7b is shown in 3.8 but as an RTI (Range-Time-Intensity) plot. Although the mean power profiles shown in the right panels of Figure 3.8 were found using data only between 18 and 19 hours, the entire data set covers 12 hours of radar observations. Again, the non-summer MF data show a majority of signal peaks near 78 km while the summer data peaked near 86

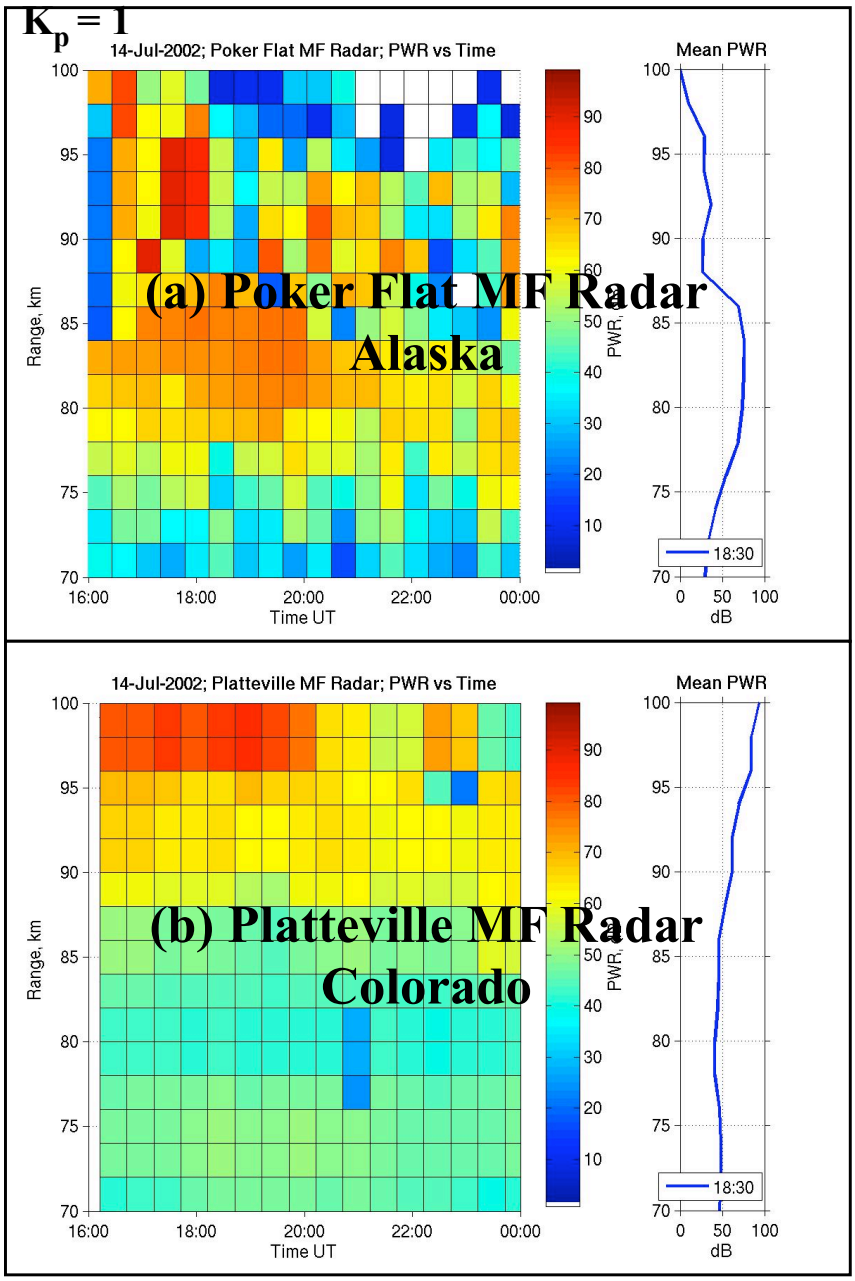

Figure 3.6: Concurrent MF radar observations over (a) Poker Flat, Alaska, and (b) Platteville, Colorado [July 14, 2002; 16:00-24:00 UT].

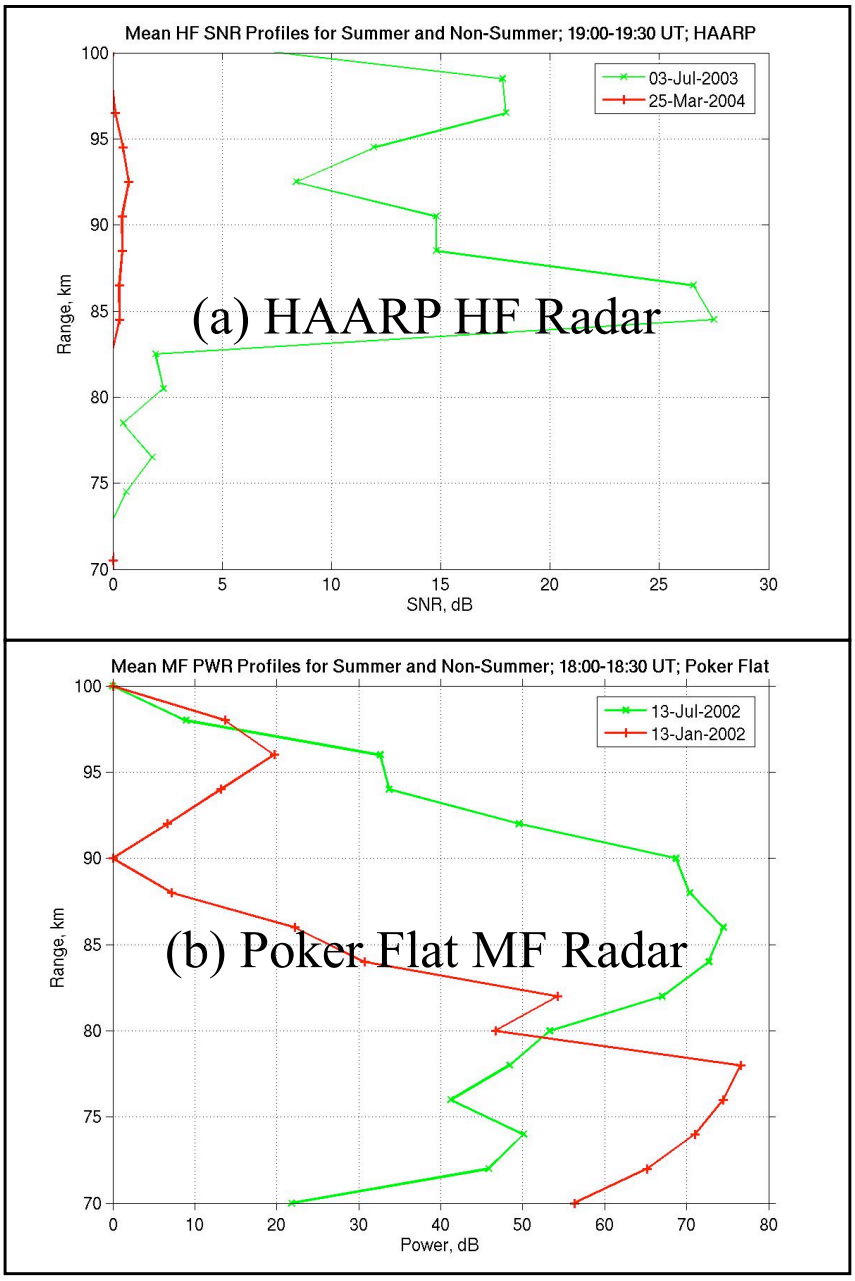

Figure 3.7: (a) HF/4.9 MHz radar mesospheric backscattered signal versus altitude for summer and non-summer periods, (b) Same inter-seasonal comparison but at MF/2.43 MHz.

km. Different from Figure 3.7, the mean backscattered signal profiles in 3.8 are displayed in linear units to emphasize the altitude of the mean power peak.

3.3.3 Climatology Studies of PMSE

Once the identity of the HF echoes was established as PMSE or non-PMSE echoes, we proceeded to conduct routine observations on as many days as possible. This gave us a broader view of PMSE phenomena. There is only one known long-term study of PMSE, which was carried out between 1979 and 1980 with the old Poker Flat VHF radar, which is no longer in operation [Ecklund and Balsley, 1981]. The characteristics of this database is described extensively in Chapters 1 and 2. In summary, VHF PMSE occur between late-May and mid-August, and between approximately 80 and 95 km. Non-summer mesospheric echoes occur as well but are relatively weaker compared to the summer ones and at lower altitudes, between 60 and 80 km approximately.

Radar operations at HF facilities are generally more difficult than at higher frequencies, e.g., VHF, mainly due to the transmitters' high manpower requirements and energy consumption. Portable and much smaller systems are commonly employed at VHF. The HF radar time is then constricted to budget availability. Our HF radar operations ended up being roughly 20 days during the summer 2002 at HIPAS, 20 days during summer 2003 at HAARP, and 5 days during winter 2004 at HAARP. Most radar runs took place between 18 and 22 UT (10 and 14 LT) and the selected days had to be coordinated in advance with the management and transmitter operations crews at HIPAS and HAARP. The author was responsible for the design and operation of the HF receiving stations at HIPAS and HAARP.

Fortunately, we had access to daily data from the nearby Poker Flat MF radar

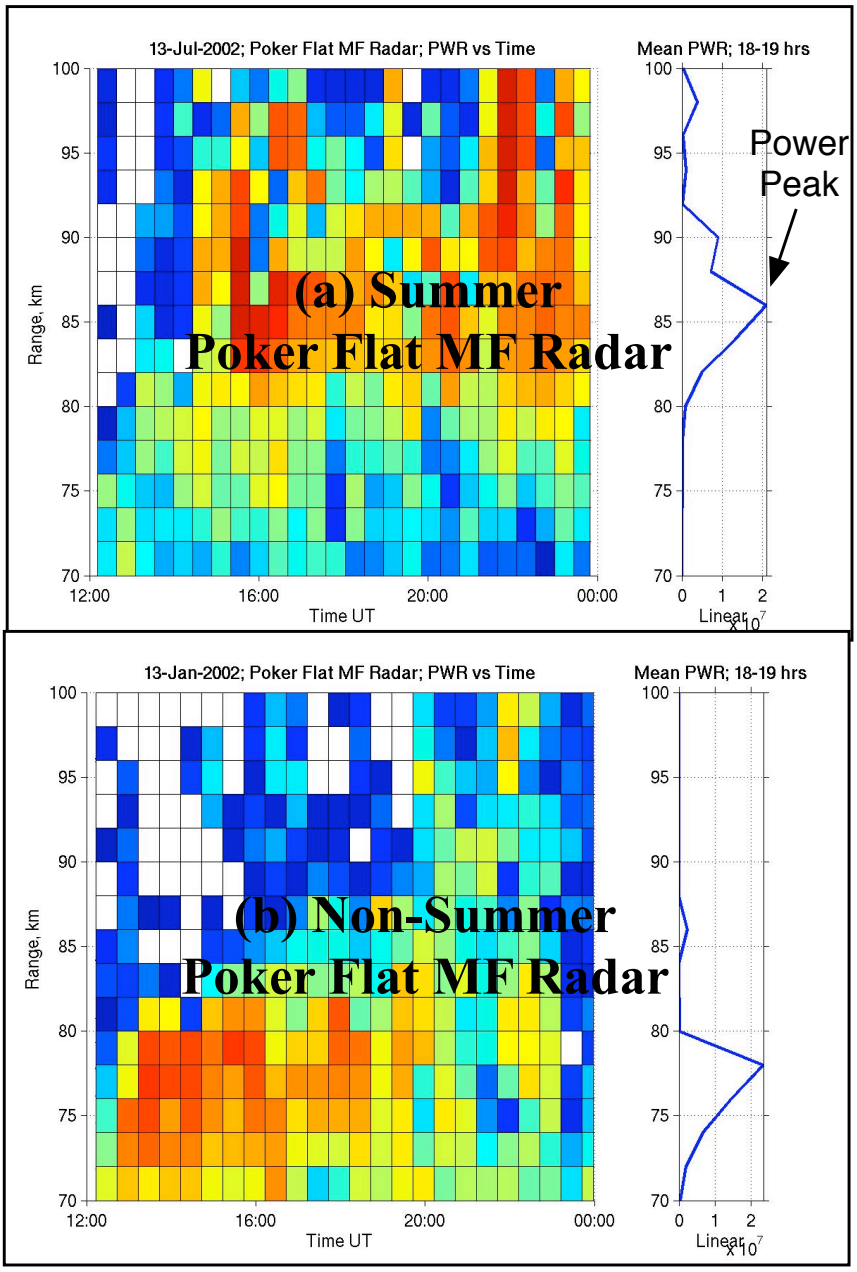

Figure 3.8: Typical MF radar power profiles for (a) summer and (b) non-summer periods [July 13, 2002 and January 13, 2002; 12:00-24:00 UT].

at Chatanika, Alaska, which enabled us to analyze two complete years of MF radar data, 2002 and 2003, on a daily basis with a 2-minute temporal resolution. We discuss the MF data sets, along with concurrent HF data from HIPAS/Summer 2002 and HAARP/2003, in the next sub-sections. The HF data sets from HAARP are discussed as case studies along with concurrent observations made with temporary VHF radars deployed at the Gakona, Alaska site and MF data from Poker Flat.

MF Results: 2002-2004

MF radar information is normally displayed as backscattered power versus altitude, instead of SNR, due to the difficulty in establishing a noise level with those systems. The backscattered signal amplitude increases quasi-linearly with altitude, as a result of partial reflections that occur worldwide across all seasons, which are produced by the ambient mesospheric ionization. This makes PMSE detection a difficult task at low frequencies and particularly in the MF band where the radar frequency is near the plasma frequency. However, we have found instances when mesospheric echoes clearly show up in the radar data without any ambiguity. Examples are shown in Figures 3.7 and 3.8.

Figure 3.9a shows post-processed Poker Flat MF radar data from two complete years (2002 and 2003) from altitudes between 60 and 100 km. For this type of analysis we have counted the number of power peaks in MF radar signal per day and displayed it as a function of height and time. This plot is quite similar to the original seasonal plot of VHF echo occurrence presented by Ecklund and Balsley [1981] (Figure 3.9b) in which an abrupt increase in echo occurrence occurred during the summer months of 1979 and 1980.

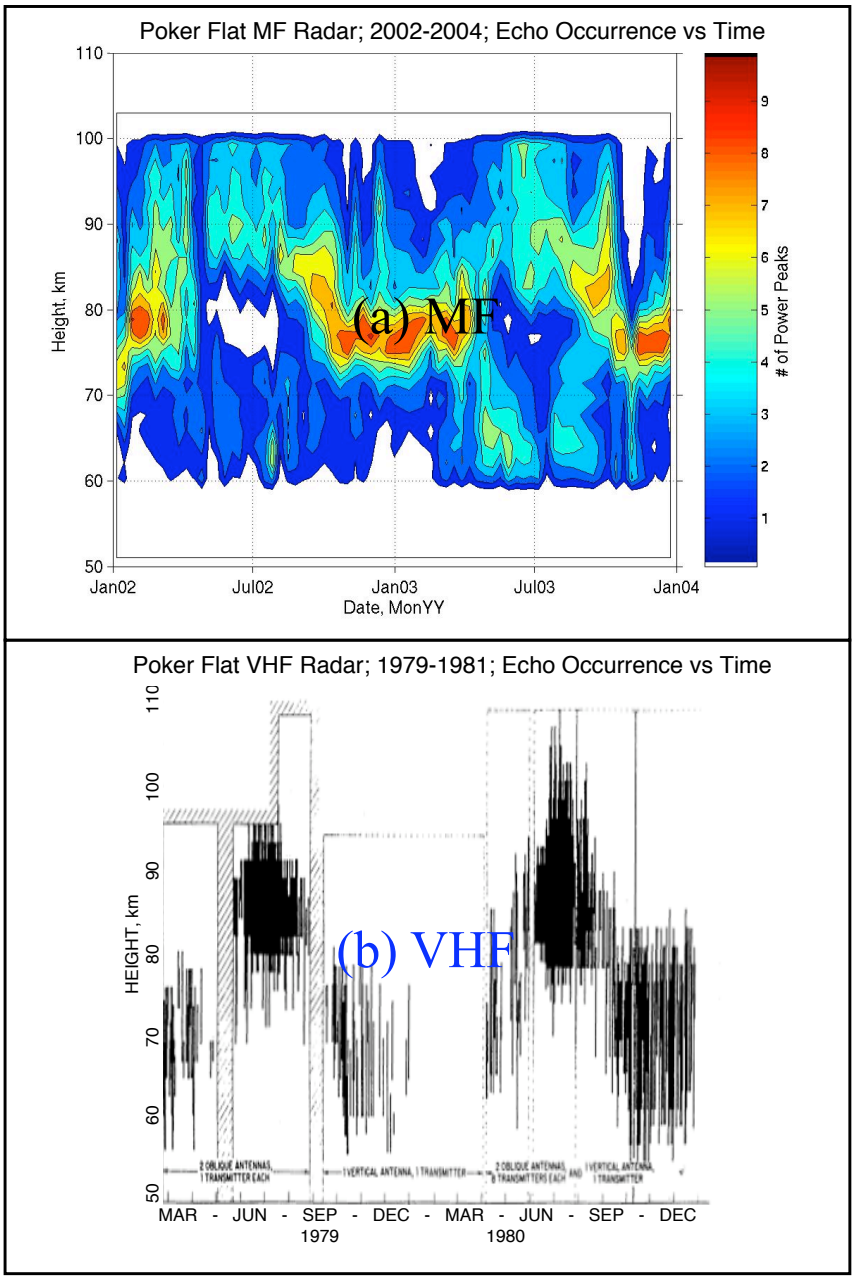

Figure 3.9: (a) Long-term distribution of MF radar mesospheric echoes (or "power peaks") over Poker Flat, Alaska [January 1, 2002 - January 1, 2004], (b) Similar analysis but at VHF [Ecklund and Balsley, 1981].

Both frequencies show similar seasonal trends in echo distribution although the MF results show higher organized non-summer structures. The summer months, i.e., May to August, show that the majority of MF peaks occurred between 85 and 95 km (top panel) in agreement with the VHF results (bottom panel). Non-summer MF peaks occur more often between 75 and 80 km. The non-summer results, although slightly higher in altitude, seem to match the Poker Flat VHF database well when the receiving and transmitting antennas were both pointed to the vertical, as is the standard mode of operation of the Poker Flat MF radar. We discuss characteristics and possible implications of the non-summer MF echo enhancements in Chapter 5.

Mesospheric Winds

For completeness we show mesospheric wind measurements obtained with the Poker Flat MF radar for 2002 (Figure 3.10). Summer and non-summer trends in global circulation can be readily verified with the zonal and meridional wind data displays, in the top and bottom panels, respectively. Notice the remarkably strong, westward, zonal wind current during the summer months, the so-called mesospheric jet stream, which acts as an "eastward mean flow" gravity wave directional filter [Kelley, 2006]. The latter sets up a southward motion at the upper boundary of the mesosphere, producing the wind driven refrigerator discussed in Chapter 2, which can explain the low temperatures experienced at mesopause altitudes during the summer season. An inverse effect occurs in the polar winter mesosphere, as indicated by the mean zonal and meridional wind profiles.

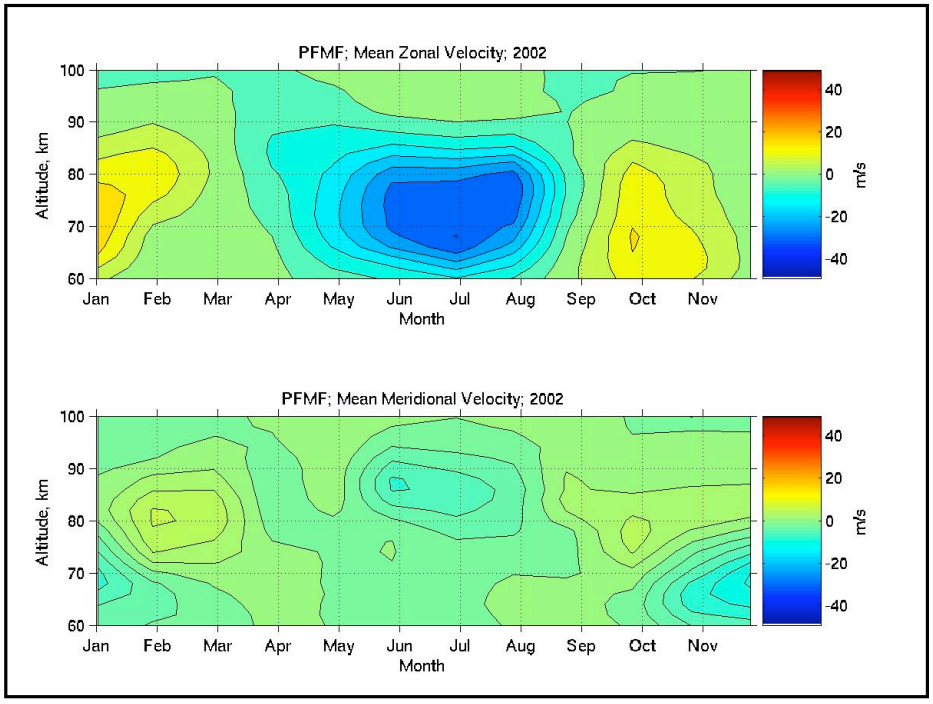

Figure 3.10: Seasonal distribution of zonal wind (top panel) and meridional wind (bottom panel) versus altitude over Poker Flat, Alaska, for year 2002. Eastward and northward winds are indicated by positive values.

MF/HF Seasonal Comparisons

After having extensively described MF radar observations we turn to inter-frequency comparisons. As indicated previously, the HF measurements were limited to 20 days during the summer of 2002, 2 hours per day. For comparison purposes we analyzed Poker Flat MF data from the same 20 days and times (19-21 UT). Due to the close proximity of Poker Flat and HIPAS (approximately 50 miles), the data gathered in both places are nearly collocated as they are collected under similar ionospheric conditions. Figure 3.11 shows seasonal backscattered power profiles from the two radars, Poker Flat/MF (3.11a) and HIPAS/HF (3.11b), respectively. The legend shows radar operational days. Each power profile represents the mean of a 2-hour data segment. The mean power profile for each seasonal database is plotted as a dashed line in both panels. Times without echo activity were discarded from the individual daily power profiles.

The HF results (Figure 3.11b) are certainly easier to interpret, with the mean power profile having a peak at approximately 86 km, as expected for PMSE. That is not the case with the MF data, where the mean power profile does not show a clear local maxima in the backscattered signal but only a very weak enhancement between 85 and 90 km. Many individual power profiles show some similarities in ionospheric conditions, at both frequencies, although no one to one correspondence can be established from a comparison of both mean seasonal profiles. The two databases seem to indicate that the more active echo periods within the summer season are the last week of June and first week of July, although the lack of continuity in measurements prevents further conclusions. This result is in solid agreement with previous PMSE studies, in which maximum detection occurred during the first week of July. In summary, seasonal PMSE characteristics can

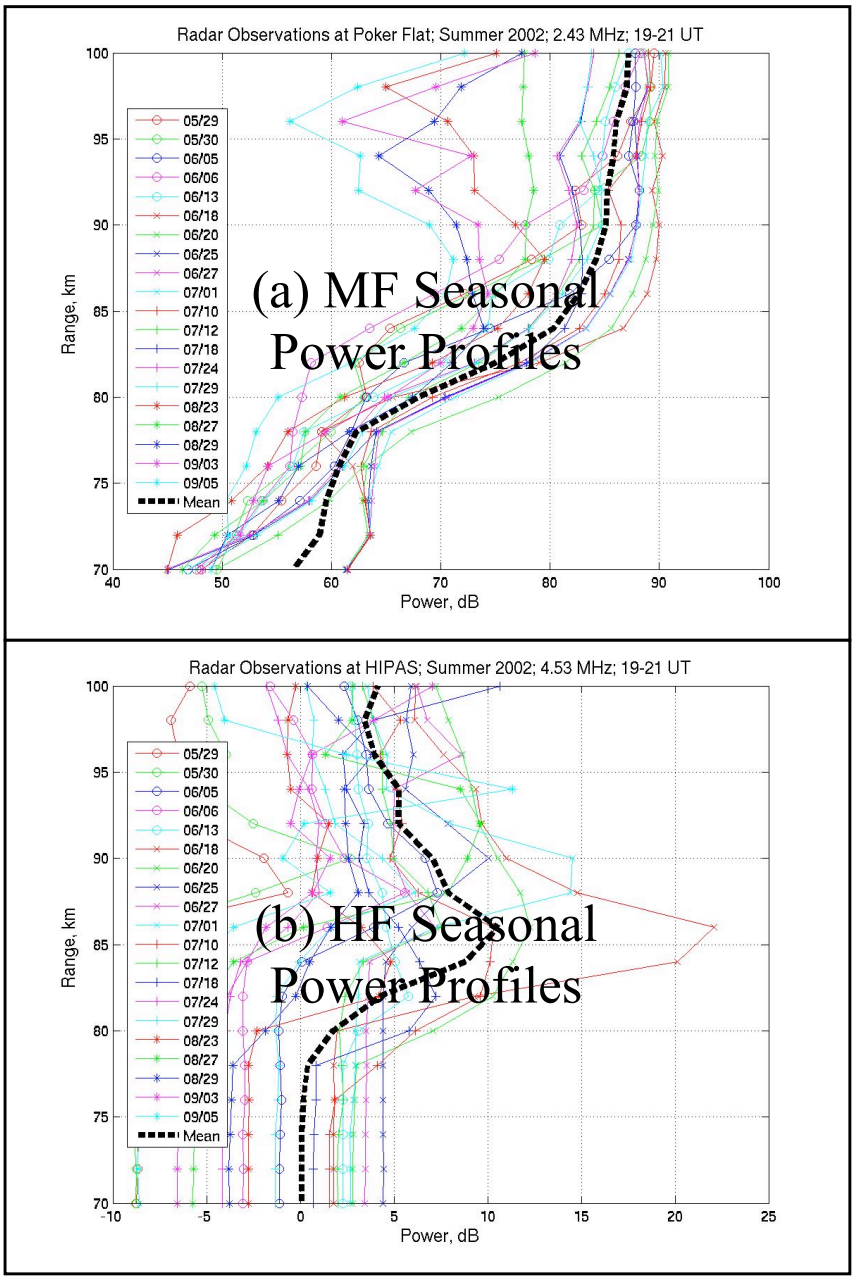

Figure 3.11: Concurrent radar observations at (a) Poker Flat (MF/2.43 MHz) and (b) HIPAS (HF/4.53 MHz). Each power profile represents the mean of a 2-hour data segment (19-21 UT). The mean power profile for each seasonal database is plotted as a dashed line in both panels.

be inferred roughly from seasonal HF radar measurements. The situation with MF radar data is different because although many individual power profiles show similarities with concurrent HF profiles, a clear indication of PMSE can not be inferred by considering the seasonal mean power profile. Strong MF radar returns from altitudes above 90 km seem to produce a "hiding" effect in PMSE echoes, which are expected to occur at lower altitudes or between 80 and 90 km.

MF/HF Diurnal Comparisons

Finally, we show MF/HF concurrent data from a full day radar run (July 29-30, 2002; 18-18 UT), which took place at Poker Flat and HIPAS. Two 24-hour HF runs were conducted during the summer of 2002, July 24-25 and July 29-30, but we only discuss the second one in this thesis because the first run was very quiet and few PMSE echoes were detected. Figure 3.12 (top panel) shows continuous MF radar power data from Poker Flat, starting on July 29, 2002,c18 hours UT and finishing on July 30, 2002, 18 hours UT (next day). Data from the same time interval is shown in Figure 3.12 (bottom panel) for the nearby HIPAS HF facility, but as signal-to-noise versus time. Significant fluctuations in HF noise level make it inconvenient to display the HIPAS data as power versus time.

We describe the MF diurnal observation first. An automatic gain device connected to the MF receiver makes the backscattered power signal smaller between approximately 02 and 14 hours UT. The daylight electron density levels seem to be delineated by the upper red/orange patches of power signal (above 90 km) but instances occur when the backscattered signal peak moves down to lower altitudes (between 80 and 90 km). Again, signal enhancements (or PMSE candidates) cannot be clearly identified from the diurnal MF power data. Turning to the HF

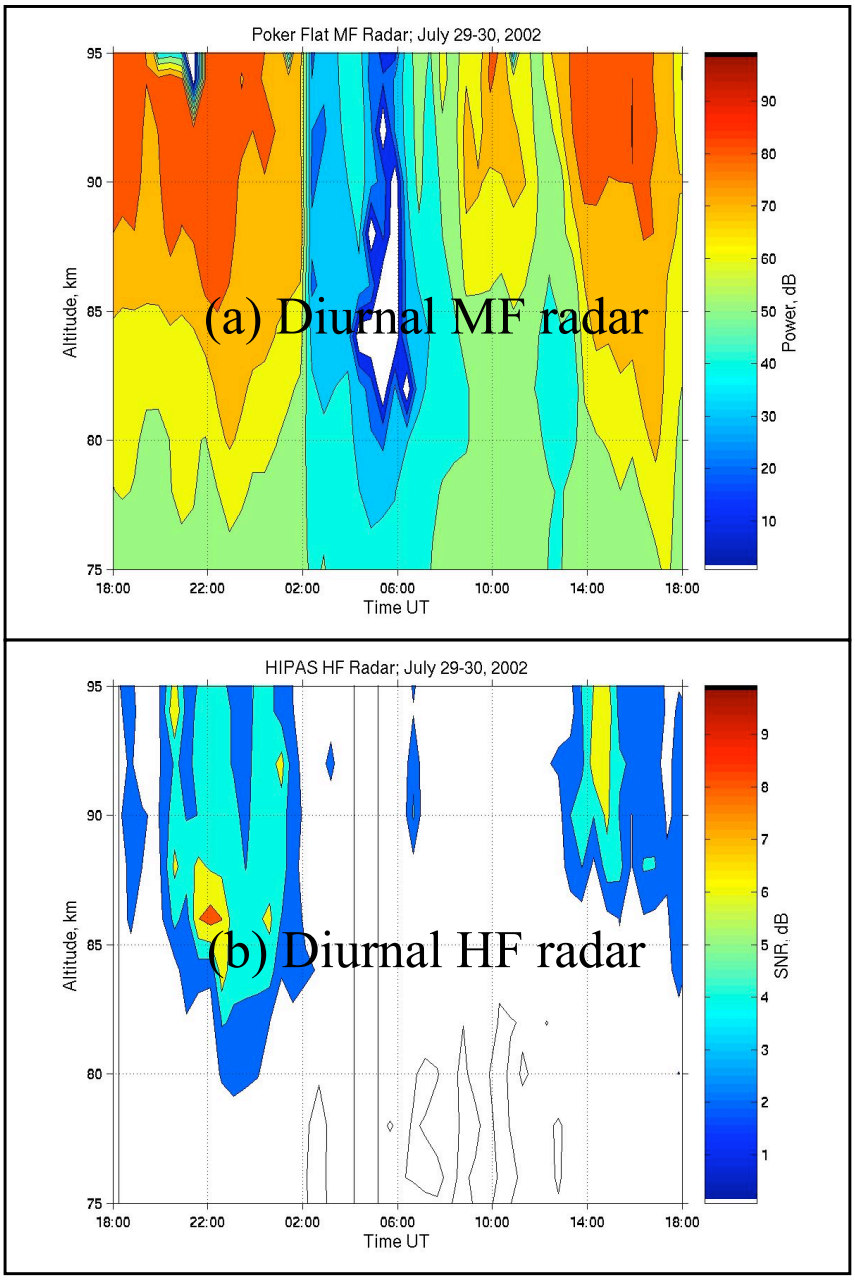

Figure 3.12: Diurnal MF backscattered power (top panel) and HF signal-to-noise ratio (bottom panel) for (a) Poker Flat and (b) HIPAS [July 29/30, 2002, 18-18 UT].

results, we should mention first that, due to the high nighttime noise levels experienced by the HF receiver, SNR values are negligible after 02 UT (18 LT, July 29th) and before 14 UT (06 LT, July 30th). Daytime occurrences of mesospheric HF echoes are more uniform, with a sharp maxima between 20 UT (noon local time) and 22 UT, in agreement with previous VHF PMSE work. In general terms, many similarities are evident from a comparison of MF and HF diurnal data sets, specially during daytime hours. PMSE discrimination is certainly more easily performed on the HF data, where mesospheric signals appear unconnected from higher altitude phenomena. Although general ideas and conclusions can be drawn from the analysis of seasonal and/or diurnal radar data, details on the nature of mesospheric radar echoes can only be acquired from the analysis of specific events with higher temporal resolutions.

3.3.4 Multi-frequency Observations: Case Studies

In this section we present examples of PMSE events observed concurrently at various frequencies. The goal is to prove that PMSE is indeed detectable in the MF and HF bands. First we link HF echoes to simultaneous VHF radar detections, the reference sensors traditionally employed for PMSE studies. Then, we extend inter-frequency comparisons to the MF, HF, and VHF bands. A total of seven case studies are described with PMSE observed concurrently with at least two radar systems. Absorption and mesospheric wind data are employed to explain signal fluctuations and time delays between PMSE events observed at different radar sites.

Comparison of HF with higher frequency observations

An example of a PMSE event observed with three radar frequencies (4.9, 28, and 50 MHz) is shown in Figure 3.13. The top panel shows a typical HF signal we believe to be PMSE [Kelley et al., 2002]. The bottom panel shows two VHF data sets, i.e., 28 and 50 MHz, collected simultaneously during HF transmissions. Integrations times for HF (4.9 MHz) and VHF (28 and 50 MHz) data are 3 and 6 seconds, respectively. The 28 MHz radar data are displayed as a colored image. In the over-plot, we can see contours representing the 50 MHz radar data. Each VHF radar data set was normalized, with respect to the signal peak, to facilitate the data comparisons. It is clear that three radar measurements, i.e., 4.9/28/50 MHz, are closely related. Since VHF radars are the accepted marker for PMSE, this comparison is definitive evidence that PMSE can be detected reliably by HF systems such as those at HAARP, HIPAS, and the Russian site SURA [Karashtin et al., 1997]. A high absorption event caused the HF/4.9 MHz signal to disappear during the second half hour ($\sim$18:30 UT) as indicated by the Poker Flat imaging riometer, which covers an area of 200 km by 200 km (Figure 3.14). The HF signal was significant up to about 88 km. The old Poker Flat VHF radar [Ecklund and Balsley, 1981], which was more sensitive than the VHF radars used here, also found echoes up to such heights. The PMSE altitude of the peak signal was virtually the same for the three radars, $\sim$82 km.

Figures 3.15 and 3.16 show two additional examples of clear HF PMSE echoes occurring simultaneously with VHF PMSE. The first set of plots (Figure 3.15, July 14, 2003, 18-19 UT) show PMSE layers at around 83 km in the two frequencies. A highly disturbed ionosphere above 90 km is evident from the HF data, which is in agreement with an E-layer reported by the HAARP ionosonde for that same

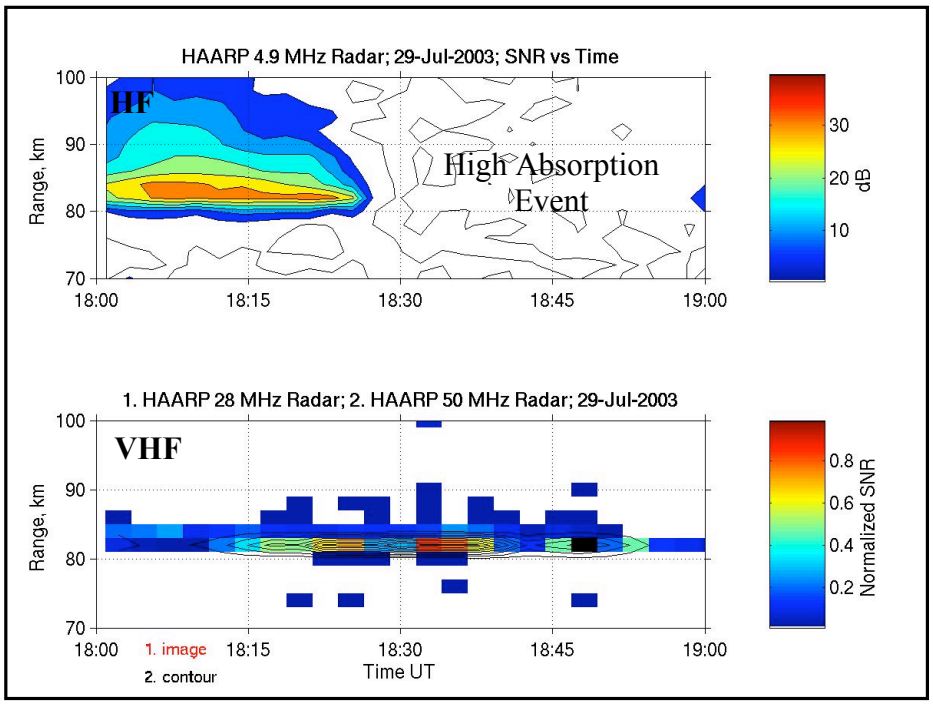

Figure 3.13: Concurrent HF/VHF radar observations at HAARP [July 29, 2003; 18:00-19:00 UT].

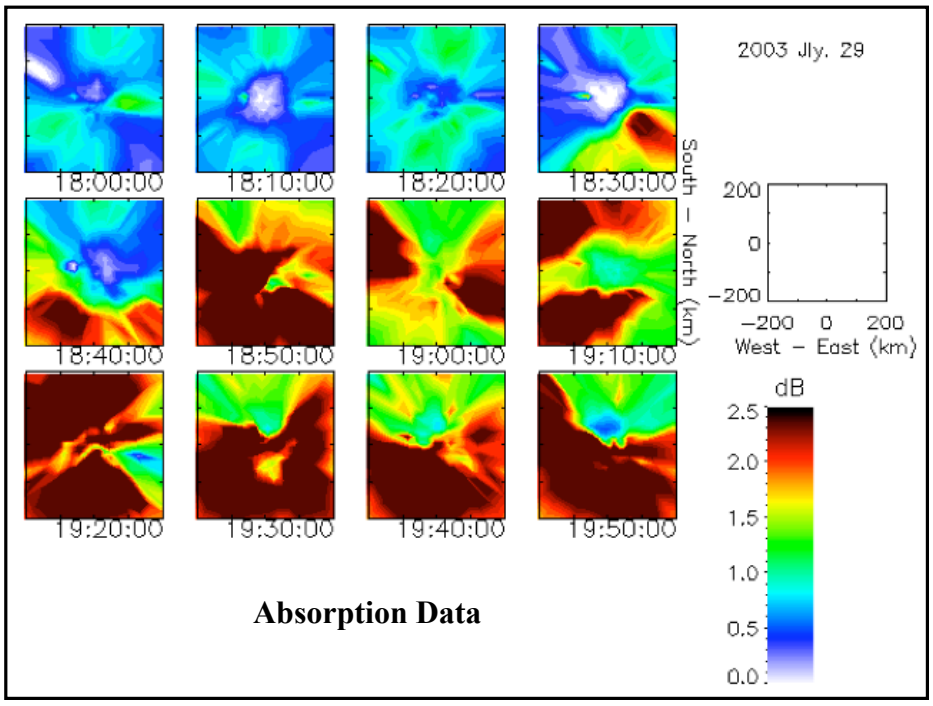

Figure 3.14: Poker Flat imaging riometer [July 29, 2003, 18:00-20:00 UT].

time interval. The higher electron density levels above 90 km seem to enhance the scattering of the lower PMSE layer, particularly at HF. Figure 3.16 (top panel) shows an almost continuous HF PMSE layer accompanied by a much weaker and sporadic VHF PMSE (bottom panel). Both data sets were collected at HAARP on July 16, 2003. Unfortunately, the HF radar scheduled time finished at 22 hours, just a few minutes after the VHF echoes began to show up! In any case, both radars gave good indications of PMSE processes occurring near 88 km of altitude.

Comparison of MF with higher frequency observations

A much less convincing MF/HF PMSE event is presented in Figure 3.17a (top panel) while the HF layer is very clear (3.17a, bottom panel). Figure 3.17b shows selected power profiles for the MF/HF data sets. One of the mysteries about which

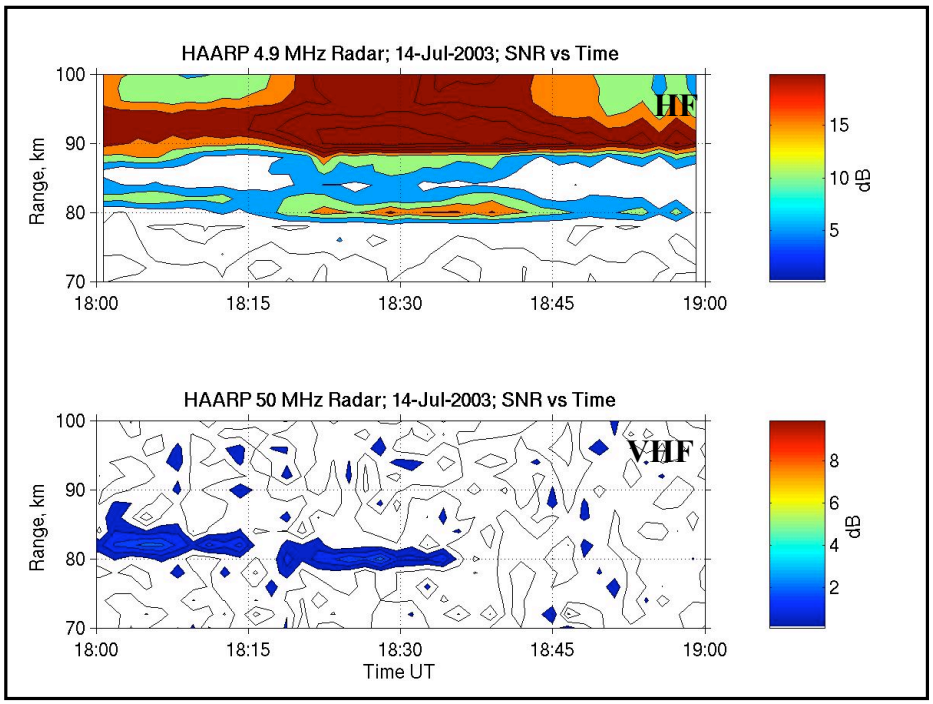

Figure 3.15: Concurrent HF/VHF radar observations at HAARP [July 14, 2003, 18:00-19:00 UT].

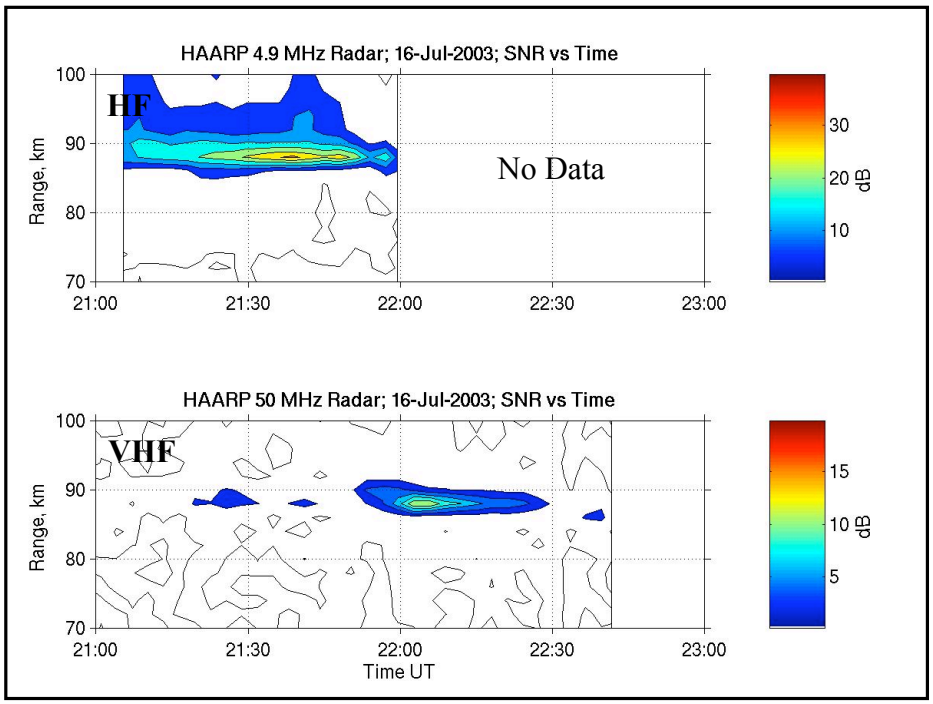

Figure 3.16: Concurrent HF/VHF radar observations at HAARP [July 16, 2003, 21:00-23:00 UT].

we can only speculate is why a frequency change of only a factor of 2 makes such a difference to the signal character. A possible clue to this difference, at least at high latitudes, is indicated by the magnetic activity index, k_p, shown in the upper left side of the MF plot. The k_p index was much higher in the time period corresponding to Figure 3.17 than for the previous MF examples shown (Figures 3.5 and 3.6). Also, HIPAS has much more power than the MF radar, and the sky temperature is much lower than that at 2.43 MHz.

Figure 3.18 presents another example of MF/2.43 MHz data from Poker Flat along with HAARP 4.9/139 MHz data. Integration times for the 2.43, 4.9, and 139 MHz data sets are 120, 3, and 30 seconds, respectively. Notice the different scales between the three panels. Absorption data from the imaging riometer at Poker Flat, and wind components observed with the MF system are shown for the same period in Figures 3.19 and 3.20, respectively. The unambiguous HF and VHF patches after 1845 are preceded by weaker echoes at HF and a strong patch in the MF data. At 19:15 UT the absorption increased and the MF signal almost completely disappeared. The absorption step was only 1 dB and seems not to have affected the HF signal. It is interesting that the time delay between the MF patch at Poker Flat and the strong layers at HAARP is consistent with the magnitude and direction of the meridional wind velocity shown in Figure 3.20.

Two more examples of simultaneous data at MF and at two VHF frequencies are presented in Figures 3.21 and 3.22. Notice the different scales between the data sets. Although less convincing than Figure 3.18, enhanced MF echoes are seen as part of the time at the same altitude as the unambiguous VHF signals.

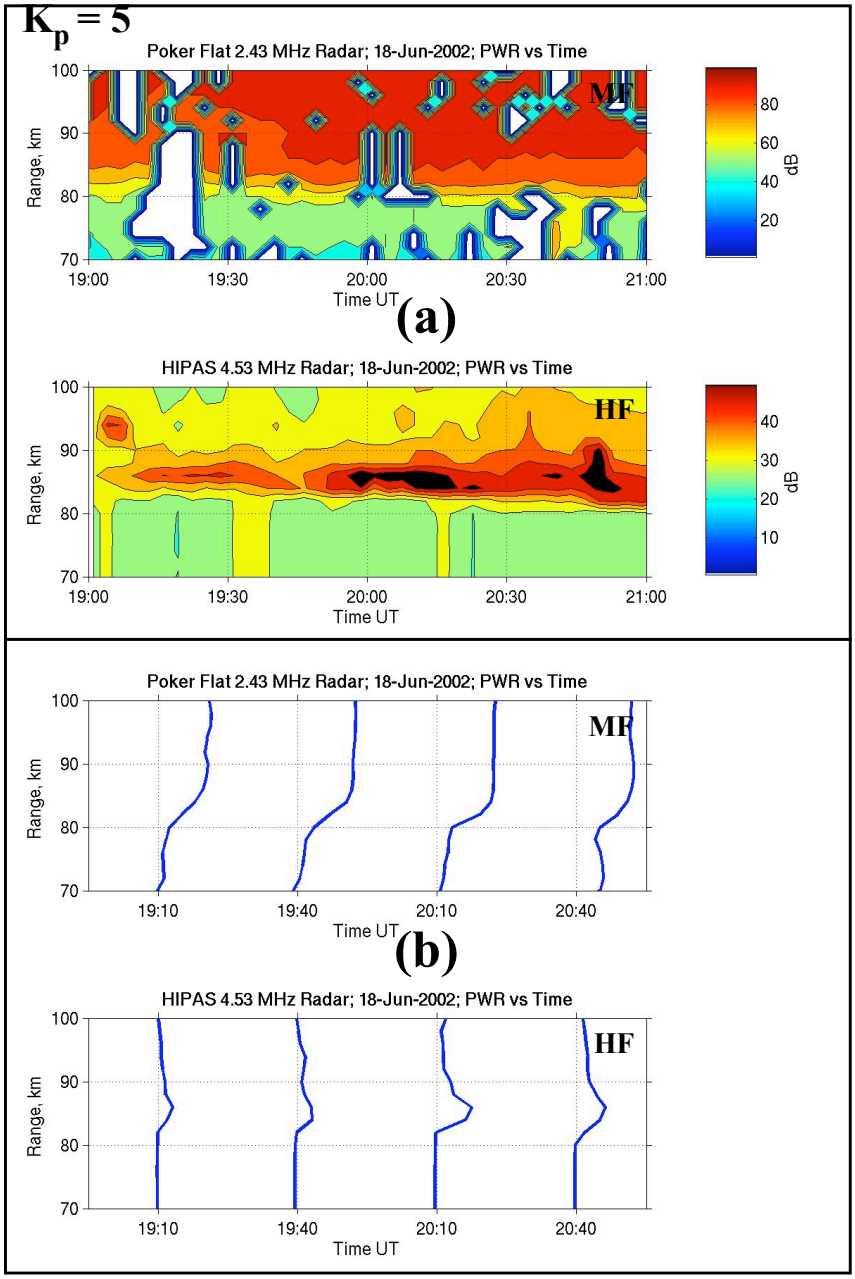

Figure 3.17: (a) MF/2.43 MHz and HF/4.53 MHz radar observations during high k_p conditions [June 18, 2002, 19:00-21:00 UT], (b) Average power profiles for 15-minute data segments centered at 19:10, 19:40, 20:10, and 20:40 UT.

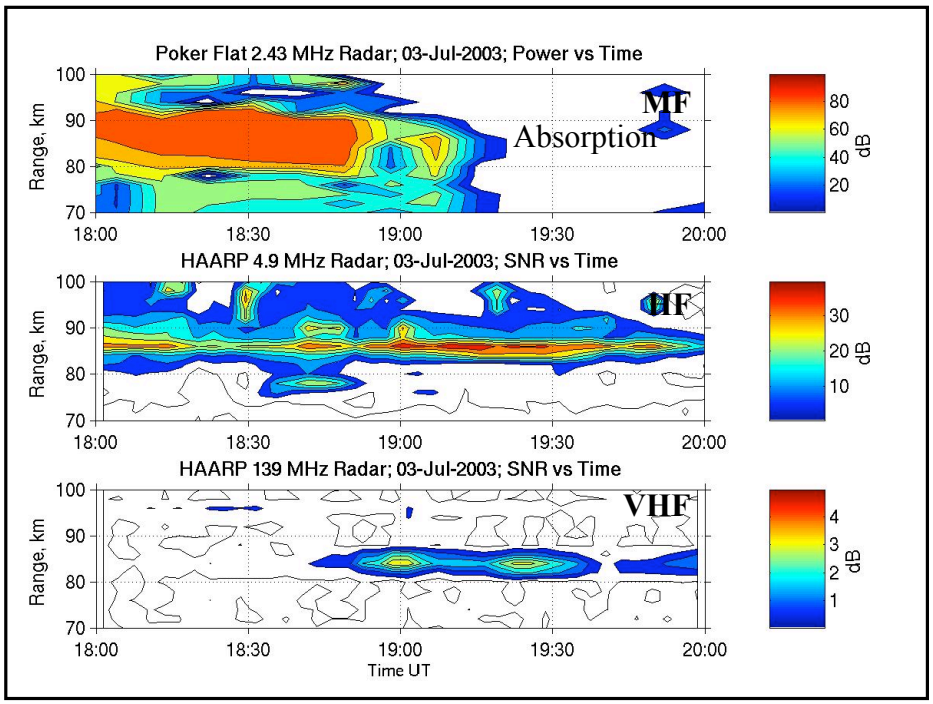

Figure 3.18: PMSE observed at three frequencies: 2.43/4.9/139 MHz [July 03, 2003, 18:00-20:00 UT].

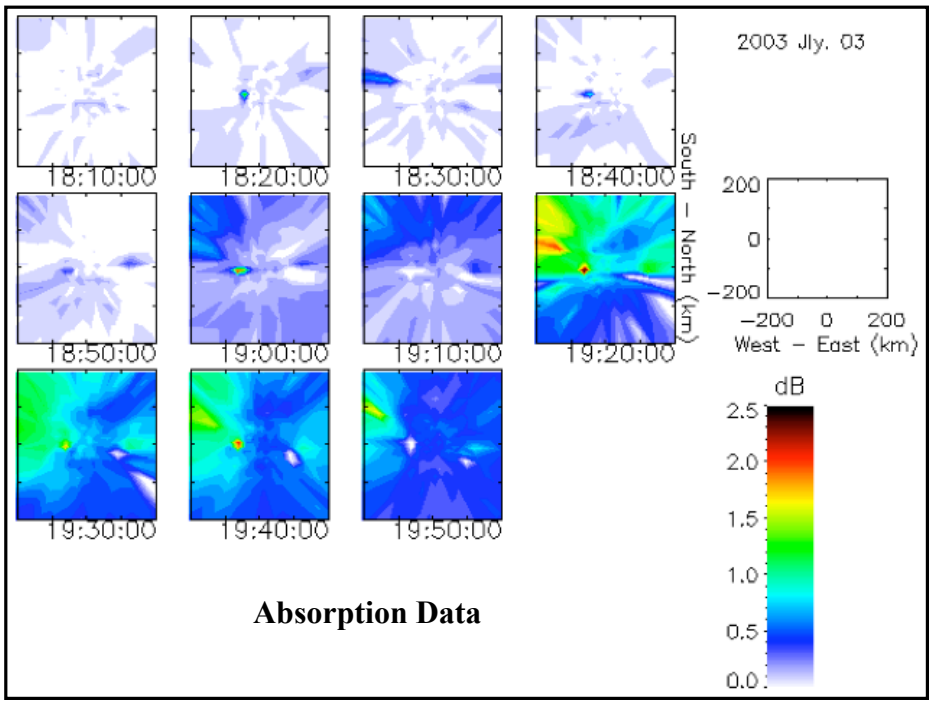

Figure 3.19: Poker Flat imaging riometer [July 03, 2003, 18:00-20:00 UT].

3.4 Summary

In this chapter we have presented definite evidence that HF radars can be used to reliably detect PMSE. This conclusion is based on several inherent features of the HF data including the altitude, layered nature, seasonal behavior, and signal strength of the echoes. The comparison of MF and HF radar observations with simultaneous VHF PMSE detections were key factors in understanding the identity of the echoes at the lower frequency bands. In addition, we have shown that MF "wind profiler" systems at high latitudes receive enhanced and layered scatter from the region associated with PMSE. Anomalous ionospheric absorption events and high geomagnetic activity explain the paucity of PMSE in the MF data and/or the fragmented nature of the observed layers.

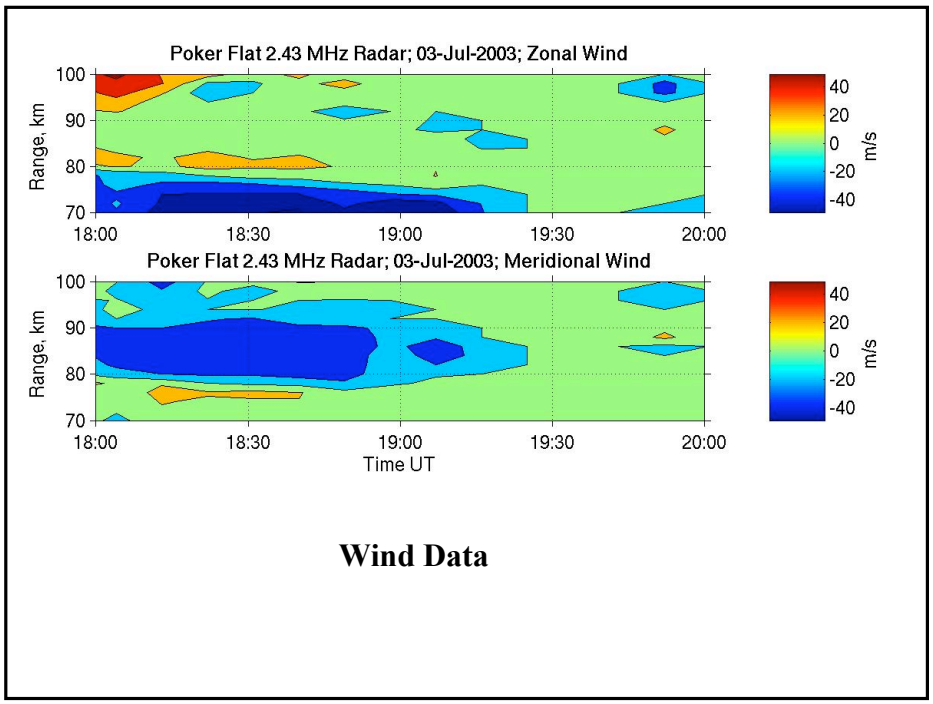

Figure 3.20: Zonal and meridional mesospheric winds over Poker Flat [July 03, 2003; 18:00-20:00 UT].

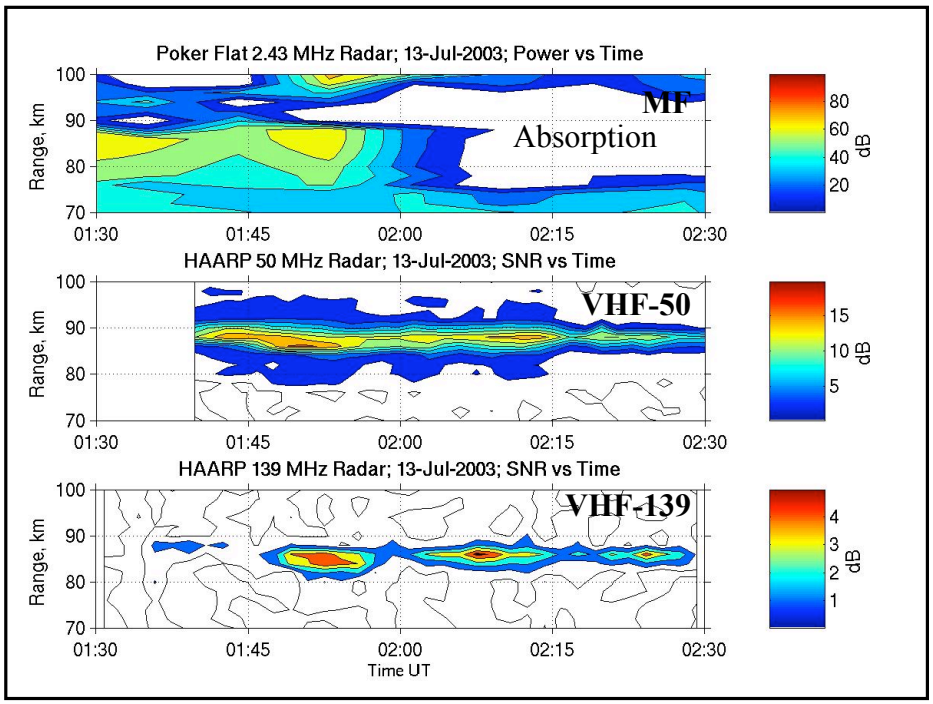

Figure 3.21: PMSE observed at three frequencies: 2.43/50/139 MHz [July 13, 2003; 01:30-02:30 UT].

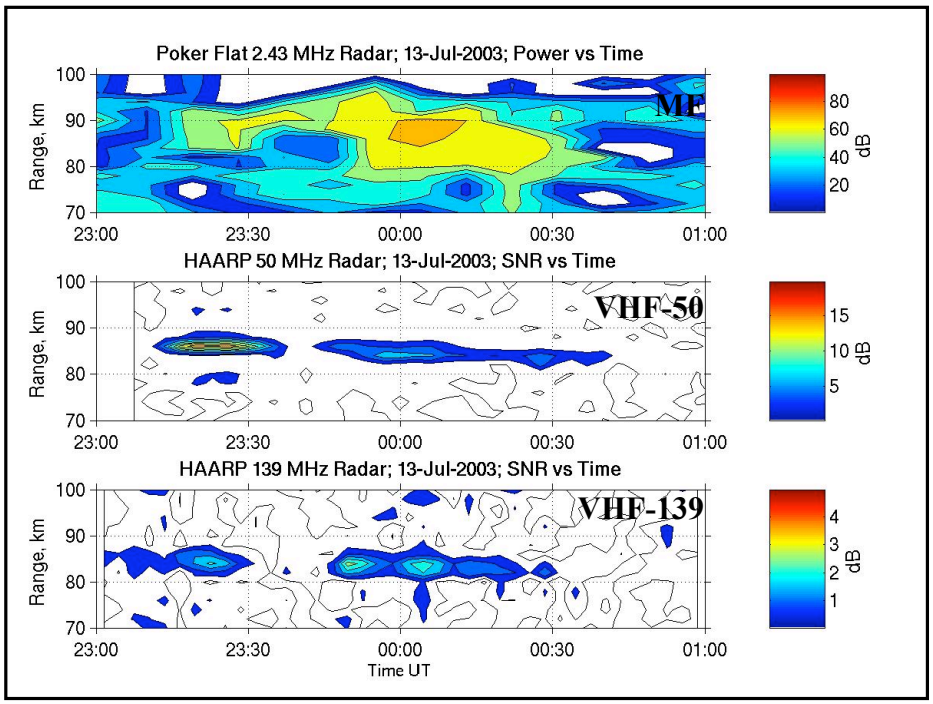

Figure 3.22: PMSE observed at three frequencies: 2.43/50/139 MHz [July 13, 2003; 23:00-01:00 UT].

Chapter 4

Radar Scattering Predictions from Rocket Soundings

In this chapter we complement our radar observational databases with numerical predictions of radio-wave scattering at different frequencies. For that purpose, we have chosen to analyze in-situ data from rocket soundings taking place during PMSE and non-PMSE seasons. Knowing that coherent scatter radars are sensitive to two different types of scattering mechanisms – sharp of edges of electron density and turbulent mediums – we employ the Wavelet transform as a mathematical tool to isolate edge and turbulent components present in electron density data. Scattering theory is used to estimate effective radar reflectivity and radar volume reflectivity for each appropriate echo contributor at MF/HF/VHF frequencies. An overview of radar scattering theory applicable to the mesosphere is presented first. Then, we describe the analyzed rocket data and the scattering estimation methods. Finally, results for predicted radar refractivity as a function of wavenumber or radar frequency are presented.

4.1 Radar Scattering Theory

Ice particles and dust layers are examples of conditions that affect and enhance radar scattering in the upper regions of the mesosphere. PMSE radio backscatter is normally accepted as a superposition of turbulent and non-turbulent mechanisms producing irregularities in electron density near the mesopause region. In the next sub-sections we describe qualitative and quantitative aspects of coherent radio-

wave scattering that could be attributed to PMSE or any other coherent or non-thermal scatter phenomena.

4.1.1 The Radar Equation

Before discussing details about reflection or scattering mechanisms in the atmosphere we define some fundamentals necessary to understand radar derived information. The radar equation provides a relationship between the radar system parameters (i.e., transmitted power, frequency, antenna gain, etc.) and the received signal power produced by an object under observation. The radar target can be characterized by its radar cross section (RCS), which can be interpreted as an equivalent physical area that intercepts an incident power density and isotropically re-radiates that power. The RCS (σ, of units m^2) relates the incident power density ($S_i, \frac{watts}{m^2}$) to the reflected or scattered power ($P_s, watts$) as follows:

$$P_s = \sigma S_i. \tag{4.1}$$

The final power arriving to the receiving station, P_r, without including hardware losses, can be defined by the so-called radar equation for a solid or point target,

$$P_r = \frac{P_t G^2 \sigma \lambda^2 \alpha^2}{(4\pi)^3 r^4}, \tag{4.2}$$

where P_t is the transmitted power, G is the antenna gain ($G = \frac{4\pi A_e}{\lambda^2}$), σ is the radar cross section, λ is the radar wavelength, α is a one-way propagation loss, r is the target range, and A_e is the effective antenna area. The above equation is valid for mono-static radar systems.

For distributed targets or volume-filled scatter, as in the case of most atmospheric phenomena, equation 4.2 can be expressed in terms of radar reflectivity,

η, instead of radar cross-section, σ. The radar reflectivity of units m^{-1} for a distributed target is equivalent to its radar cross-section per unit volume and is expressed by

$$\eta = \frac{\sigma}{V}. \tag{4.3}$$

Two special cases of radar echoing mechanisms are: turbulent scatter, and specular reflection or edge scatter due to sharp transitions in the radio refractive index. Please refer to Appendix A.3 for detailed derivations of the next two equations. The radar equation for turbulent scatter can be found from 4.2 and 4.3 as

$$P_r = \frac{P_t A_e \Delta r \alpha^2}{16 r^2} \eta_{turb}, \tag{4.4}$$

where Δr is the radar range resolution. Similarly, for edge scatter, the radar equation is obtained as

$$P_r = \frac{P_t A_e^2 \alpha^2}{4 r^2 \lambda^2} |\rho|^2 \tag{4.5}$$

[Gage and Green, 1978; Röttger and Liu, 1978; Gage et al., 1981], where the received power is now expressed in terms of the power reflection coefficient, $|\rho|^2$. An extra gain term must be added to equation 4.2, termed scattering gain or G_s' by Gage and Balsley [1980], due to the preferred direction of edge scattering processes.

In the next two sub-sections we describe the physics behind turbulent and edge scattering processes, their generation mechanisms, and methods to calculate η_{turb} and $|\rho|^2$.

4.1.2 Turbulent Scatter

Radar waves scatter off signals coherently from the "clear" atmosphere as a result of macroscopic fluctuations of the radio refractive index of air ($\frac{\delta n}{\delta z}$). Equation 4.6 defines the refractive index, n, where p is the total pressure in mbar, T is the temperature in ^{o}K, e is the partial pressure of water in mbar, N_e is the electron number density in m^{-3} , and f_o is the radar operating frequency in Hz [Bean and Dutton, 1966].

$$n = 1 + 77.6 \times 10^{-6}\frac{p}{T} + 3.73{\cdot}10^{-1}\frac{e}{T^2} - 40.3\frac{N_e}{f_o^2} \tag{4.6}$$

Fluctuations in the second and third terms of Eq. 4.6 (known as dry and wet terms, respectively) contribute mostly to radar returns from the troposphere and stratosphere. At mesospheric altitudes the ionization term (last term of Eq. 4.6) is the major factor responsible for radar returns, where refractive index fluctuations are induced by neutral turbulence acting on the background plasma [Gage and Balsley, 1980].

Turbulent fluctuations of the refractive index produce radio wave scattering or what is known as "turbulent scatter". This is the dominant form of radio-wave scatter in the neutral atmosphere. The radar backscattered signal is predominantly from irregularities with scale sizes equal to the Bragg length (one half the radar wavelength, $\lambda_R/2$) or wavenumbers in the order of $k = \frac{4\pi}{\lambda_R}$. For Kolmogorov-type inertial range turbulence, coherent backscatter occurs between the inner and outer scale sizes of the turbulence, l_o and L_o, respectively. Figure 4.1 shows the energy distribution or the power spectral density of turbulence, $\phi_n(k)$, as a function of the wavenumber, k, or the inverse of the eddy size. Larger eddies supply energy to smaller eddies via nonlinear interactions. At scale sizes smaller than l_o (i.e., in

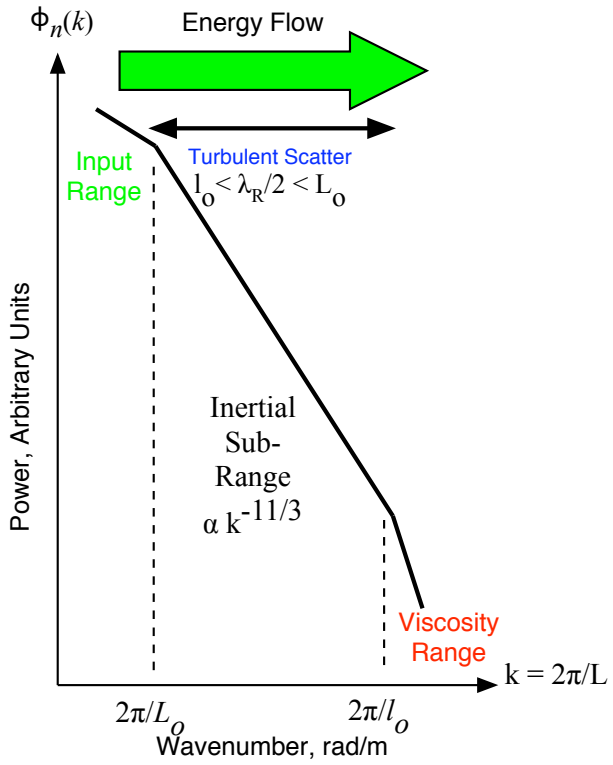

Figure 4.1: Power spectrum of refractive index fluctuations in a turbulent atmosphere. Adapted from Craig [2002].

the viscosity sub-range), turbulent fluctuations are attenuated by viscosity. The inner scale of turbulence increases as a function of altitude [Hocking, 1985]. The power spectral density falls off as $k^{-11/3}$ within the inertial sub-range.

The radar operating wavelength and the sampled altitude impose a limit for the detection of echoes ($l_o(z) < \frac{\lambda_R}{2} < L_o$, where z is altitude). For a given radar frequency, the chances of detecting echoes due to turbulent scatter increase as we move into lower altitudes. Similarly, at smaller radar frequencies (i.e., MF/HF versus VHF/UHF) the chances of detecting echoes produced by turbulence increase as a result of the higher content of turbulent energy at larger scale sizes.

The radar reflectivity for inertial range isotropic turbulence is generally expressed as

$$\eta = \frac{\pi^2}{2} k^4 \phi_n(k) \tag{4.7}$$

[Tatarskii, 1971], where the power spectrum, as a function of wavenumber, is given by

$$\phi_n(k) = 0.03 C_n^2 k^{-11/3}. \tag{4.8}$$

C_n^2 is known as the refractive index structure constant. Tatarskii [1971] expresses C_n^2 in terms of the mean gradient of refractive index M and the outer scale of turbulence L_o as

$$C_n^2 = 2.8 L_o^{4/3} M^2. \tag{4.9}$$

For the mesosphere, where refractive index fluctuations by electron density N_e are dominant, M is expressed by Röttger [2002] as

$$M = \frac{r_e \lambda^2}{2\pi}(N_e(\frac{\omega_B^2}{g} - \frac{d\rho}{\rho dz}) - \frac{dN_e}{dz}). \tag{4.10}$$

Different relations for the mean gradient of the refractive index can be found for the troposphere and stratosphere by considering the relevant atmospheric parameters in the two regions. The final expression for radar reflectivity produced by turbulence, in terms of C_n^2 and λ, is

$$\eta_{turb} = 0.38 C_n^2 \lambda^{-1/3}. \tag{4.11}$$

Turbulent scatter represents the dominant form of radio-wave scatter in the clear air atmosphere. These structures are generally isotropic in nature but can also be distorted in shape due to wind shears or other external forces. When this happens, the radar echoes can show some degree of specularity or "aspect sensitivity". Many such irregularities or "eddies" can coexist within the radar volume. To first order, these turbulent structures fall off in a Gaussian way, and are wider horizontally than vertically as shown in Figure 4.2. This is the most common structure alignment in the atmosphere. Here "h" corresponds to the vertical scale or distance over which the refractive index distribution reachs e^{-1} of its maximum value. Similarly, "L" corresponds to the horizontal scale of the radio scatterer. Other types of functions can be used to model refractive index variations but the equation in Figure 4.2 is very common and greatly simplifies the math.

Once a target model is established, we can predict radar backscatter using scattering theory. Another approach is to make radar measurements and from these work backwards to learn about the atmospheric medium. "Isotropic" scatter is the term generally used to name radar backscatter independent of the beam

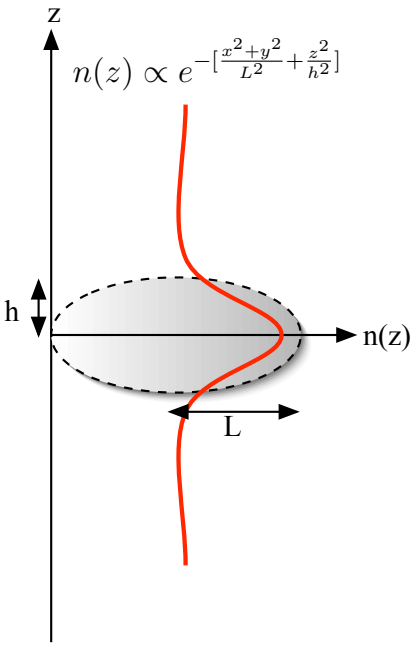

Figure 4.2: Mathematical and graphical representation for a typical radio scatterer in clear air.

direction. "Stretched or aspect sensitive" scatter refers to a medium where the power falls off in a Gaussian manner. The power dependency on the radar beam angle, θ, for an aspect sensitive scatterer is defined by [Hocking, 1987; Hocking et al., 1990] as

$$B(\theta) \propto e^{\frac{-\sin^2(\theta)}{\sin^2(\theta_s)}}, \tag{4.12}$$

where θ_s is a constant or the so-called aspect sensitivity parameter that is related to the scatterer and radar beam polar diagrams. The latter must be deconvolved such that a more accurate description for the scattering mechanism can be found. The higher the value of θ_s, the slower the backscattered power fall off is, and as a result, the more isotropic the medium is.

How is the aspect sensitive parameter measured? There are two general radar

techniques: (1) beam steering, where a single radar beam is moved around the sky and power measurements are taken for different zenith angles, and (2) spatial correlation, where multiple receiving antennas measure the ground diffraction pattern of the scattering medium. A least squares fitting technique is applied on the data to invert equation 4.12 or to find the best approximation for the θ_s parameter.

4.1.3 Edge Scatter

Radar scattering in clear air is not only due to turbulent eddies. Stratified layers of refractive index can occur in the neutral atmosphere, primarily as a result of layered regions of turbulence that evolve into regions of adiabatic lapse rate bounded by sharp gradients in the potential temperature [Werne and Fritts, 1999; Chen et al., 2001]. Electron density stratification can also produce sharp gradients of the radio refractive index. We refer to non-turbulent scatter as edge scatter or specular reflection. Fresnel scattering arises from randomly distributed specular reflectors in space. Other types of phenomena producing edge scatter include meteor trails, particle precipitation, and PMSE. Before discussing edge scatter in detail we should stress that in-situ measurements using rockets have shown evidence of turbulent and non-turbulent mechanisms occurring simultaneously at mesospheric altitudes.

Edge scattering is often explained using a simple slab geometry of radio refractive index, where the atmosphere is modeled as a series of slabs or stratified layers [Gage et al., 1981; Hocking and Vincent, 1982; Hocking and Röttger; 1983]. Figure 4.3 shows a slab geometry containing a series of layers with different refractive indexes. The reflection coefficient for radio waves impinging the n_1/n_2 boundary is given by $\rho = \frac{n_1 - n_2}{n_1 + n_2}$. In general, for steep changes of the refractive index, the radar reflection coefficient profile can be expressed as

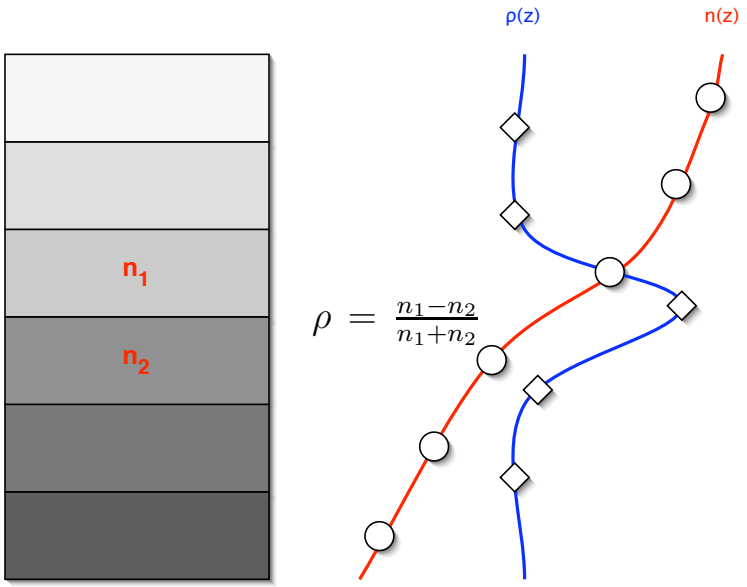

Figure 4.3: a) Slab geometry of refractive index and reflection coefficient for two mediums of different refractive indices, n_1 and n_2, b) Reflection coefficient and refractive index profiles for slab geometry shown in a). Adapted from Hocking [2002].

$$\rho(z) = \frac{\Delta n}{2} = \frac{1}{2}\frac{dn}{dz}dz. \tag{4.13}$$

Wait [1962] found the following expression for the power reflection coefficient of an electromagnetic wave approaching an infinite horizontal layer:

$$|\rho|^2 = \frac{1}{4}|\int_{-l/2}^{+l/2} \frac{dn}{dz} e^{-j2kz} dz|^2, \tag{4.14}$$

where l is the thickness of the reflecting layer. The power reflection coefficient maximizes for Fourier components with vertical scales equal to half the radar wavelength ($k = \frac{2\pi}{\lambda_R}$).

Gage et al. [1981] and Hocking and Röttger [1983] modeled "Fresnel" or edge scatter for VHF radars as random variations of the refractive index as a function of height, $n(z)$, where the atmosphere is represented as a series of slabs as shown in Figure 4.3. Gage et al. [1981] developed a model for Fresnel scattering assuming half-wavelength periodic structures of the refractive index, the spatial component of which the radar is sensitive. A layer of arbitrary thickness L centered at z_o takes the form

$$n(z) = n_0 + (\delta n)_{\lambda/2} \sin(2kz + \phi_{\lambda/2}), \tag{4.15}$$

[Gage et al., 1981], where $\delta_{\lambda/2}$ and $\phi_{\lambda/2}$ represent the amplitude and phase of the harmonic function, respectively. The above expression is valid for $z_o - L/2 < z < z_o + L/2$. Using Equation 4.14, Gage et al. [1981] found the power reflection coefficient as

$$|\rho|^2 = \pi^2 [\frac{\Delta z}{\lambda} (\delta n)_{\lambda/2}]^2. \tag{4.16}$$

This expression is valid for $L > \Delta z$ or layer depths larger than the radar range resolution or pulse width. The same authors found no dependency in range resolution for $L < \Delta z$. A revised radar equation for Fresnel scatter was proposed by Hocking and Röttger [1983] who suggested a dependency in the range resolution of Δz instead of $(\Delta z)^2$, as previously found by Gage et al. [1981], although they recognized that the pulse dependency could be more complicated for general conditions. Hocking and Röttger [1983] express received power as a function of height as

$$P_r = \frac{\alpha^2 P_t A_e^2}{4\lambda^2 z^2}[F(\lambda)\bar{M}]^2(\Delta z), \tag{4.17}$$

where $F(\lambda)$ refers to a radar "calibration constant", $\bar{M}$ is the mean refractive index gradient, and Δz is the pulse length.

Figure 4.4 shows a graphical description of edge scatter. A continuous function is used to model a single step of refractive index. The radar return or the reflected complex amplitude, $a(z)$, can be modeled as the convolution of the reflection coefficient profile, now $r(z)$, and the radar pulse, $g(z)$ (left hand plots, z-domain). After correcting for range, the reflected pulse can be approximated as

$$a(z) \propto \frac{r(z)}{z} \otimes g(z) \tag{4.18}$$

[Hocking and Röttger, 1983]. This is equivalent to the product of the spatial Fourier transforms of the reflection coefficient, $R(k)$, and the radar pulse, $G(k)$ (right hand plot, k-domain). The Fourier transform for r(z), a Gaussian function, is simply another Gaussian function but broader compared to the Fourier transform of the radar pulse, which can be approximated by two narrow Gaussians at $-2/\lambda$ and $+2/\lambda$, respectively. Since $R(k)$ is nearly constant with respect to $G(k)$ at these two points, the product $R(k)G(k)$ can be taken as $R(2/\lambda)$ scaled by the peak value

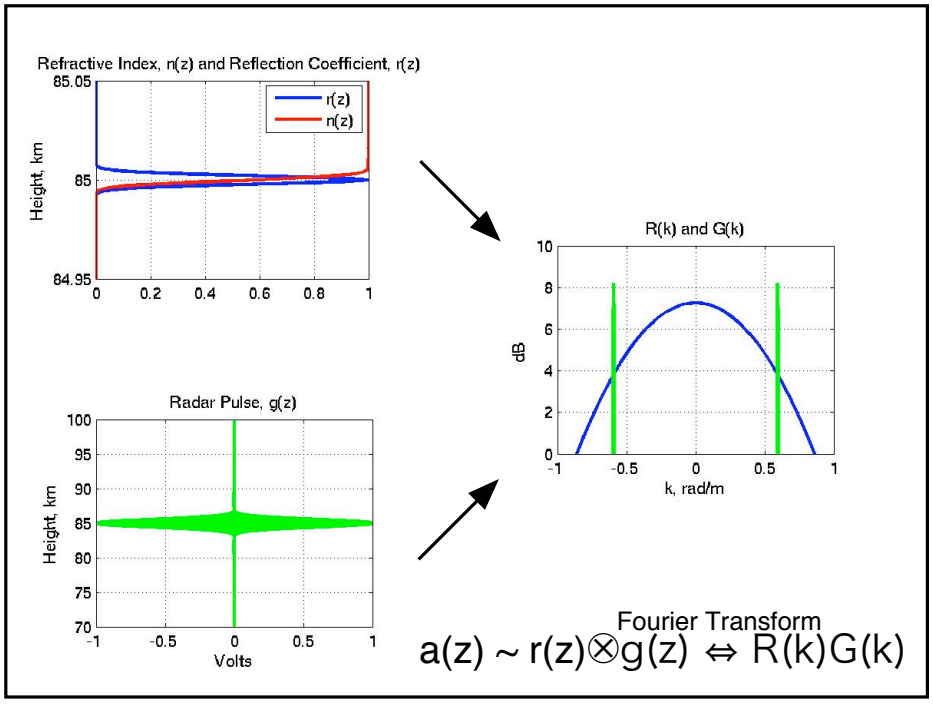

Figure 4.4: Reflected complex amplitude for a single step of refractive index. The two left panels show refractive index, reflection coefficient, and radar pulse variations in space or z-domain. The right panel shows a representation of the refractive index and radar pulse in inverse space or k-domain.

of $G(k)$, which is a constant for a fixed pulse-width. In that way, for a given range z_o (Ex. $z_o = 85$ km), $a(z)$ is found to be

$$a(z_o) \propto e^{-\pi^2 d^2 (2/\lambda)^2} = e^{-\frac{4\pi^2 d^2}{\lambda^2}} \tag{4.19}$$

[Hocking and Röttger, 1983], where d is the thickness of the irregularity. The backscattered power is proportional to the square of this approximation for the complex reflected amplitude. It can be easily shown that for $d > \lambda/2$, the amount of signal attenuation (> 80 dB) will be quite significant and will not be compensated by signal processing methods. Reasonable detection can be attained for layer depths smaller than $\lambda/2$ [Hocking, 1987].

4.2 Rocket Data Analysis

In this section we apply scattering theory to in-situ measurements of electron density. The goal is to predict radar backscatter at multiple frequencies using rocket data collected with (and without) simultaneous PMSE in the background mesospheric medium. For that purpose, two rocket soundings from Norway, DYANA-1990 and MAC/SINE-1987, were analyzed. The first one was flown in March 1990, without PMSE as expected. The second one was flown in July 1987 during a simultaneous PMSE event reported by a VHF radar. More recently, we had access to rocket data from a NASA campaign at Poker Flat in 2002; part of that data along with simultaneous MF radar data from the same location is discussed in the next chapter.

4.2.1 Non-Summer: DYANA Campaign

The DYANA campaign (DYnamics Adapted Network for the Atmosphere) was carried out from January through March of 1990 in the European northern hemisphere [Offerman, 1994; Thrane et al., 1993]. The rocket sounding analyzed here took place on March 11, 1990, 2042 UT, at the Andoya rocket range in Norway. Figure 4.5a shows electron density versus altitude data. Figure 4.5c shows a power spectral density estimate performed on a 1 km segment of de-trended electron density centered at 84 km. An on-site magnetometer and a riometer gave measurements of 200 nT and 0.2 dB absorption, respectively, during the time of the rocket flight [personal communication with T. Blix, 2002], indicating strong geomagnetic activity and a relatively low absorption in the ionosphere.

4.2.2 Summer: MAC/SINE Campaign

The MAC/SINE campaign (Middle Atmosphere Cooperation/Summer In Northern Europe) took place in Norway during the summer of 1987 [Inhester et al., 1990]. Figure 4.5b shows electron density measured during the up-leg portion of one flight (July 14, 1987; 0929 UT). Data from the Sousy/53.5 MHz radar collected simultaneously is shown in Figure 4.5b. Notice the strong bite-out of electron density occurring between 85 and 87 km. The VHF radar recorded the strongest echoes (attributed to PMSE) near the altitude of an upper ledge of electron density. Similar to the non-summer display, Figure 4.5d shows a Fourier analysis for electron density fluctuations on a 1 km data segment centered at 84 km. Below we discuss characteristics and major differences between both rocket flights.

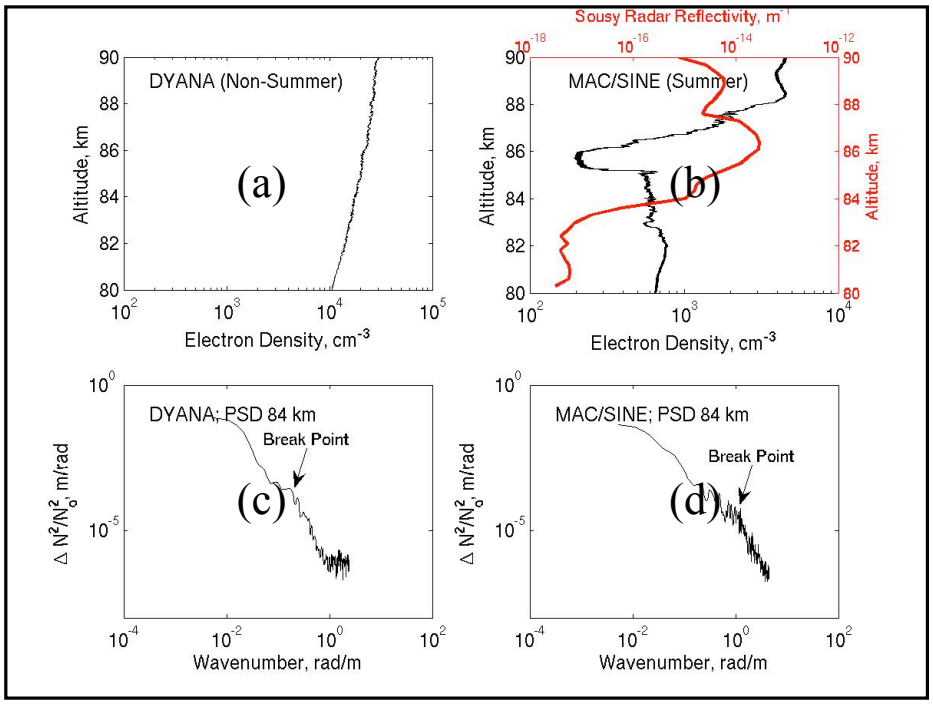

Figure 4.5: Rocket flights representing (a) non-summer and (b) summer mesospheric conditions. Fourier analysis performed on non-summer and summer electron density data, (c) and (d), respectively. Over-plotted in (b) is shown radar reflectivity data collected simultaneously with the Sousy/53.5 MHz radar.

4.2.3 Differences between the Non-summer and Summer Rocket Measurements

The differences between the summer and winter profiles and spectra can be summarized as follows:

1. The most striking difference is the deep summer bite-out which has been explained as an attachment of electrons to ice covered dust particles [Reid, 1990].

2. In addition to the bite-out in the summer data, a low level of fluctuations exists, which are similar to the entire profile in the non-summer conditions, albeit about a factor of three higher in $\delta n/n$ variations.

3. The non-summer spectrum shows a break in the spectral form from a shallow slope to a steep one at about 0.2 rad/m (see arrows). A similar break occurs in the summer at about 1 rad/m. The former corresponds to a scale of 30 m which is in good agreement with the predictions based on the Kolmogorov micro-scale in atmospheric turbulence [Hocking, 1987], while the latter requires a significant extension of the spectrum to smaller scales associated with a high Schmidt Number [Batchelor, 1959; Kelley et al., 1988].

Due to the steepness of the slopes at high k, the most important factor leading to the strong VHF echoes is the Schmidt Number effect (the ratio of the viscosity coefficient to the electron diffusion coefficient, $S_c = \frac{\nu}{D}$), which is due to massive charged particles [Cho and Kelley, 1993; Hill et al., 1999] and which leads to structures at their small Bragg scales. The Bragg scales of our MF/2.43 MHz (λ_B = 61.7 m, k = 0.1 rad/m) and HF/4.9 MHz (λ_B = 30.6 m, k = 0.2 rad/m)

radars are much closer to the classic atmospheric inner scale for non-polar summer conditions. Note that the fluctuation levels are about the same in summer and winter at these k values.

4.3 Wavelet Decomposition and Edge Reconstruction of Electron Density

The layered nature of the rocket and radar data sets suggests that a Fourier analysis may not be appropriate to extract information on electron density fluctuations as a function of scale size in all cases. Indeed, the Wavelet transform has been used for the analysis of in-situ data in mesospheric [Alcala et al., 2001a,b] and lower atmospheric studies [Chen et al., 2001]. Figures 4.6 and 4.7 show two examples of wavelet analysis performed on non-summer and summer rocket measurements of electron density. The Canny edge detector [Canny, 1986], equivalent to the first derivative of a Gaussian function, is used to localize edges of electron density in both physical space (i.e., rocket altitude) and scale size of the irregularity.

A wavelet scalogram provides information on the signal energy as a function of space and scale size. This property makes it possible to identify edges or gradients existing in a data sequence. An edge is defined as a signal variation that is localized in space, as opposed to random phenomena, like turbulence, that are uniformly spread out over space and/or time, and has structure at multiple scale sizes. Traditional Fourier analysis provides frequency information for the complete duration of the analyzed signal and doesn't distinguish localized features in space and/or time. Wavelets overcome this limitation by separating edges from turbulent components in the data, and lastly calculate radar backscatter for both types

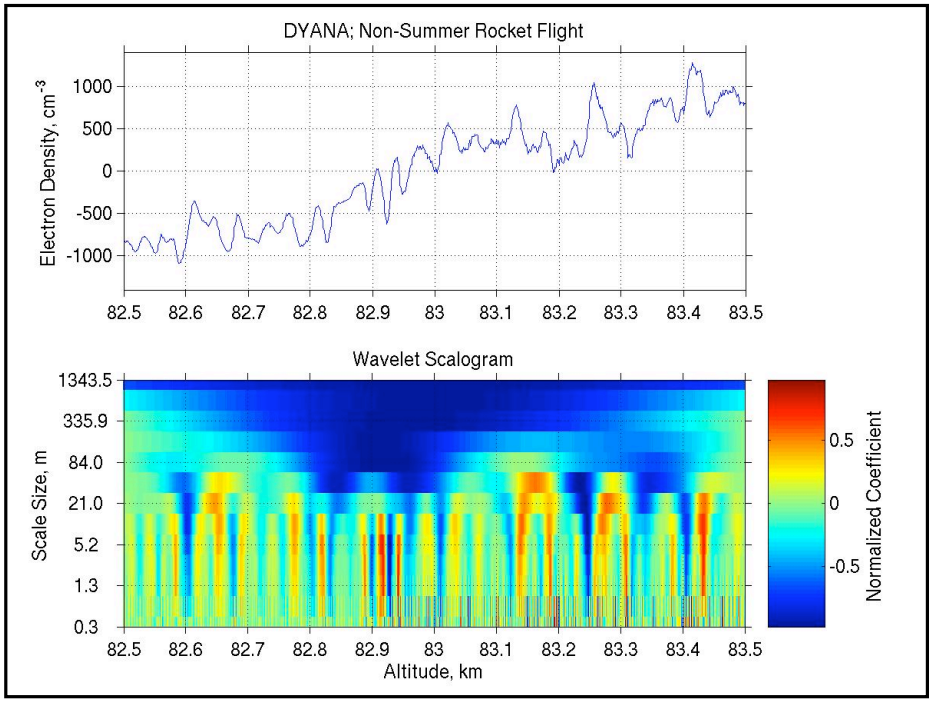

Figure 4.6: Wavelet analysis applied to a non-summer rocket data segment. The top panel shows de-trended electron density versus altitude. The bottom panel shows a Wavelet scalogram obtained for the data segment in the upper panel.

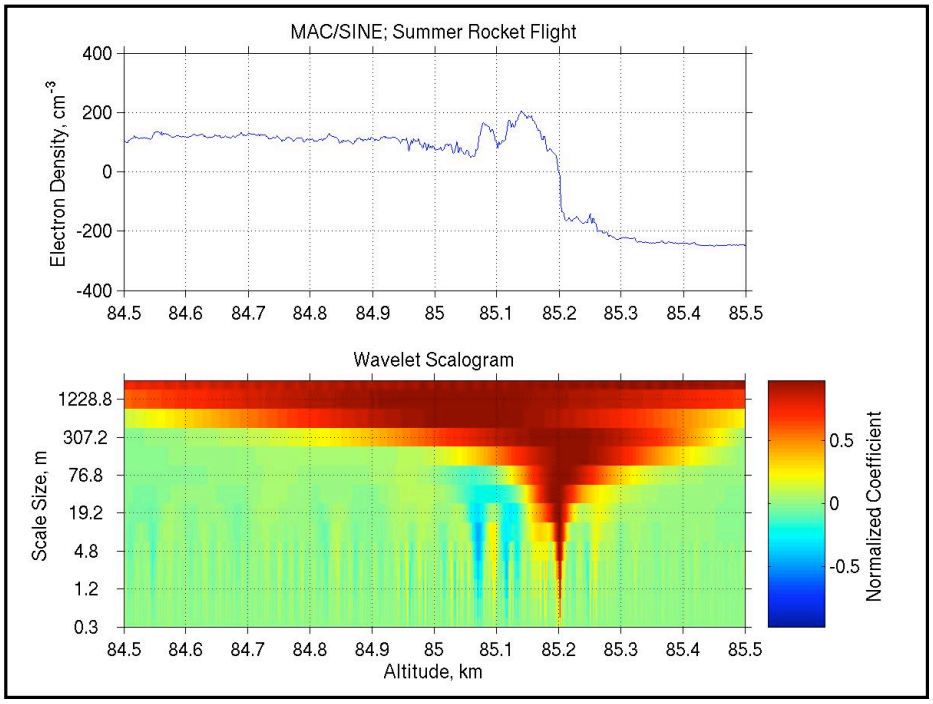

Figure 4.7: Wavelet analysis applied to a summer rocket data segment using the format of Figure 4.6.

of phenomena individually.

The two wavelet scalograms (the colored bottom panels in Figures 4.6 and 4.7) show evidence of multiple edges in the two rocket data segments. Specifically, in the summer data, a dominant edge is localized at approximately 85.2 km. Notice how at this altitude the scalogram shows structure from larger scales connecting down to smaller scales, a necessary condition for edge occurrence as explained previously. Red colors indicate negative or decreasing edges. Similarly, blue colors indicate positive or increasing edges. The scalogram information was normalized, with respect to its maxima at each scale size, to facilitate the data visualization.

After identifying edges in space, using an edge tracking algorithm based on Alcala et al. [2001a], the edge portion of the electron density profile can be reconstructed using the appropriate wavelet coefficients and Canny basis functions as

$$N_e(\xi) = \sum_{b=1}^{N} \sum_{i=1}^{M} A_i \psi_{i,b}(\xi), \tag{4.20}$$

where A_i represents the wavelet coefficients for the basis function $\psi_{i,b}$. Index i represents dilation or wavelet scale size, and index b spans space, or altitude in our case. The Canny basis function is given by

$$\psi_{i,b} = -\pi^{-1/4} \sqrt{2^{(1-i)}} \left(\frac{\xi - \xi_b}{L_i}\right) e^{-(\xi-\xi_b)^2/2L_i^2}, \tag{4.21}$$

where ξ_b is the offset of the wavelet basis function from the center of the range window, $L_i = 2^i \Delta x$ is the wavelet scale size, and Δx is the instrument sampling distance.

The backscattered electric field or reflection coefficient, as a function of radar range gate, for an edge or a set of edges has been derived by Doviak and Zrnic

[1984] as

$$\rho(r_o) = -j(\frac{2\pi r_e}{k_o}) \int_{-\infty}^{+\infty} N_e(\xi) e^{-(\frac{\xi^2}{4\sigma_r^2})} e^{-2jk_o\xi} d\xi. \tag{4.22}$$

Here r_e is the classical electron radius, k_o is the radar wavenumber, and σ_r is the second central moment of the radar range weighting function. We can express the radar reflection coefficient, equatio 4.22, in terms of the reconstructed electron density profile obtained with the Canny edge detector, shown in equations 4.20 and 4.21, as

$$\rho_b = -\pi^{-1/4}(8\pi r_e) \sum_{i=1}^{M} \frac{A_i L_i^2}{\sqrt{2^i}} e^{-2(k_o L_i)^2}. \tag{4.23}$$

The above expression is obtained after neglecting a phase term of the form e^{-2jx} and range weighting effects due to radar parameters and the fact that only certain scale sizes contribute to edge scattering [Hocking, 1987]. Please refer to Appendix A.4 for a detailed derivation of Equation 4.23.

Using equation 4.23, and assuming random spacing, the reflection coefficients from each edge can be squared and summed to obtain the scattered power for a given radar range gate,

$$P_r(r_o) \propto \sum_{b=1}^{N} |\rho_b|^2. \tag{4.24}$$

Radar system parameters determine the proportionality constant. We can then compare our estimate for edge scatter with turbulent volume-filling scatter calculations and determine the relative contributions for both types of mechanisms. Given the limitation of the sounding rocket technique, where only a one dimensional view of the medium can be obtained, i.e., the z-axis, we are forced to assume that the medium is uniform along the x and y axes. Better rocket measurements, e.g., multiple spaced samples at each altitude, are necessary to overcome the above limitation and obtain more exact estimates of the scattering components affecting the radar sampled volume.

4.4 Radar Reflectivity Calculations

To compare estimates of radio scatter at different frequencies we use reflectivity values since they are independent of the radar parameters, and conclusions about the medium can be made in more absolute terms. In the next sub-sections, we describe the appropriate expressions for radar reflectivity for the scattering mechanisms of interest here.

4.4.1 Turbulent Scatter

Royrvik and Smith [1984] derived radar volume reflectivity for turbulent scatter in terms of the rocket irregularity power spectra. They found

$$\eta_{turb} = -n(\frac{\pi}{8})k^2 \frac{f_p^4}{4f^4} S_n(k), \tag{4.25}$$

where n is the local spectral index for a given wavenumber k, f_p is the plasma frequency, f is the radar probing frequency, and $S_n(k) = (\frac{\Delta N}{N_o})^2$ is the one-dimensional power spectrum measured by the rocket in meters per radian.

4.4.2 Edge Scatter

To derive an expression for effective radar reflectivity produced by edges of refractive index, or electron density, we begin from the well known radar equation for a point or solid target

$$P_r(r_o) = \frac{\alpha^2 P_t A_e^2 \sigma}{4\pi\lambda^2 r_o^4}, \tag{4.26}$$

which was described extensively in section 4.1. Here P_t is transmitted power, α is a one-way efficiency factor, A_e is the effective area of the antenna, σ is the target radar cross section, and λ is the radar wavelength. Gage et al. [1981] relate

the squared magnitude of the reflection coefficient produced by an irregularity of length L_i to the radar received power with the following equation,

$$P_r(r_o) = \frac{\alpha^2 P_t A_e^2}{4\lambda^2 r_o^2} |\rho_i(\xi_o)|^2. \tag{4.27}$$

Here the basic assumption is that the irregularity horizontal size is at least one Fresnel zone

$$R_i = \sqrt{\frac{\lambda r_o}{2}}. \tag{4.28}$$

By equating (4.26) and (4.27), and knowing that $\eta = \frac{\sigma}{V}$, the following expression for effective edge scatter or edge reflectivity, in terms of the radar reflection coefficient, is derived [Alcala et al., 2001b]

$$\eta_{edge} = \frac{4}{\theta^2 \Delta r} |\rho|^2. \tag{4.29}$$

The two parameters in the denominator, beam width, θ, and range resolution, Δr, are due to the volume dependency for reflectivity and are determined by the radar system. For our calculations we have assumed $\Delta r = 1$ km and $\theta = 3, 20, 40$ degrees for the three radar frequencies of interest: 53.5, 5.0, and 2.5 MHz, respectively. MF radars, as expected for the lower frequencies and similar antenna sizes, have bigger antenna beam widths than HF and VHF radars.

Figure 4.8 shows results for predicted radar scattering for the two analyzed rocket flights and three different altitudes (83, 84, and 85 km). The dashed curve denotes the predicted radar reflectivity for isotropic turbulent scatter. The low k portion of the data sets has been matched to the expected reflectivity from the turbulence spectrum model of Driscoll and Kennedy [1985] in the range of 0.04 rad/m $\leq k \leq$ 0.80 rad/m, assuming a Schmidt number of $S_c = 1$ for non-summer conditions and $S_c = 100$ for summer. This is plotted as the solid black curve. The edge scatter is shown by the "+" markers at two wavenumbers for non-summer

and three wavenumbers for the summer case. In the next section we summarize the results for both seasons. Complete wavelet analyses and similar reflectivity calculations are shown in Appendices A.5 and A.6 for higher and lower altitudes.

4.5 Summary

The radar reflectivity calculations derived from the MAC/SINE rocket campaign (summer season, right panels of Figure 4.8) indicate that at PMSE and non-PMSE altitudes, the edge scattering mechanism should dominate turbulent scatter at the analyzed MF/HF/VHF radar frequencies (2.5, 5.0, and 53.5 MHz, respectively). For non-summer conditions (DYANA rocket campaign, left panels of Figure 4.8), both types of scattering components (edges and turbulence) are expected to produce more or less even contributions, although slightly biased toward edge scatter. These calculations suggest that MF and HF radars should be suitable for observing PMSE or any other type of layered phenomena in the upper mesosphere, assuming other ionospheric conditions do not severely affect the radar signal. These results are revisited in the next chapter but in the context of mesospheric dust and MF radio scatter.

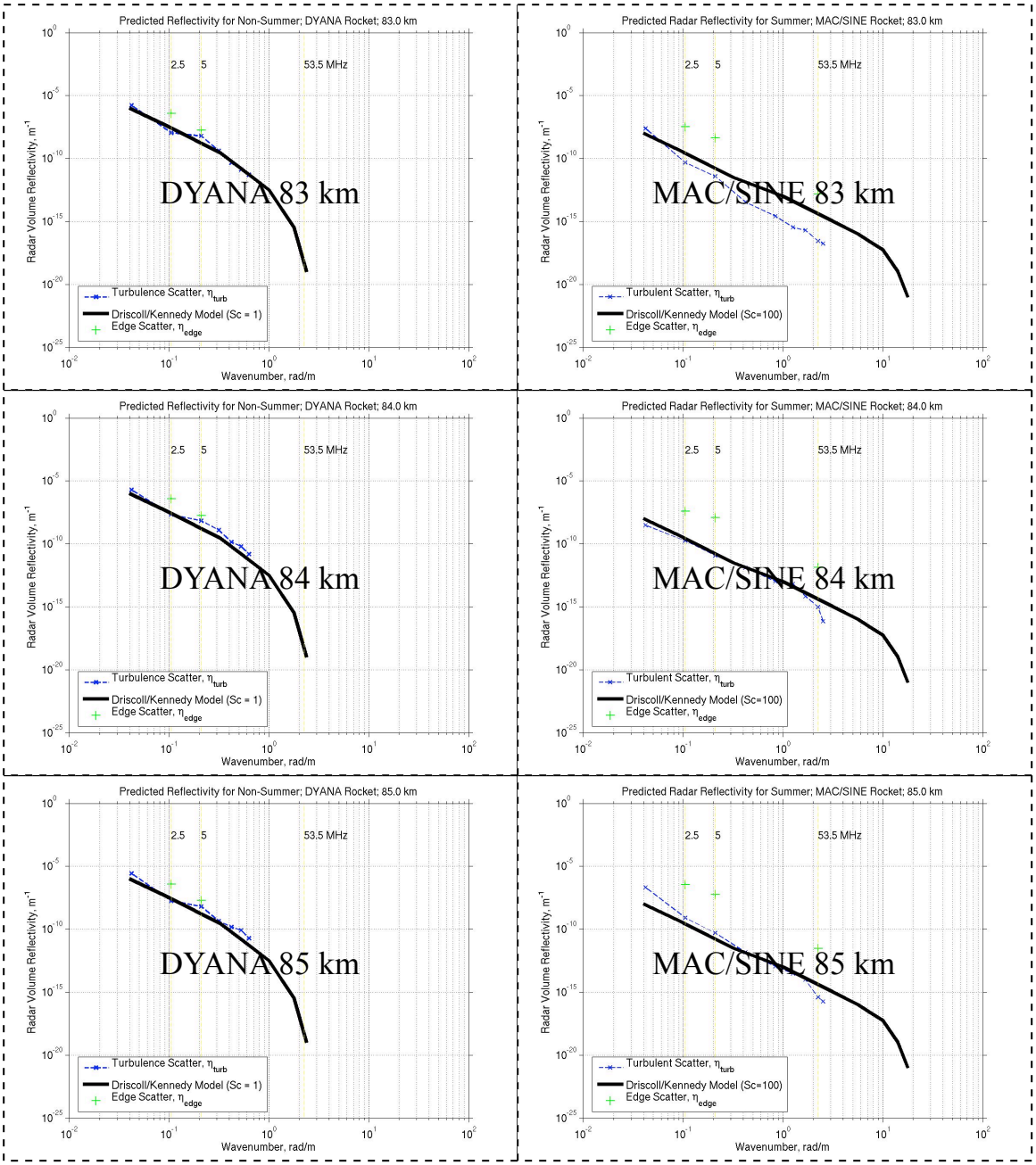

Figure 4.8: Radar reflectivity, η_{turb} and η_{edge}, versus wavenumber, k, for (a) non-summer and (b) summer, and three different altitudes: 83, 84, and 85 km. The Driscoll and Kennedy model for turbulent reflectivity is superimposed for $S_c = 1$ on the left and $S_c = 100$ on the right.

Chapter 5

On a Possible Relationship Between Mesospheric Dust and Medium Frequency (MF) Radio Scatter

Dust particles of meteoric origin are known to exist in the mesosphere where they can scavenge electrons. In our radar studies at high latitudes, we have found enhancements in MF radar signal at altitudes near and lower than that expected for PMSE. These structures occur equally during summer and non-summer periods, although they are less noticeable in summer due to the presence of PMSE. Could mesospheric dust particles be related to those echoes? In this chapter we present collocated radar and rocket measurements exploring this idea.

5.1 Radio Scattering at Medium Frequencies

Sharp transitions in refractive index and/or electron density produce partial reflections in the lower ionosphere, the primary radar scattering mechanism in the MF band (1-3 MHz). At up to about 100 km, these spatial irregularities in the refractive index are generated by neutral air turbulence most of the time. Extragalactic objects entering the atmosphere can similarly produce this type of fluctuations during their lifetime, e.g., ionization by meteor trails or smoke and dust particles recombined from ablated atoms and oxidized material at mesospheric altitudes [Rosinski and Snow, 1961; Hunten et al., 1980]. Radar waves are scattered or reflected by meteor trails, depending on whether the electron density in the trail

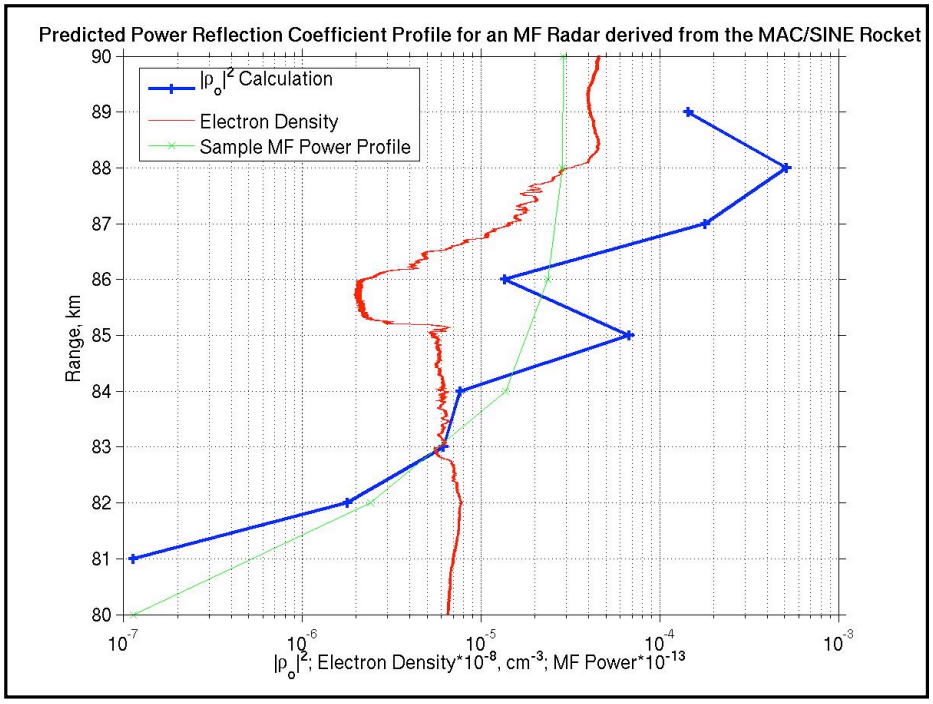

Figure 5.1: Predicted power reflection coefficient profile for an MF/2.5 MHz radar derived from in-situ data collected during summer (MAC/SINE rocket). A sample MF power profile measured at Poker Flat (June 18, 2002, 19-21 UT) is over-plotted for comparison purposes.

is underdense (the plasma frequency is smaller than the radar frequency) or overdense (the plasma frequency is larger than the radar frequency), respectively. In addition, a new long duration meteor scatter mechanism has been found that is related to charged dust in an underdense trail [Kelley, 2004].

The partial reflection echoes are very weak in the mesosphere. Typical values for power reflection coefficients in the upper mesosphere region range between 10^{-10} and 10^{-6} [Hargreaves, 1992]. Figure 5.1 shows the predicted power reflection profile, $|\rho_o|^2$ versus range, for an MF/2.5 MHz radar derived from rocket measurements of electron density collected during a summer day in Norway (MAC/SINE 1987). Please refer to Appendix A.4 for a description of the $|\rho_o|^2$ calculation. The enhancement at 85 km is concurrent with a PMSE event detected by a 50 MHz radar (see Figure 4.5b). Below 85 km, the $|\rho_o|^2$ values are in good agreement with what would be expected for the mesosphere. The presence of ice and/or PMSE certainly produces the enhancement at 85 km. At above 85 km, the monotonic increase for $|\rho_o|^2$ is presumably due to the higher contents of electron density. A sample MF power profile from the Poker Flat MF radar is over-plotted for comparison purposes. Notice the similarities between the $|\rho_o|^2$ calculation and the MF radar measurement. Unfortunately, we did not have access to rocket data from lower altitudes but the aim was to estimate the effect of gradients in electron density in the production of partial reflections. Dust particles at altitudes closer to PMSE or below them may induce similar enhancements in reflection coefficient as we will see in the next sections.

5.2 Mesospheric Dust Layers

Thousands of meteors enter the near-space region of the Earth throughout the year. The majority of these extra-galactic materials vaporize due to friction and then oxidize and re-condense at upper mesospheric altitudes, finally producing the so-called dust layer. Ambient plasma and sunlight can charge/discharge dust particles by means of attachment/detachment processes.

Heavy charged species may be crucial for producing Noctilucent Clouds (NLC), that are associated to PMSE, which can be observed remotely using lidars. To date radio techniques have not been used to observe these nanometer sized particles but depletions in electrons produced by a structured charged dust layer could generate spatial structure at MF/HF/VHF radar frequencies.

Only recently have in-situ measurements of dust content been possible using rocket-borne instruments [Gelinas et al., 2005]. This type of information is important to support theoretical and modeling work on the dynamical and chemical processes occurring in the mesosphere.

5.3 Radar and Rocket Observations of Mesospheric Dust

A NASA rocket campaign was carried out in Poker Flat, Alaska during the winter of 2002 [Gelinas et al., 2005]. The goal was to study charged dust particles in the mesosphere. A set of four dust density profiles, in units of cm^{-3}, are shown in Figure 5.2. Superimposed is the corresponding MF radar normalized backscattered power for the nearest times. The first flight (March 07, 2002) was intended for control purposes; the second set of three flights (March 15, 2002) took place during a sudden atom layer (SAL) event detected by a lidar system at Poker Flat. The

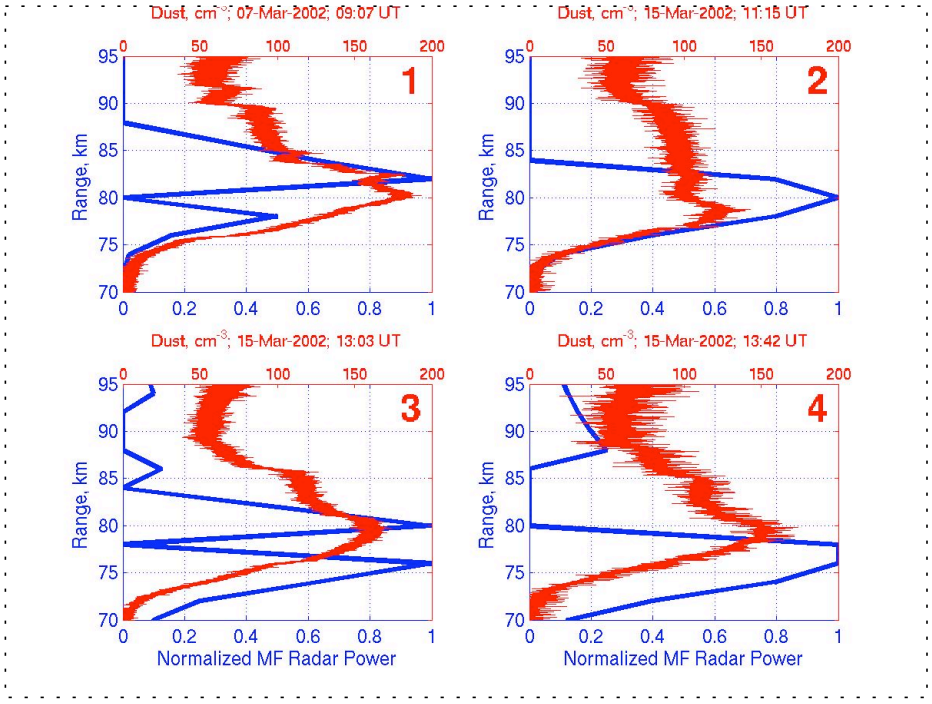

Figure 5.2: Radar and rocket concurrent observations of MF power and charged dust density, respectively, over Poker Flat, Alaska (NASA Rocket Campaign, March 2002).

four rockets were flown during nighttime and no auroral activity was reported during the two days.

All the rocket flights showed the presence of negatively charged dust layers with densities up to nearly 200 cm^{-3}. Dust particles occurred between 78 and 90 km and strong correlations were found with lidar detections of sodium and iron layers [Gelinas et al., 2005]. The dust profiles have been inverted in sign to facilitate the comparisons with radar data.

A global view of MF radar power data collected before and after the rocket flights is presented in Figure 5.3. The dust peak profiles have been over-plotted at their respective flight times. Although the profile to profile comparisons in Figure 5.2 show slight differences in altitude between the radar enhancements and dust peaks, the radar power histories shown in Figure 5.3 indicate that, in general, the mesospheric conditions recorded by the rockets were consistent with some type of radiowave scattering effect between 75 and 85 km. Three of the four rocket flights are coincident with temporal and spatial patches of MF radar power, and the dust maxima in the last flight, rocket number 4, occurred just minutes before the radar detected a new enhancement in backscattered power. Differences in sensor coverage between the radar and the rockets could explain minor discrepancies in time or space.

5.4 The Dust Effect at MF/HF/VHF

We now turn to inter-frequency and inter-seasonal comparisons of mesospheric radar profiles to check whether some additional insights can be obtained on the presence of dust layers. For that purpose, we show typical MF/HF/VHF scattering profiles, for summer and non-summer periods, in Figure 5.4. The top panel, Figure

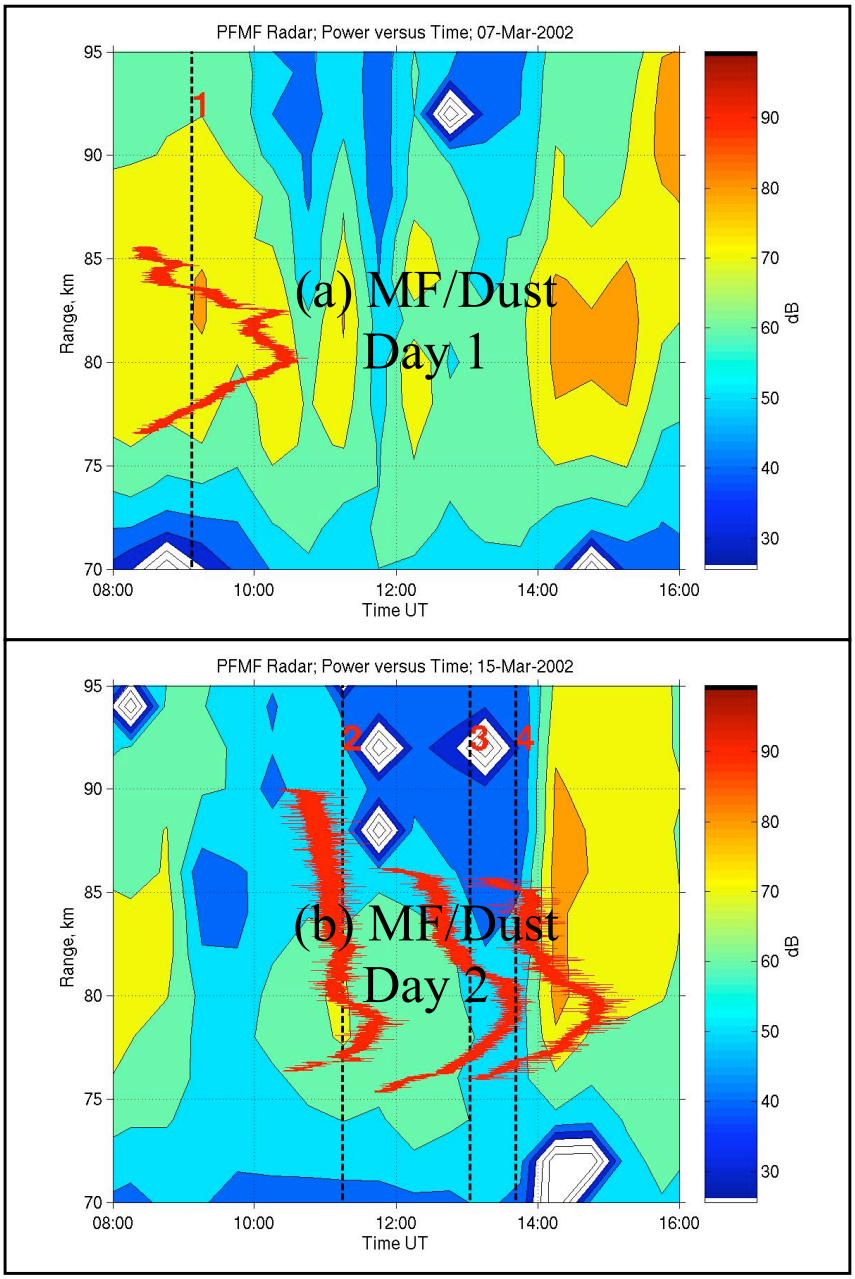

Figure 5.3: Dust peak profiles and MF power/radar history for (a) March 07, 2002; 08-16 UT, and (b) March 15, 2002, 08-16 UT, at Poker Flat, Alaska.

5.4a, shows MF power profiles for January 13, 2002/non-summer and July 13, 2002/summer, respectively. Similarly, Figure 5.4b shows HF signal to noise profiles for March 25, 2004/non-summer and July 03, 2003/summer, respectively. For completeness, VHF statistics from the historical Poker Flat database, 1979-1980, are shown in Figure 5.4(c).

Both MF profiles display a clear maxima in scattered radar signal for each season. We will concentrate on the echo characteristics below 90 km. The summer data (July 13, 2002) show the typical 86 km bump associated with PMSE, which we had previously predicted using MAC/SINE rocket data (Figure 5.1). A second maxima, but less evident, shows up around 74 km. The MF non-summer data (January 13, 2002) show no indication of structures between 80 and 90 km but the same profile shows a remarkably strong signal maxima at 78 km. We think that this bump could be an indicator of mesospheric dust due to its similarity to the radar results shown in the previous section on the radar rocket collocated observations at Poker Flat. The lack of in-situ data prevents further conclusions. Long-term analyses of MF radar data, previously shown in Chapter 3, suggest that the two MF profiles presented in Figure 5.4(a) are good representations of summer and non-summer radar measurements of the mesosphere.

Figure 5.4(b) shows HF radar summer and non-summer, 1-hour averaged SNR profiles. Our HF databases for the summer season are quite extensive so we are very confident that the July 3rd, 2003 radar profile is a good representation of average conditions in the polar summer mesosphere. Notice the PMSE peak echo ($\sim$25 dB) at 86 km. Weaker structures can be seen at lower altitudes but the SNRs are too weak to establish their origin. The non-summer data show no indication of PMSE, as expected, although some very weak structures are identified between 85

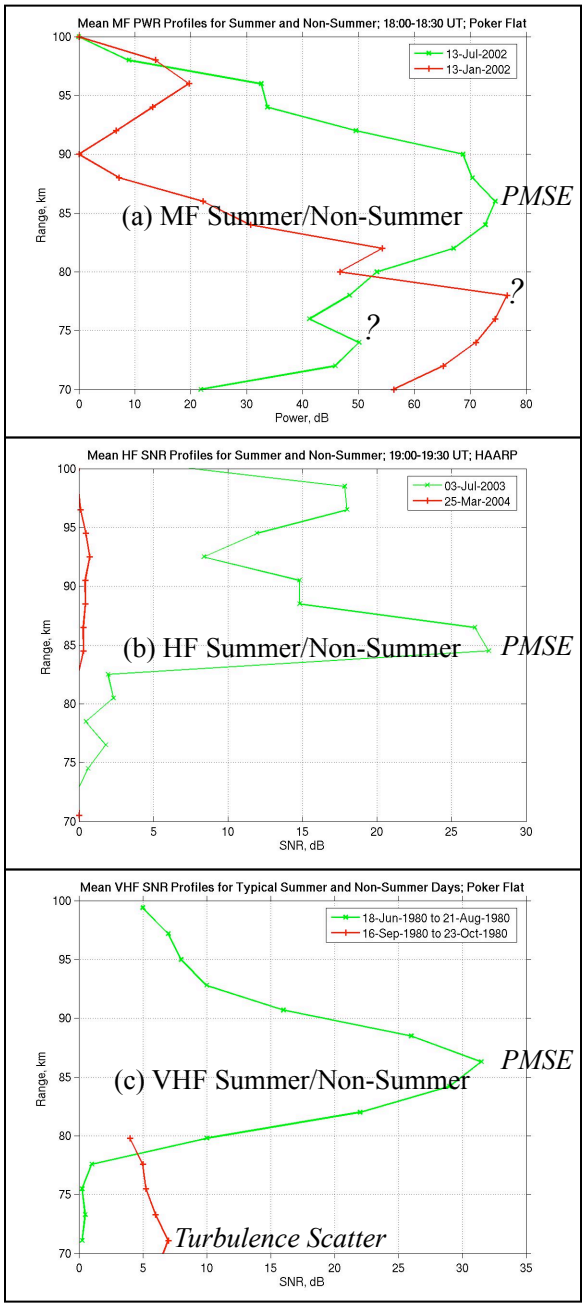

Figure 5.4: Typical summer and non-summer backscattering profiles for the (a) Poker Flat MF/2.43 MHz, (b) HAARP HF/4.9 MHz, and (c) Poker Flat VHF/50 MHz radars. The VHF results were adapted from Ecklund and Balsley [1981].

and 90 km. We conducted fewer non-summer HF observations but found that all of them had a faint scattering region in common, with a few dBs of SNR, always occurring between 80 and 90 km.

Figure 5.4(c) shows VHF summer and non-summer average SNR profiles. The summer average profile shows the well defined PMSE region, which extends from 80 to about 93 km. The winter average profile is about two orders of magnitude weaker than the summer profile and approximately 10 km lower in altitude. The VHF non-summer profile shows some similarities with the MF results from 5.4(a). The mean MF winter profile shows a peak signal at 76 km. At VHF, the peak altitude is approximately 72 km. The VHF statistics should be given more weight since they consist of a full month of analyzed data. The low value of the winter SNR peak leads us to conclude that dust might not be the primary contributor to the VHF scattering mechanism. Balsley et al. [1983] explained the VHF winter mesospheric echoes as irregularities in electron density produced by gravity wave breaking induced turbulence.

How do we explain these multi-frequency profiles and the apparent lack of HF "dust" echoes? PMSE occurrence at MF/HF/VHF is not questioned but the HF/VHF results are more reliable for its identification, as we stated in Chapters 3 and 4. On the dust side, we can say that the MF radar seems to be more sensitive to dust particles. A competition with PMSE/ice could "hide" the MF dust echoes during the summer season but some indication of radar structures at altitudes below 80 km remain between May and August. HF PMSE echoes could produce the same "hiding" effect in dust layers. The dust could be simply mixed with PMSE/ice or could provide the seeds for the ice crystals associated with PMSE during summer. Some of the HF summer results presented in Chapter 3 show

sporadic echoes at altitudes below those expected for PMSE, i.e., below 80 km, which could be attributed to mesospheric dust. Their non-occurrence at HF during winter looks suspicious. More winter observations would be necessary to confirm those results. Technical difficulties at the HAARP facility delayed our planned winter set of observations from mid-February to mid-March of 2004. The final set of observations ended up being 5 days and 2 hours per day during March 2004. In that regard, the MF radar database from Poker Flat, being continuous, can be used to establish more robust conclusions on seasonal trends of either PMSE/ice and possibly dust occurrence in the mesosphere.

5.5 A Possible Explanation for the Dust Radar Mechanism

One possible explanation for the multi-frequency characteristics of mesospheric dust is related to the scattering model based on the turbulence model of Driscoll and Kennedy [1985]. Figure 5.5 shows this model for predicted radar volume reflectivity as a function of wavenumber and two Schmidt numbers: $S_c = 1$ and $S_c = 100$. On the assumption of pure turbulent scatter, from irregularities in electron density driven completely by neutral air, and any S_c, the predicted radar volume reflectivity for an MF/2.5 MHz radar would be approximately 2 orders higher in magnitude than that expected for an HF radar operating at the lower HF band ($\sim$5 MHz). The fact that a low Schmidt number can trigger radar echoes within low frequency bands, e.g., MF or HF, is important since a decrease in electron diffusivity is not a requirement for turbulent scatter to occur. The opposite occurs at higher frequencies and that is why higher Schmidt numbers are necessary to explain VHF PMSE, e.g., 53.5 MHz. Meteor trails with moderate levels in electron density and diffusion could scatter radio waves more efficiently

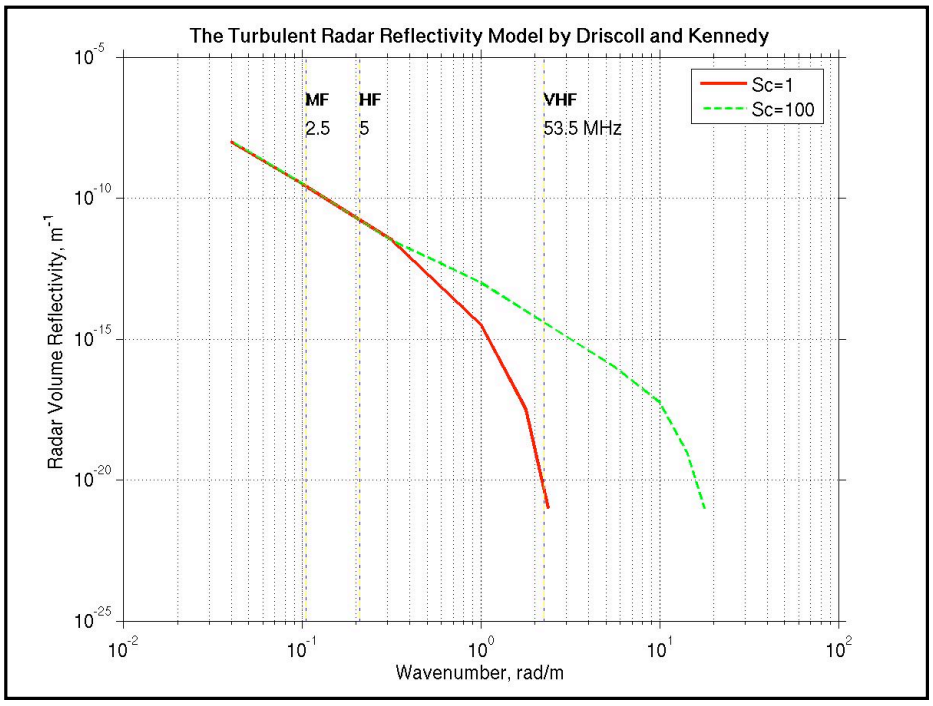

Figure 5.5: Scattering model for turbulence fluctuations as a function of wavenumber or radar frequency. Two Schmidt numbers are displayed: $S_c = 1$ and $S_c = 100$. Adapted from Driscoll and Kennedy [1985].

at MF than at HF/VHF according to the reflectivity curves shown in Figure 5.5. Along those lines, dust particles should also have a very good chance to be detected with an HF radar and that is why we question the lack of "dust" type of echoes in the HF profiles (shown in Section 5.4). Hocking [2003] has suggested a new type of wave called a dust diffusive wave analogous to viscosity waves thought to occur in the lower atmosphere. Perhaps these waves have characteristic scales that include MF but not HF wavelengths.

5.6 Summary

In this chapter we presented strong evidence that mesospheric dust induces radio scatter at MF frequencies. One possible explanation for the dust radar mechanism at MF frequencies is given in terms of the Schmidt number for a turbulent medium. A decrease in electron diffusivity, or equivalently a high Schmidt number, is not a necessary requirement for the generation of radar echoes at scale sizes relevant to MF frequencies. Dust particles with low charge numbers could scatter radio waves more efficiently at MF than at HF/VHF frequencies. Four rocket flights with measurements of mesospheric dust content and simultaneous MF radar measurements from Poker Flat, Alaska, were analyzed. Although many similarities were found between both experimental techniques, more rocket/radar observations are necessary to solidly understand the geophysical mechanisms producing MF radar scattering in the mesosphere. The occurrence of mesospheric dust, and similarly PMSE, offers a new frontier to advance the understanding of the dynamical and chemical processes occurring at those altitudes. Dust particles, acting as natural atmospheric tracers, could be monitored using ground based radars. By following the formation and evolution of dust particles, the radar technique could be employed to answer many questions about physical processes in the mesosphere.

Chapter 6

Discussion

In this chapter we look back and try to interpret the results presented in this thesis. First, we give an overview of the major findings regarding the multi-frequency radar observations. Then, we discuss the different scattering mechanisms and our attempts to quantify their relative contributions to polar summer and polar non-summer mesospheric phenomena using rocket measurements. The occurrence of dust layers in the mesosphere is re-visited. Finally, implications of our work for climate change and mesospheric studies are discussed.

6.1 Multi-Frequency Radar Studies of Icy/Dusty Plasmas

The comparisons between HF and VHF scatter verify for the first time that narrow beam HF radars can be used to detect PMSE or charged ice particles in a plasma environment. In addition we have presented, we believe, the first definitive evidence that MF radars can detect PMSE. Previously, Huaman [1998] had found small localized enhancements in mesospheric backscattered signals using MF radars at Mawson and McMurdo, Antarctica, but concurrent data were not available to validate the radar echoes firmly as PMSE. Here the correlation between MF and HF PMSE is clear, as is the correlation of events observed at the higher frequencies of HF and VHF (Figures 3.4 to 3.22, multi-frequency PMSE case studies). The analysis of two years of continuous MF radar data collected at Poker Flat, Alaska, clearly shows the presence of highly structured MF echoes following the seasonal variations of VHF scatter at polar latitudes (Figure 3.9, long-term presence of MF/VHF mesospheric radar echoes). Radar and rocket concurrent measurements

over Poker Flat suggest that MF radars have the potential to detect dust deposited in the mesosphere (Figures 5.2 and 5.3, radar/rocket comparisons). No indication of dust presence is reported consistently from separate radar data at higher frequencies although some summer HF soundings from the HAARP facility suggest the presence of that phenomenon below PMSE altitudes.

6.2 Scattering Estimation

Two major types of scattering have been proposed for mesospheric heights: edges or partial reflections and turbulent scatter. We have attempted to separate these effects using wavelets that are ideal for locating edges in space. This is a generalization of the work of Hocking [1987] who fit a rocket measured structure to a single Canny wavelet. Following Alcala et al. [2001a,b] we applied the technique to non-polar summer rocket data as well as to the polar summer case. For the non-summer case we found that the edge scatter estimates are higher than the expected turbulent scatter contribution for typical MF radar systems (Figure 4.8, predicted radar reflectivity versus wavenumber). This result is deceiving since it assumes that the horizontal scale of the scattering volume exceeds the Fresnel zone, which is 2,258 m at 2.5 MHz and 85 km.

Aspect sensitivity measurements in the mesosphere indicate a ratio of horizontal to vertical scale (L/h) of about 4. For a single scatterer with L greater than one Fresnel zone the received power scales as $P_{r1} \sim (h/L)^4$ [Balsley and Gage, 1981]. For multiple radio scatterers, as in the case here, the radar can detect scatterers within an angle $\theta_{eff} = 2\tan^{-1}(h/L)$, that contains $N = (\frac{r \times 2\tan^{-1}(h/L)}{L})^2$ scatterers across the horizontal extent of the region, which scatters effectively. We illustrate the geometry and mathematical relationships applicable for a volume consisting

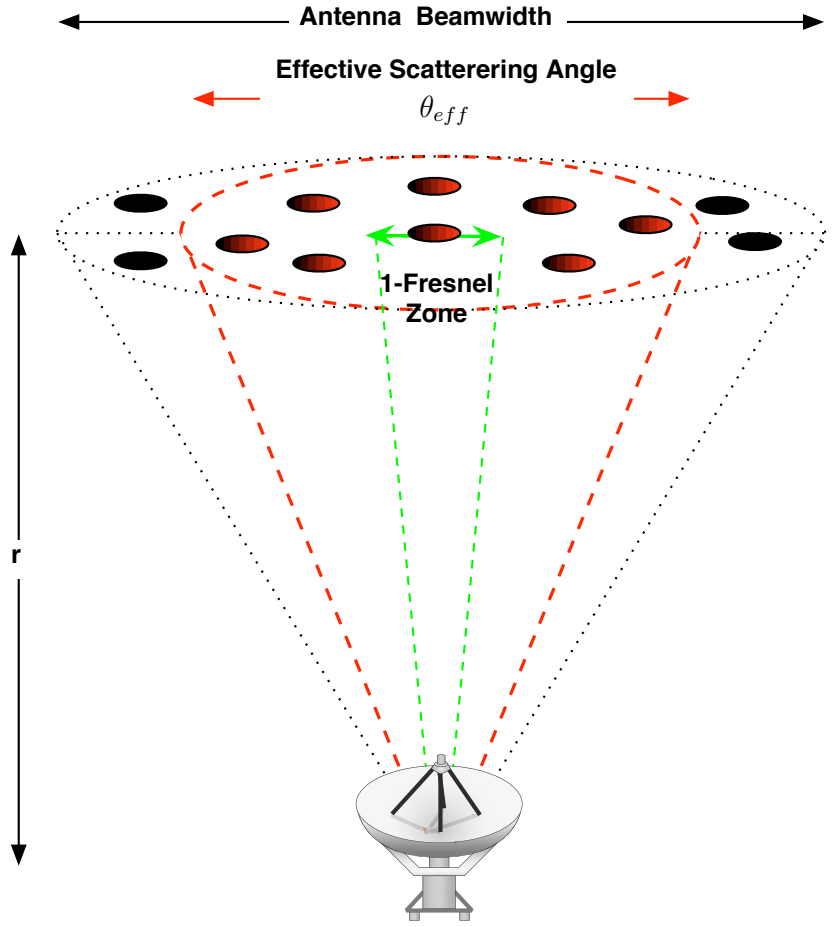

$$P_{rN} \sim N \times (h/L)^4 = n_{\|} n_{\perp} \times (h/L)^4 = n_{\|} (\frac{r \times 2\tan^{-1}(h/L)}{L})^2 \times (h/L)^4$$

Figure 6.1: Received power reduction (P_{rN}) for N scattering elements smaller than 1-Fresnel zone.

of N scatterers in Figure 6.1. The vertical distribution of scatterers in the range gate has been taken into account since the rocket cuts across the structures in that direction. Combining all these terms we get the following expression for reduction in received power for N anisotropic scatterers:

$$P_{rN} \sim N \times (h/L)^4 = n_{\parallel} n_{\perp} \times (h/L)^4 = n_{\parallel} (\frac{r \times 2\tan^{-1}(h/L)}{L})^2 \times (h/L)^4. \quad (6.1)$$

A reduction of 10 dB in received power is obtained for a radar probing a 1 km depth scattering volume at 85 km. This signal reduction has been included and shown in Figure 6.2 as the "$*$" the markers. Similar results were shown previously in Chapter 4 (Figure 4.8) but without the modeled signal reduction factor. The top panel shows predicted reflectivity versus wavenumber for non-summer derived from the DYANA rocket at 85 km. Similarly, the bottom panel shows predicted reflectivity versus wavenumber for summer derived from the MAC/SINE rocket at 85 km. Numerical values for radar reflectivity as a function of frequency are summarized in Table 6.1.

For non-summer conditions, we have found that the two types of scatter, edges and turbulence, are comparable and yield an MF voltage reflection coefficient of about 0.3% (Equation 4.29). These results are in agreement with current understanding of mesosphere scatter above 80 km. For example, Hocking [1987] quotes values of that order for the reflection coefficient and others [Røyrvik and Smith, 1984; Thrane et al., 1994] have indicated a transition to turbulent scatter at such heights. For reference, the volume reflectivity found at the equator by Røyrvik and Smith [1984] at 85 km was $4{\times}10^{-18}$ m^{-1}. This is in excellent agreement with the projected turbulent scatter based on the Driscoll and Kennedy model for $S_c = 1$ (the black curve in Figure 4.8a). The latter supports the validity of our calculations and suggests that turbulent scattering mechanisms predominate in the mesosphere

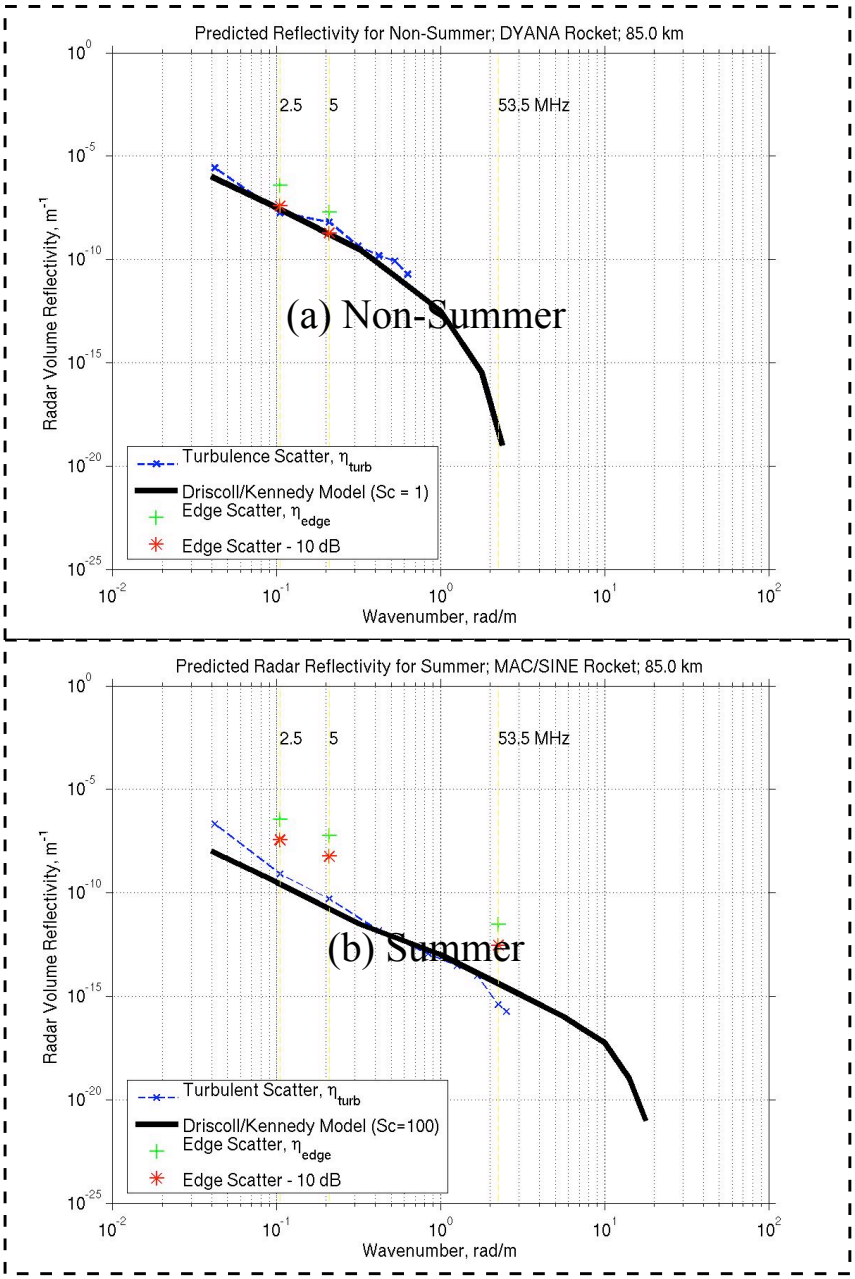

Figure 6.2: Predicted radar reflectivity, η_{turb} and η_{edge}, versus wavenumber, k, for (a) non-summer and (b) summer periods. The Driscoll and Kennedy model for turbulent reflectivity is superimposed for $S_c = 1$/Non-summer and $S_c = 100$/Summer.

Table 6.1: Predicted radar reflectivity values for 85 km derived from non-summer (DYANA) and summer (MAC/SINE) rocket measurements of electron density.

Rocket Flight	Altitude (km)	Radar Frequency (MHz)	Turbulent Reflectivity (m^{-1})	Edge[1] Reflectivity (m^{-1})
DYANA[2]	85	2.5	$10^{-7.5}$	$10^{-7.5}$
		5	$10^{-8.0}$	$10^{-8.5}$
		53.5	-	-
MAC/SINE	85	2.5	$10^{-9.0}$	$10^{-7.0}$
		5	$10^{-10.0}$	$10^{-8.0}$
		53.5	$10^{-15.0}$	$10^{-12.5}$

[1] Power reduction model is included. [2] The DYANA sensor resolution was not high enough to allow the estimation of non-summer VHF/53.5 MHz radar reflectivity.

during non-summer periods.

In the polar summer, the VHF scatter estimates are about 40 dB stronger than the expected values for non-summer (Figure 6.2b). The edges do have a significant effect at all frequencies even including the signal reduction due to aspect sensitivity. These results support the experimental data presented in Chapter 3, showing that MF radars are affected in a measurable way by the layering associated with polar mesospheric phenomena. Since the summer rocket detector had good resolution we could calculate the turbulent scatter contribution at VHF (blue curve). It is a significant component of scatter but less than the strongest edge components.

6.3 Dust Phenomena

We have also presented evidence that mesospheric dust particles lead to layers that coincide with structured echoing at MF frequencies (Chapter 5). Dust particles of meteoric origin are known to exist in the mesosphere where they can scavenge electrons. The layering may be due to their production as ablation products and slow diffusion. Kelley et al. [1987] flew a rocket through an ablation trail and found it to have a very high Schmidt number and an enormous 50 MHz backscatter coefficient. Normal meteors, most likely, have similar dust products but on a much smaller scale. Unlike VHF scatter, a large Schmidt number is not needed at MF/HF frequencies since the wavelengths are larger than the Kolmogorov microscale, and layers may be sustained at low charging levels. All these factors could explain the existence of dust scatter at MF frequencies and the non existence of an analogous radar mechanism at higher frequencies.

The dust effects identified by both rockets or radars are certainly intriguing. The fact that polar summer MF and HF scattering seem to be affected by mesospheric layers associated with charged ice naturally leads to the suggestion that charged dust could affect MF scattering at other latitudes and seasons. The small charged dust particles in these locations are not thought to greatly increase the Schmidt number, which is consistent with the absence of VHF scatter. On the other hand, if the dust is layered due to meteor deposition, structured MF scattering might occur even with modest Schmidt numbers.

6.4 Climate Change, Radar Remote Sensing, and the Importance of Mesospheric Ice/Dust Research

The potential of PMSE and/or NLC to trace possible changes in global temperatures remains an object of intense debate. Questionings are primarily due to the limited number of observational databases using either radio or optical techniques [von Zahn, 2003]. It has only been 20 years since the discovery of PMSE. NLC observations have been taken for a little more than a century but systematic observations, either by satellite or trained observers, have been carried out on a near-continuous basis only for the last 40 years [von Zahn, 2003]. What is clear is that PMSE and NLC are related to low temperatures and ice formation at altitudes near the mesopause region. The proliferation of NLC, which is commonly linked with a decrease in mesopause temperatures and an increase in water vapor, might be directly associated with higher temperatures experienced by the Earth's lower atmosphere [Amos, 2006; Phillips, 2003]. An increase in the primary greenhouse gases, carbon dioxide (CO_2) and methane (CH_4), due to human activities would have the effect of trapping the Earth's infrared radiation at tropospheric/stratospheric altitudes, eventually making the near atmosphere warmer and the "isolated" mesosphere colder. An increase in greenhouse gases would have the additional effect of increasing the amount of water vapor reaching mesopause altitudes, a necessary ingredient for ice formation and PMSE/NLC [Thomas, 1996; Thomas et al., 2003].

We still do not have a full explanation for the radar scattering associated with PMSE. This makes it difficult to quantify the radar returns using solid arguments. We have made an effort along those lines but we need more in-situ and truly col-

located radar measurements. Also, the potential and limitations of radar sensors operating at multiple frequencies should be exploited in order to maximize the amount of information extracted from ice or dust phenomena. In any case, radar remote sensing for mesospheric investigation offers many advantages over other observational techniques. Two examples are its unattended operation capability, and independence of local weather conditions. The interpretation of the radar gathered information imposes limitations but with many more multi-wavelength and in-situ measurements, using more sophisticated instrumentation, many of those gaps will be filled. Different than other atmospheric regions, the number of in-situ mesospheric measurements for radar validation are scarce.

The study of mesospheric ice or dust particles by means of radar techniques could dramatically advance our knowledge of the dynamical and physical processes in the lower thermosphere. As an example, gravity wave activity and winds at mesospheric altitudes could be characterized using radar measurements of ice and dust particles, both natural tracers of atmospheric motions. Coupling with lower atmospheric regions could be established following the dynamics of PMSE or dust layers. A very good understanding of the formation, growth, and evolution of ice/dust particles could be retrieved from continuous radar observations of PMSE in conjunction with other techniques, e.g., lidars, satellites, and rockets. Multi-year radar observations of PMSE, given their association with extremely low temperatures, would be helpful in quantifying and tracing possible changes in global temperatures. All these efforts will be highly valuable for the advance of science and technology, and in the meantime, many lessons could be learned about what types of policies should be created, continued, or eliminated regarding the protection of the environment.

Chapter 7

Conclusions and Future Work

The radar frequency or wavenumber (k) dependency of Polar Mesosphere Summer Echoes (PMSE) has been treated in several ways. Multi-frequency radar observations show that PMSE events can correlate very well from frequencies as low as 2.43 MHz to as high as 139 MHz. Echoes at the higher frequencies are more sporadic and weaker compared to their HF counterparts. MF radars show highly organized PMSE layers quite often but are more susceptible to ionospheric absorption and higher altitude returns associated with geomagnetic activity. Both phenomena produce a blanking effect in MF PMSE, which at times can persist for hours. HF and VHF radars are less affected by absorption events but the PMSE echoes become weaker as the radar frequency increases.

A long-term analysis of MF radar data collected at Poker Flat, Alaska, showed a good agreement with a similar study of PMSE at VHF conducted by Balsley and co-workers in the early 1980s. The annual occurrence of MF radar mesospheric echoes shows a sharp increase (between 80 and 95 km) beginning in May that persist until approximately mid-August, as expected for PMSE. Non-summer enhancements of MF backscattered signal (below 80 km) are thought to be produced by mesospheric turbulence and layering associated with charged dust particles. Comparisons between simultaneous MF radar data and four rockets measuring mesospheric dust over Poker Flat during March 2002 support the latter idea. A possible explanation for the lack of dust scatter at higher frequencies is that unlike VHF scatter, a large Schmidt number is not needed at MF/HF frequencies (since the wavelengths are larger than the Kolmogorov micro-scale) and layers may be

sustained at low charging levels.

Radar reflectivity calculations derived from rocket data collected during summer and non-summer periods indicate that the edge scattering mechanism is important at MF/HF/VHF frequencies in the polar summer mesosphere. The results are ambiguous for other seasons. The observed tendency of PMSE patches to be located at lower altitudes for the higher frequencies is also seen in the predicted radar reflectivity profiles. Previous work using lidar and radar concurrently showed the same type of structuring in NLC/PMSE patches, indicating larger particles at lower altitudes. The radar results may be due to a height dependence in the Schmidt number. The HF radar capabilities to study mesospheric layered phenomena are supported by our numerical predictions of radio backscatter. This could explain the fact that MF radars detect PMSE reasonably well from time to time, assuming that ionospheric absorption and geomagnetic activity are not mitigating factors.

Table 7.1 summarizes some of the major advances of PMSE observational research, in the context of multi-frequency radar observations, during the last 25 years. Prior to 2000, most works focused in understanding PMSE characteristics at VHF frequencies; little work was carried out at MF and HF radar frequencies. The development of the HAARP HF facility in the late 1990s enabled us to observe PMSE concurrently at multiple HF frequencies, in addition to MF and VHF frequencies, using on-site and nearby Alaskan radar facilities. The operation of VHF radars at HAARP was key in clearly identifying MF/HF PMSE returns. UHF observations are not discussed in this thesis but the on-going deployment of AMISR (Advanced Modular Incoherent Scatter Radars) UHF radars in Alaska opens new frontiers for the understanding of PMSE and upper mesospheric phe-

nomena in general [R. Cuevas, personal communication, 2006]. Below are some ideas for future research.

On the basis of echo duration and signal strength, we suggest that HF radars would be optimal for PMSE monitoring. Nearly vertical pointed HF radars deployed along a longitude line, at latitudes above 50 degrees, could give insights on possible global change trends associated with PMSE. In the meantime, statistical analyses of data gathered with the existing global network of MF radars, which have been in continuous operation for almost two decades, would help to identify long-term tendencies in PMSE and perhaps the Earth's climate. MF databases from different locations should be exploited to confirm if there is any indication of dust layering at other latitudes and/or seasonal trends.

On a research campaign basis, an ideal scenario for future efforts should include the use of portable or permanent VHF radars operating at several frequencies, e.g., 50 MHz and 139 MHz. As soon as one of these systems detect a PMSE event, the larger and more expensive HF systems could come into operation. Off-site SuperDARN HF radars, pre-programed for higher temporal and spatial resolutions, could be useful providing information on local and regional ionospheric conditions favorable for PMSE occurrence. An incoherent scatter radar system could provide information on the electron environment leading to PMSE and ice layering. A lidar system could give temperature retrievals and more importantly, identify ice and dust particles in the mesopause region [Collins et al., 2003; Gelinas et al., 2005]. The relationship between multi-wavelength PMSE and ice particles could be determined for the first time with such an experimental setup. A similar set of observations should be carried out during the summer and winter seasons. For the latter, the lidar system would indicate favorable conditions for dust occurrence in

Table 7.1: Overview of PMSE observational research during the last 25 years and sample references.

Frequency Band	Prior to 2000	Post 2000
Medium Frequency (MF)	Some hints of PMSE, Ambiguous echo discrimination Bremer at al., 1996	Fully validated MF PMSE, Geomagnetic activity and absorption effects, Scattering predictions Ramos et al., 2006
High Frequency (HF)	Layered HF echoes near mesopause Karashtin et al., 1997	Layered echoes at multiple HF frequencies, Lidar/HF radar comparisons, Fully validated HF PMSE, Scattering predictions Kelley et al., 2002 Collins et al., 2003 Ogawa et al., 2003 Ramos et al., 2006
Very High Frequency (VHF)	Pioneer PMSE work, Structure and dynamics, Radar/rocket comparisons, Aspect sensitivity studies Ecklund and Balsley, 1981 Röttger et al., 1988 Kelley and Ulwick, 1988 Czechowsky et al., 1988	Heating effects, Comparisons with MF/HF PMSE, Scattering predictions Chilson et al., 2000 Alcala et al., 2001 Havnes et al., 2003 Ramos et al., 2006

the mesosphere. Alternatively, forward scatter of a strong HF transmitter such as HAARP could be received on a polar orbiting spacecraft to detect the equatorward edge of the PMSE region as a function of season. Just such a possibility exists with the launch of the Canadian E-POP (Enhanced Polar Outflow Probe) satellite [G. James, personal communication, 2005].

Collocated rocket measurements of electron and/or dust density would be a magnificent addition to the radar and lidar observations. Numerical predictions for radar reflectivity (versus wavenumber) should be performed using rocket electron density data collected when dust layers are present. The reflectivity estimates presented in this thesis covered only the interval of 80 to 90 km. Other altitudes and historical rocket databases should be considered, specially when simultaneous radar data are available. We recognize that the proposed experimental scenario is extremely ambitious but not impossible with the proper funding and scientific collaboration.

APPENDICES

A.1 Radar Analysis and Mesospheric Observation System (RAMOS)

A.1.1 HF Radars at HIPAS and HAARP

The Radar Analysis and Mesospheric Observation System[1] (RAMOS) consists of two HF radar receiving stations designed and configured for PMSE observations at the HIPAS and HAARP ionospheric observatories in Two Rivers and Gakona, Alaska, respectively. The following hardware and software components are required to assemble both HF receiving stations. Refer to Figures A.1 to A.4 for descriptions of the system diagrams and pictures of each radar site.

Hardware:

1. HF Quadrature Receiver
2. Digital Oscilloscope and Synthesized Signal Generator
3. National Instruments (NI) DAQ-6110E Digitizer
4. NI SCB-68 DAQ Connnector
5. Desktop Computer running Windows Operating System

[1]RAMOS: Radar Analysis and Mesospheric Observation System [v3.0]. A MATLAB® graphical interface to control radar experiments and acquire ionospheric data using an HF receiver, a personal computer, and National Instruments acquisition devices. Real time and off-line processing software. C. Ramos/2003.

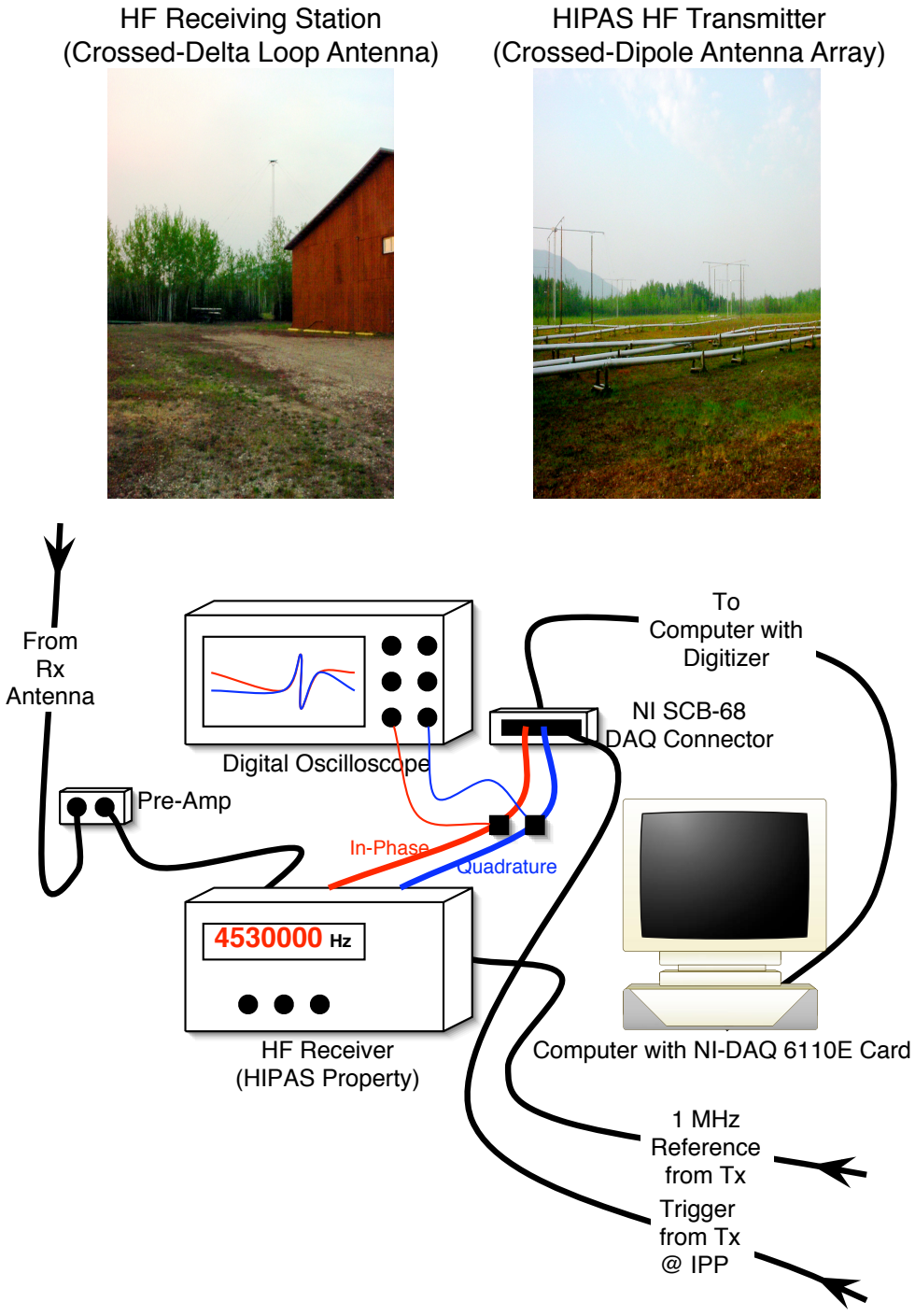

Figure A.1: HIPAS HF Radar Receiver Setup

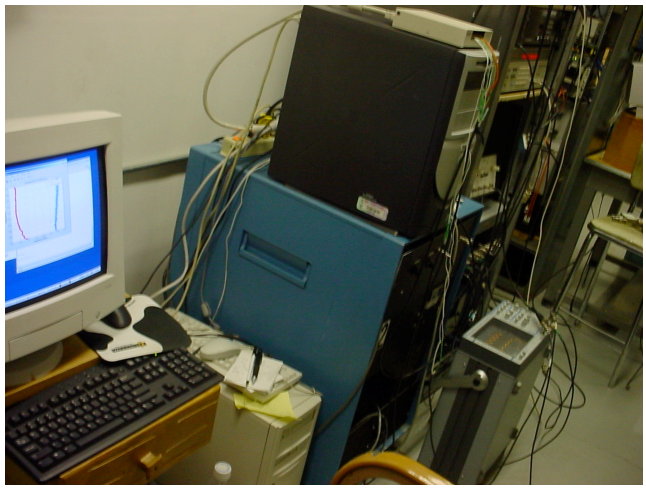

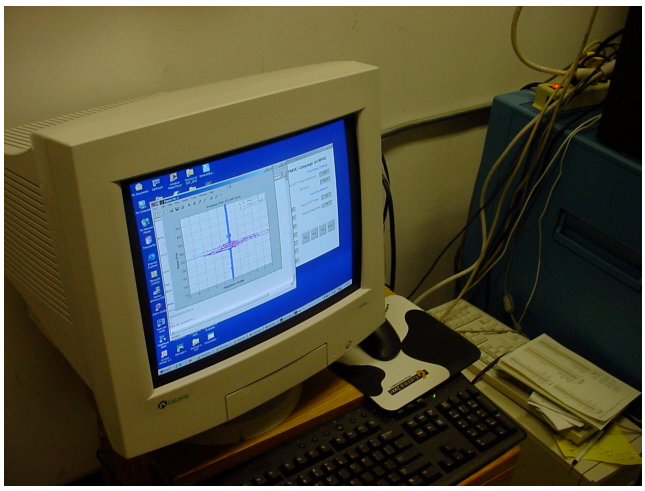

Figure A.2: The HIPAS HF Receiving Station

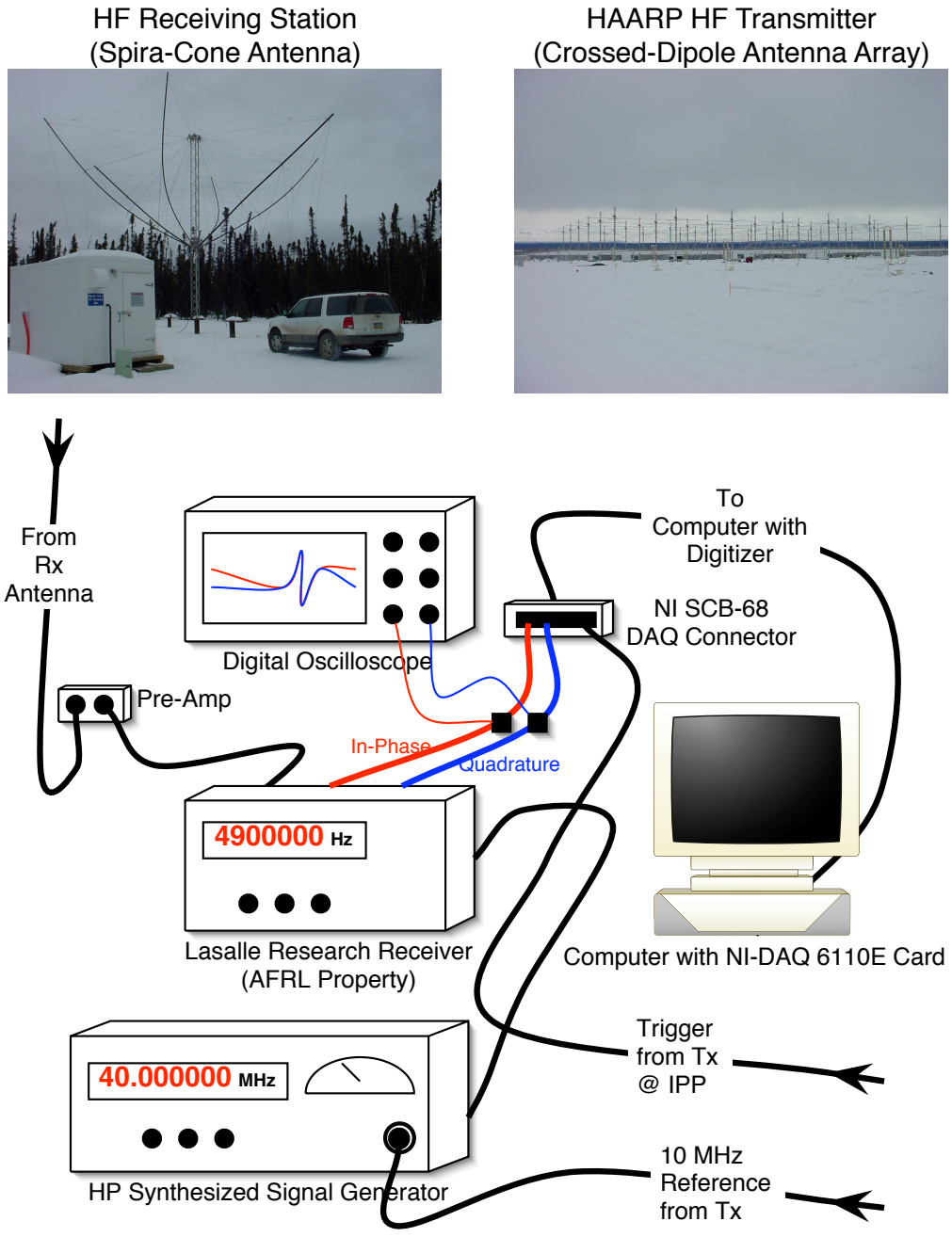

Figure A.3: HAARP HF Radar Receiver Setup

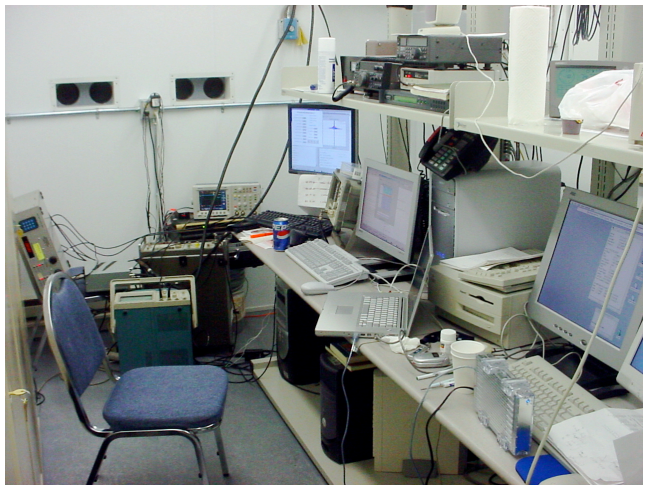

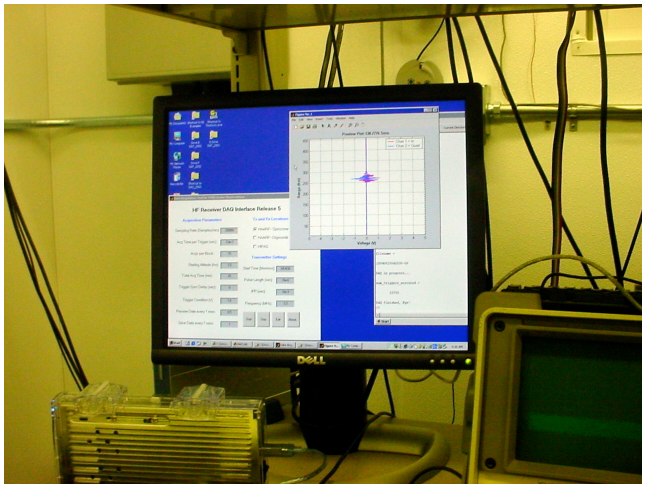

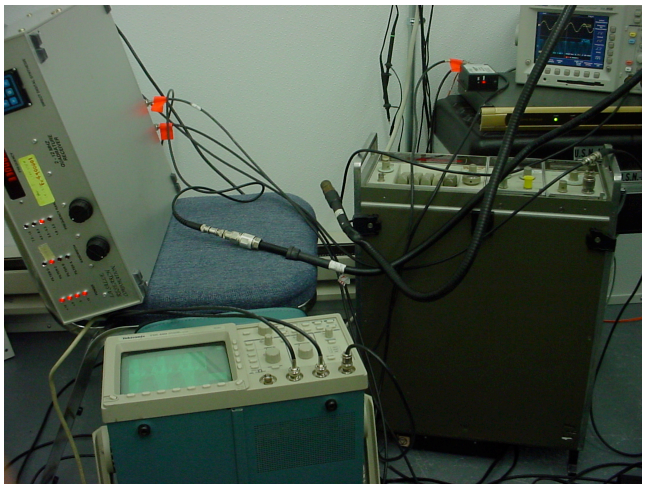

Figure A.4: The HAARP HF Receiving Station

Software:

1. MATLAB for Windows with Data Acquisition Toolbox
2. NI-DAQ Driver Software
3. NI Measurement and Automation Explorer Software
4. MATLAB Data Acquisition Software (DAQ m-files[1])

A.1.2 Data Acquisition System

The software used to control data collection at HIPAS was written in the MATLAB programming language. Eventually, it was modified for usage at the HAARP facility. The user must enter the acquisition parameters listed in Table A.1 using the Graphical User Interface (GUI) shown in Figure A.5. MATLAB communicates with C-libraries provided by a vendor, National Instruments, which sends instructions to the acquisition hardware, PCI-6110E. The latter samples the In-Phase (I) and Quadrature (Q) outputs from the HF receiver each time a synchronization (Sync) pulse, running at the inter-pulse-period, is detected by the PCI-6110E trigger input (see Figure A.6). Refer to Figure A.7 for a description of the PCI-6110E card pin assignments. The I and Q samples, as a function of time (or radar transmitted pulse) and range (or time delay), are automatically written to memory and the computer disk during the experimental run.

HF Radar Operation/Data Acquisition Checklist

The following checklist is intended only as a guide for the operation of the HF radar receiving stations at HIPAS and HAARP. The user can always modify the system to accomplish his/her specific needs or experimental goals.

1. Install software and hardware listed in section A.1.1.

2. The Trigger Sync signal must be connected to the analog input **Channel 0** of the PCI-6110E card (see Figure A.7).

3. The In-Phase receiver output must be connected to the analog input **Channel 1** of the PCI-6110E card.

4. The Quadrature receiver output must be connected to the analog input **Channel 2** of the PCI-6110E card.

5. Copy DAQ m-files to desktop computer.

6. Verify that the computer has enough space for data storage (see Section A.1.4).

7. Open NI Explorer Software.

8. Test the digitizer using National Instruments Explorer Software. Use a known waveform, e.g., sine wave, as input to the digitizer channels. Verify that each analog input channel is connected properly. Similar waveforms should be shown simultaneously by the Explorer software and the oscilloscope if the digitizer is working correctly.

9. Test the trigger input using Explorer software. Ask the HIPAS or HAARP operator to run a Sync signal for testing purposes. HF transmissions are not necessary for this part.

10. Exit Explorer software if both analog channels and the trigger input of the digitizer are working properly.

11. Verify that the HF receiver is working properly. Use a test signal, e.g., sine wave, as the antenna input. Look for any channel unbalance or phase error. The I and Q receiver outputs should have similar magnitudes and a phase difference of 90°.

12. Verify that the 1 MHz reference signal (for Doppler) is powered on and connected to the HF receiver.

13. Open MATLAB.

14. Change current working directory to the DAQ directory or the location of the m-files copied in step 5.

15. Open m-file *run_daq_script_v5.m* and modify line #21 (*pathname* = ...). Put the full location of the directory where data files will be saved. Verify that lines #43 and #45 are in agreement with hardware setup.

16. Type *run_daq_gui_v5* in the MATLAB prompt to open the GUI interface (Figure A.5).

17. Modify relevant GUI input fields (see Table A.1). It is recommended to keep fields 1, 2, 3, 4, 7, 8, and 9 with their default values. Change fields 5, 6, 10, 11, 12, 13, and 14 according to the HIPAS or HAARP system parameters and the specifications of the HF transmissions. Test DAQ software before the real radar run using Sync signals sent out from the transmitter building.

18. Press the Start button several seconds before the "Start Time" indicated in field 11 (5 or 10 seconds prior to the beginning of the HF transmission is fine). The DAQ software can be started or re-started any time within the

radar operation as long as the Sync signal is running. The software crashes if the Sync signal is lost or turned off.

19. MATLAB should show a message indicating that data acquisition is in progress after the "Start Time" indicated in field 11.

20. Verify that the oscilloscope and the MATLAB preview plot are in agreement. PMSE echoes (Height $\simeq$ 85 km or Delay $\simeq$ 0.6 ms) should be weaker than the F-region echoes (Height $\simeq$ 300 km or Delay $\simeq$ 2 ms). Use Tx Sync signals to synchronize scope traces. The time delays shown in the oscilloscope must correlate with the Height Scale (Y-Axis) shown by the DAQ Preview Plot. Both traces shown in the Preview Plot (Channels 1 and 2) should have comparable magnitudes in voltage. If they do not, look for a bad connection or in the worst case, a channel unbalance inside the receiver. Most software crashes are due to a lack of Sync signal. Call the operator if the Sync or the 1 MHz reference signals are lost. Re-start the MATLAB DAQ software. Take notes if unexpected problems occur.

21. Check the data directory to verify if data files are being created. One new binary file should be created every minute if the field 9 was set to 1.

22. If a second computer is available, use MATLAB post-processing tools to read the data files over the network. The analyzed data sets should make sense and be consistent with the real time profiles shown by the oscilloscope and in the DAQ preview plot.

Table A.1: Graphical-User-Interface (GUI) input fields for HF data acquisition

Parameter	Description	Example
1. Sampling Rate	Sampling rate for data collection	200,000 Hz
2. Acquisition Time per Trigger	Acquisition Time per Transmitted Pulse	3 ms (for 450 km)
3. Acquisitions per Block	Number of Acquisitions per "block" of data	75
4. Starting Altitude	First sampled altitude in the atmosphere	50 km
5. Total Acquisition Time	Length of experimental sequence	60 minutes
6. Trigger Sync Delay	Delay between HF transmissions and Sync arrival to Rx building	1 us
7. Trigger Condition	Voltage condition for acquisition	1 volt
8. Preview Data	Time interval for "real" time monitor updates	1 minute
9. Save Data	Amount of data per data file	1 minute
10. Tx and Rx Locations	Radar Tx/Rx Locations	HIPAS
11. Start Time	Time of Experiment	19:00:00 UT
12. Pulse Length	Pulse Length	10 us
13. IPP	Inter-Pulse-Period	15 ms
14. Frequency	Radar Frequency	4.53 MHz

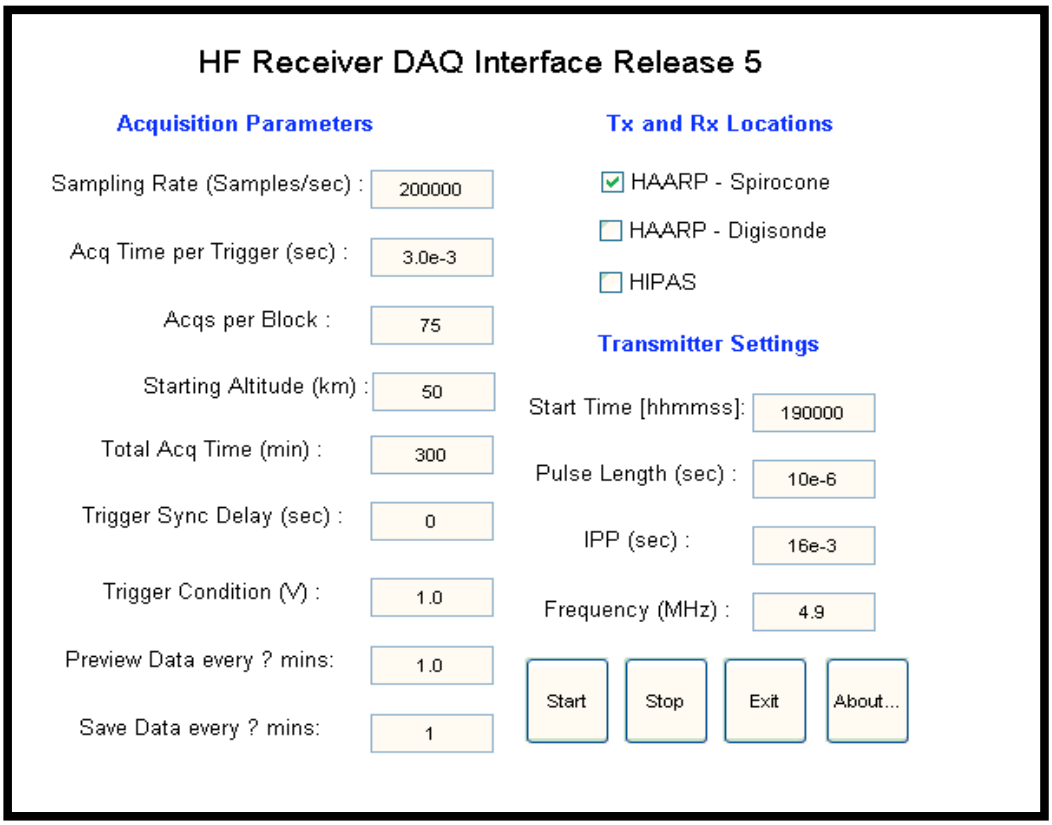

Figure A.5: MATLAB® GUI for HF data acquisition [C. Ramos/2003]

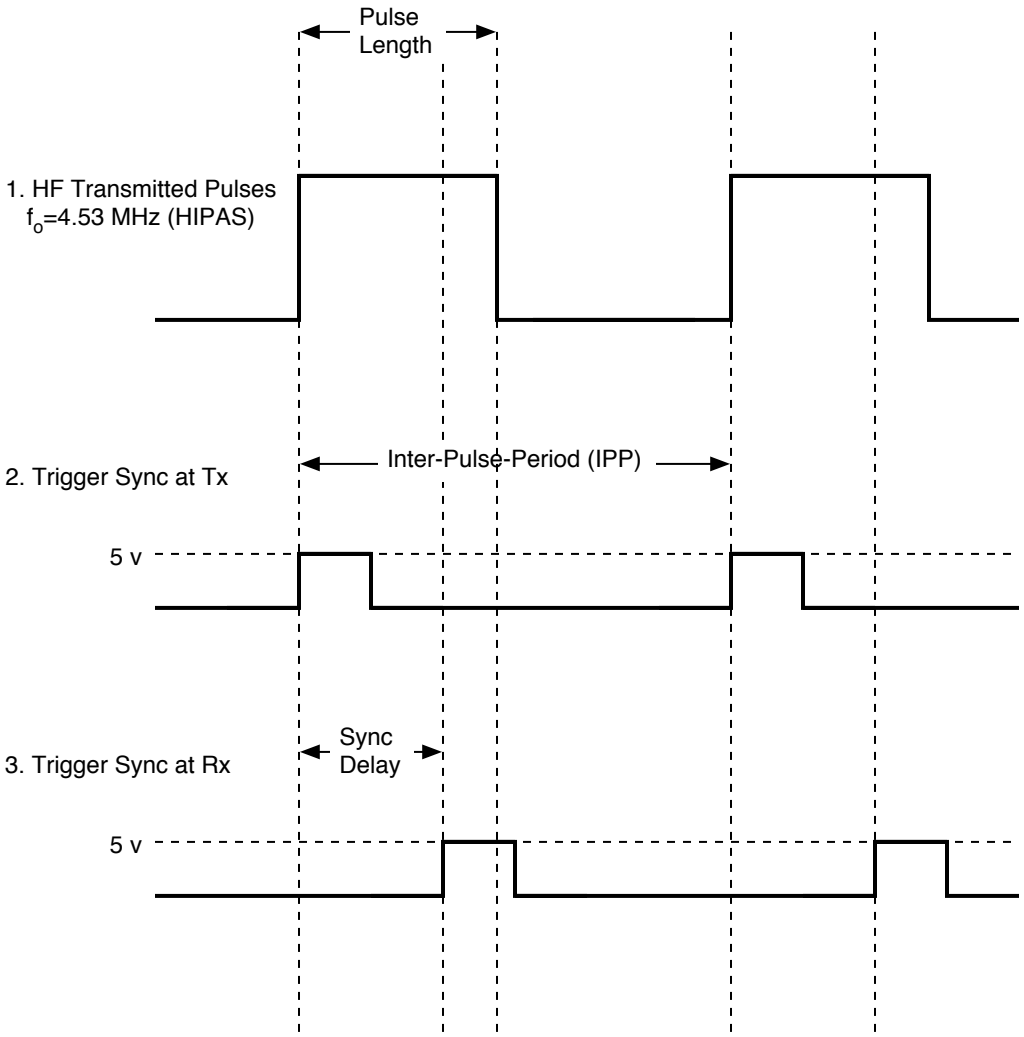

Figure A.6: Timing diagrams for HF radar transmissions

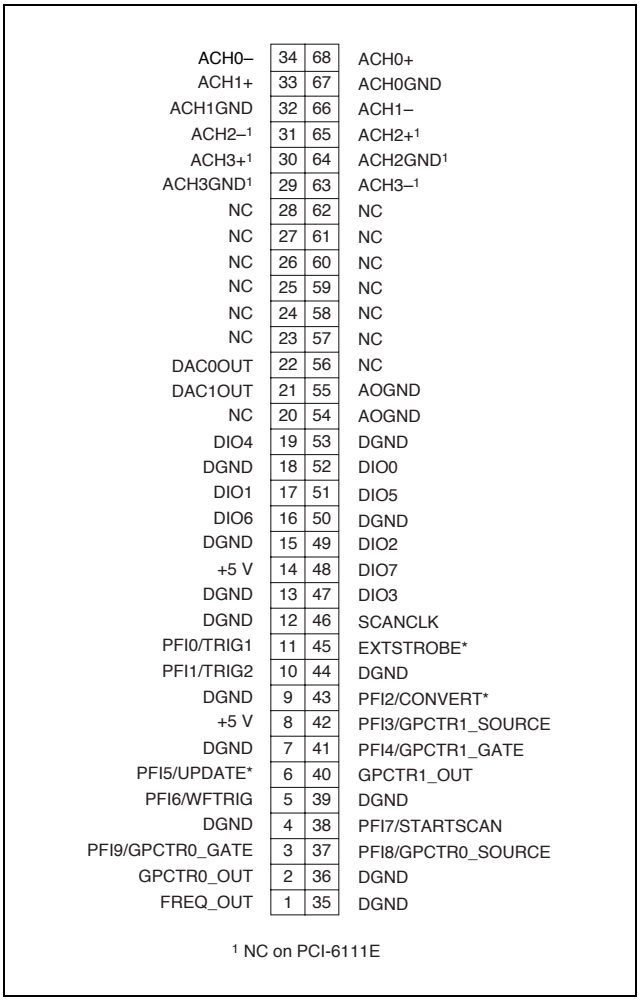

Figure A.7: Input/Output Connector Pin Assignment for the PCI-6110E digitizer/card. Adapted from *PCI-6110E/6111E User Manual*, National Instruments Corporation, 1998.

Table A.2: HF Header Data Structure

Acquisition Parameter	Variable Name	Data Type	Example	Units
Year	y	float[1]	2003	UT
Month	m	float	7	UT
Day	d	float	3	UT
Hour	hh	float	18	UT
Minutes	mm	float	0	UT
Seconds	ss	float	0	UT
Sampling Rate	Sr	float	200000	Samples/Second
Acq Time per Trigger	TimeAcq	float	3e-3	Seconds
Total Acq Time	TotalTime	float	15	Minutes
Trigger Sync Delay	TimeDelay	float	0.1e-3	Seconds
Pulse Length	PulseLength	float	10e-6	Seconds
Inter-Pulse-Period	IPP	float	10e-3	Seconds
Acqs per Block	AcqsBlk	float	100	-
Starting Altitude	StartAlt	float	50	km
Frequency	RadarFreq	float	4.9	MHz
HF Facility	RadarName	char[2]	'HAARP02'	-
Block Data Size[3]	NumSamples	float	60000	-
Data Maximum	DataMax	float	10	Volts
Data Minimum	DataMin	float	-10	Volts

[1]Floating point, 32 bits. [2]Character, 8 bits.

[3]I or Q samples per Acquisition Block, NumSamples=Sr*TimeAcq*AcqsBlk.

A.1.3 HF Radar Data Format

The HF data files, written in binary format, consist of a header and a contiguous array of numbers of I and Q voltages as a function of range and time. Detailed descriptions of both data structures are given in Tables A.2 and A.3. The stream of I and Q voltages sampled by the PCI-6110E digitizer are read as signed "float/32-bit" numbers, the MATLAB's default data type, with values ranging from -10.0 to 10.0 volts. Formula A.1 is used to convert the I and Q "float/32-bit" samples to unsigned "integer/16-bits" numbers before writing them to a data file.

$$[DataUint] = ([DataFloat] - DataMin)/DataRange * 65535, \qquad (A.1)$$

In the above expression $DataFloat$ is a vector of either I or Q values, $DataRange = DataMax - DataMin$ is the dynamic range of the digitizer, and $DataUint$ is a new vector containing a stream of unsigned integer I or Q values ranging from 0 to 2^{16}-1=65,535. This "float2uint" conversion allows us to save 50% in storage space. An inverse conversion procedure must be performed when reading the raw binary files for their analysis.

A.1.4 An Example of a Data Collection Sequence

For a radar experiment lasting say TotalTime = 15 minutes, and using the acquisition parameters listed in Table A.2, the number of acquired samples per trigger would be St = Sr*TimeAcq = 600 samples, covering an ionospheric region of 450 km or TimeAcq = 3 ms, from StartRange = 50 km up to 500 km. Each acquisition block would be completed in TimeBlk = AcqsBlk*IPP = 1 second per block and a total of NumBlk = TotalTime*60/TimeBlk = 900 acquisition blocks, each one consisting of two sets of NumSamples = St*AcqsBlk = 60000 numbers, would be

Table A.3: HF I/Q Data Format

Acquisition Parameter	Variable Name	Example	Units	Data Type	Array Size[1]
In-Phase	I	0.10	Volts	ushort[2]	60000
Quadrature	Q	-0.05	Volts	ushort	60000

[1]Array size is computed using parameters listed in Table A.2.

[2]Unsigned integer, 16 bits. The acquired I/Q voltages are float/32-bit numbers but they are converted to unsigned integers (16-bits) before writing them to a data file.

performed sequentially and written to one data file, or multiple data files if desired, during the entire experiment. The final size for a single data file consisting of the full experimental run (without any coherent integration) is approximately 216 Mbytes (Table A.4). The data filename is, by convention, the time when the acquisition engine begins the data collection, e.g., '20030703180000-01.DAT'. If smaller data files are desired, a counter is added before the file extension to indicate the order of the data segment. In the above example, if the file size is

Table A.4: Data size calculation for parameters listed in Table A.2

Data Element	Calculation	Size
Header	(18*32 + 7*8)/8	79 bytes
In-Phase	(60000*900*16)/8/1e6	108 Mbytes
Quadrature	(60000*900*16)/8/1e6	108 Mbytes
Total	79/1e6 + 108*2	∼216 Mbytes

specified as 5 minutes, 3 data files of ∼72 Mbytes each one would be created, i.e., '20030703180000-01.DAT', '20030703180000-02.DAT', and '20030703180000-03.DAT'.

A.1.5 HAARP HF Receiver

The HAARP HF receiver was built by La Salle Research Corp. (LSRC) for the Air Force Research Laboratory (AFRL) at Hanscom Air Force Base in Massachusetts. The following documentation was provided by the manufacturer. Contact LSRC for additional details on the hardware and circuit diagrams of the instrument.

La Salle Research Corp. MODEL RXHF-1 Specifications:

Frequency- Direct Digital Synthesis (DDS) – 2-12 MHz

Input- BNC Antenna Connector

Output- Quadrature Outputs may be set to +/- 5 Vdc, +/- 10 Vdc, or 0-5 Vdc. Will drive up to 50 ft of 50 ohm coaxial cable.

AC Power- Wired for 120 VAC 50/60 Hz but may be configured for 240 VAC operation; 2 amp fuse required.

Size- Rack Mount 5.25" H by 19" W by 17" D

Weight- 24 pounds

Reference Oscillator- 40 MHz TCXO

External Oscillator- A 0 dBm external external oscillator may be used.

Factory Installed Baseband Filters- 500 kHz and 100 kHz.

Receiver Overview:

The HF Receiver is a 2-12 MHz receiver was designed by La Salle Research Corp. for atmospheric research work. It consists of four main components, which are shown in Figure A.8. Below is a description of each major component.

RF Stages- The RF stages are mounted in one of two shielded enclosures on the top side of the chassis. They provide the filtering, amplification, and coherent quadrature-detection of the return signals from the antenna system.

Oscillator Module- The oscillator stage is mounted in the second shielded enclosure on the top of the chassis. It consists of a crystal oscillator, used as reference for the Proxim Direct Digital Synthesis board, which generates the operator's choice of operating frequency. The Z-80 microprocessor, along with its keyboard and display, provides for operator selection of receive frequency.

Bessel Filter Board- The Bessel Filter board is mounted on the bottom side of the chassis and provides for appropriate baseband filtering of the quadrature signals from the phase detectors. A choice of four bandwidths is provided.

Power Supply- The power supply section includes two commercially available modules from Power One, which are mounted along one side of the cabinet, as well as an additional regulator, which is on the Bessel Filter board, and is used to provide the power for the RF stages.

Baseband bandwidth is selected from the front panel by a rotary switch. Correct power supply operation is monitored by four LEDs mounted on the front panel.

Theory of Operation:

RF Stages- Mounted in the first section of the shielded RF enclosure are four bandpass filters that are selected using the front panel range switch. Mounted in the second section of the RF enclosure is the first of the 3-stage MMIC amplifiers and an attenuator. The third section of the RF enclosure contains the second of the 3-stage MMIC amplifiers and a second attenuator. The final section of the RF enclosure contains the quadrature detectors. The RF signal from the second MMIC stage is split by a zero degree hybrid and the resulting two signals are applied to the RF ports of their associated detectors. The oscillator module generates the sine and cosine signals required by the phase detectors. The IF output ports of the two detectors contain the quadrature baseband signals that are amplified and filtered by the Bessel Filter board.

Oscillator Module- The oscillator module contains a 40.00 MHz TCXO crystal oscillator that is used as the reference signal for the direct digital synthesizer. A Z-80 microprocessor provides convenient control of the frequency. It accepts inputs from the keyboard, performs keyboard to binary conversion, binary to seven-segment conversion, and drives a seven segment display. The desired operating frequency is selected by entering the frequency on the keypad, pressing the $*$ as the ENTER key and # as the CLEAR key. The serial data from the microprocessor are converted to parallel data as required by the DDS in the interface circuit.

Bessel Filter Board- The Bessel Filter Board contains two amplifier/filter chains for the quadrature detector outputs. There are four separate filters available for each channel. The signals are amplified by their respective input amps,

U1 and U14. The two signals from these amps are used to drive up to four filters per channel. The actual filter modules are mounted on removable "daugther boards" for ease of changing to different bandwidths. Each filter module drives its own amplifier stage, U4, 7, 10, 13 and U18, 21, 24, 27. The appropriate bandwidth is selected by the MUX24 chip by controlling its two TTL-compatible select-lines. Each quadrature signal is further amplified by U29 and U30. These two amplifiers connect to the output connectors through 51 ohm series resistors to minimize any tendency for the amplifiers to oscillate when driving capacitive loads when using long cables.

Power Supply- The power supply consists of two modular power supplies and an additional regulator mounted on the Bessel Filter Board. The power supplies may be configured for either 120 VAC or 240 VAC and operate on 50 or 60 Hz.

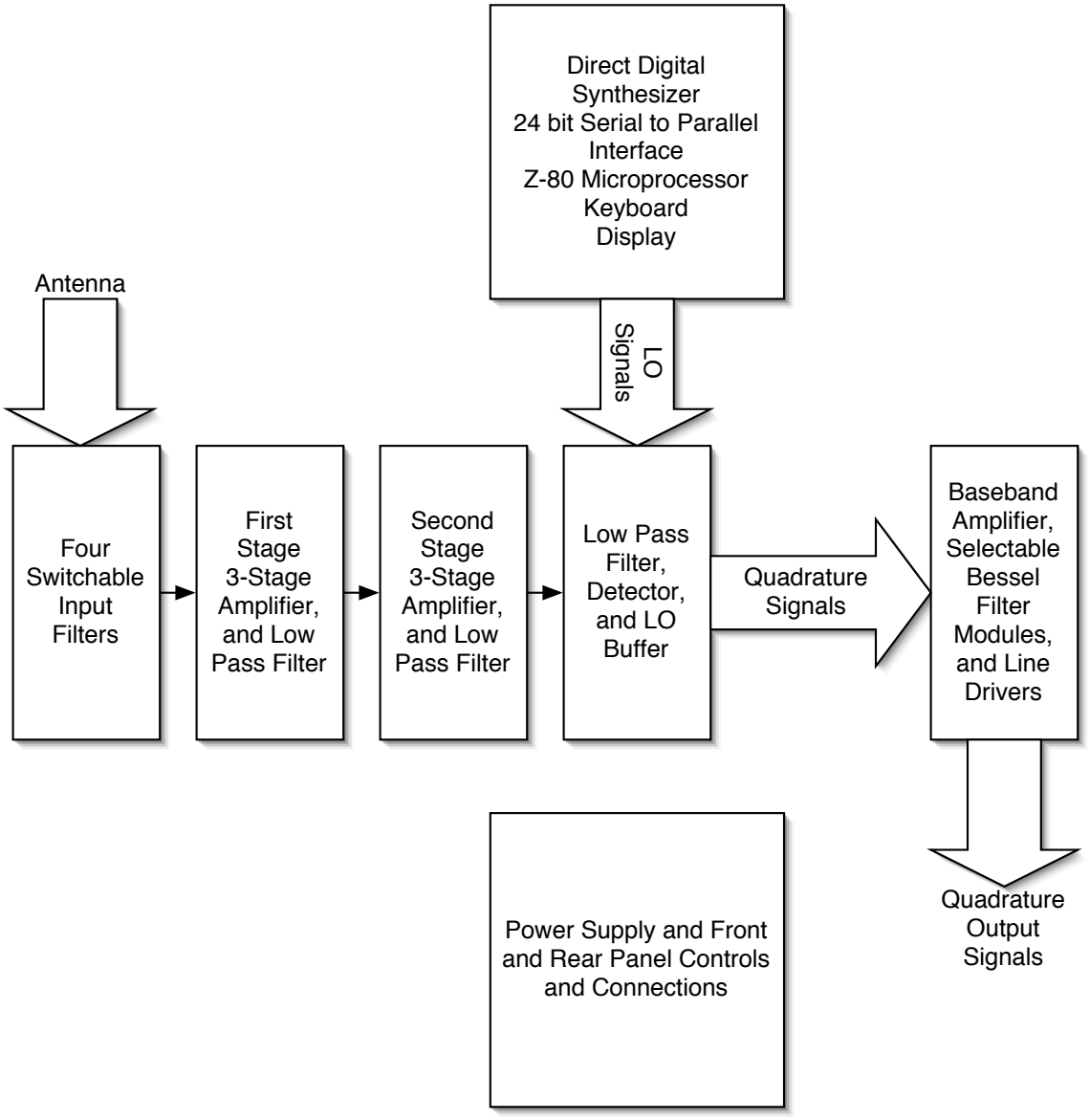

Figure A.8: La Salle HF Receiver Overview [Personal Communication with John Brosnahan, 2003]

A.2 Radar/Rocket Data Inventory

The following tables summarize the radar and rocket databases analyzed in this thesis. We have separated the information on the radar data files based on the year that the experiments took place, 2002, 2003, and 2004. Each table provides details on the radar facility or rocket flight location, transmission frequency, date/time, acquisition parameters, data format, etc. Additional HF data files are available for the summers of 2000 and 2001 but they are not included here since those experiments were intended as proof-of-concept campaigns.

Table A.5: Radar Databases/Summer 2002

Radar Facility	Frequency (MHz)	Number Days	Range (km)	Time UT (hours)	Delta Range (km)	Delta Time (secs)	Data Type	File Type
Poker Flat	2.43	340	50-110	00-24	3	120	Power/Winds	ASCII
HIPAS	4.53	21	50-450	19-21	1.5	$15x10^{-3}$	I/Q	Binary[1]

[1] HF Radar Format. See Appendix A.1 for details.

Table A.6: Radar Databases/Summer 2003

Radar Facility	Frequency (MHz)	Number Days	Range (km)	Time UT (hours)	Delta Range (km)	Delta Time (secs)	Data Type	File Type
Poker Flat	2.43	318	50-110	00-24	3	120	Power/Winds	ASCII
HAARP	4.9	21	50-450	18-22	1.5	$15x10^{-3}$	I/Q	Binary[1]
HAARP	28	10	50-120	*	0.75	$4x10^{-3}$	I/Q	Binary[2]
HAARP	50	10	50-120	*	0.75	$4x10^{-3}$	I/Q	Binary[2]
HAARP	139	14	50-120	00-24	1.5	$10x10^{-3}$	I/Q	Binary[3]

[1] HF Radar Format. See Appendix A.1 for details.

[2] Air Force Research Laboratory (AFRL) Radar Format.

[3] Geospace Research Inc. (GRI) Radar Format.

* Mostly between 20 and 02 UT.

Table A.7: Radar Databases/Winter 2004

Radar Facility	Frequency (MHz)	Number Days	Range (km)	Time UT (hours)	Delta Range (km)	Delta Time (secs)	Data Type	File Type
HAARP	4.9	5	50-450	18-22	1.5	$15\text{x}10^{-3}$	I/Q	Binary[1]

[1] HF Radar Format. See Appendix A.1 for details.

Table A.8: Rocket Databases

Rocket Flight	Location	Date [dd-mmm-yyyy]	Range (km)	Time UT [HH:MM]	Delta Range (m)	Data Type (cm^{-3})	File Type
MAC/SINE	Norway	14-Jul-1987	80-90	09:29	$9x10^{-5}$	N_e	ASCII
DYANA	Norway	11-Mar-1990	80-90	20:42	$13x10^{-4}$	N_e	ASCII
NASA/D1	Alaska	07-Mar-2002	50-100	09:07	$5x10^{-4}$	N_d	ASCII
NASA/D2	Alaska	15-Mar-2002	50-100	11:15	$5x10^{-4}$	N_d	ASCII
NASA/D3	Alaska	15-Mar-2002	50-100	13:03	$5x10^{-4}$	N_d	ASCII
NASA/D3	Alaska	15-Mar-2002	50-100	13:42	$5x10^{-4}$	N_d	ASCII

N_e = Electron Density.

N_d = Dust Charge Density.

A.3 Radar Equation Derivation

The following derivations for the radar equation apply to a mono-static radar system pointed vertically and probing a volume or cross sectional area located within the antenna's far field region. The antenna gain is defined as $G = \frac{4\pi}{\Omega}$ or $\frac{4\pi Ae}{\lambda^2}$, where Ω is the antenna's solid angle in steradians and is approximately equal to the product of the half power beamwidths, $\Omega \sim \theta_{1/2} \cdot \phi_{1/2}$ or $\frac{\lambda^2}{A_e}$. A_e and λ are the effective antenna collection area and the radar wavelength, respectively.

A.3.1 Small (Point) Target

The power density, $S_i[\frac{W}{m^2}]$, intercepting a point target located at some distance or radar range, r, can be defined as

$$S_i = \frac{P_t G \alpha}{4\pi r^2}, \tag{A.2}$$

where P_t is the transmitted power by the radar transmitter, G is the transmission antenna gain, and α is a one-way attenuation factor (see Figure A.9). "Small" in this case means linear dimensions much less than the Fresnel distance defined below. The amount of power scattered, isotropically, by the target, P_s, is determined by its isotropic radar cross section, $\sigma[m^2]$, and the incident power density

$$P_s = \sigma S_i. \tag{A.3}$$

Using the above two expressions the signal power collected by the receiving antenna, P_r, is found to be

$$P_r = \frac{P_s A_e \alpha}{4\pi r^2} = \frac{P_t G^2 \sigma \lambda^2 \alpha^2}{(4\pi)^3 r^4}. \tag{A.4}$$

To obtain the final equation we have expressed the receiving collection area, A_e, in terms of the antenna gain, G. An extra attenuation factor, α, is added to account

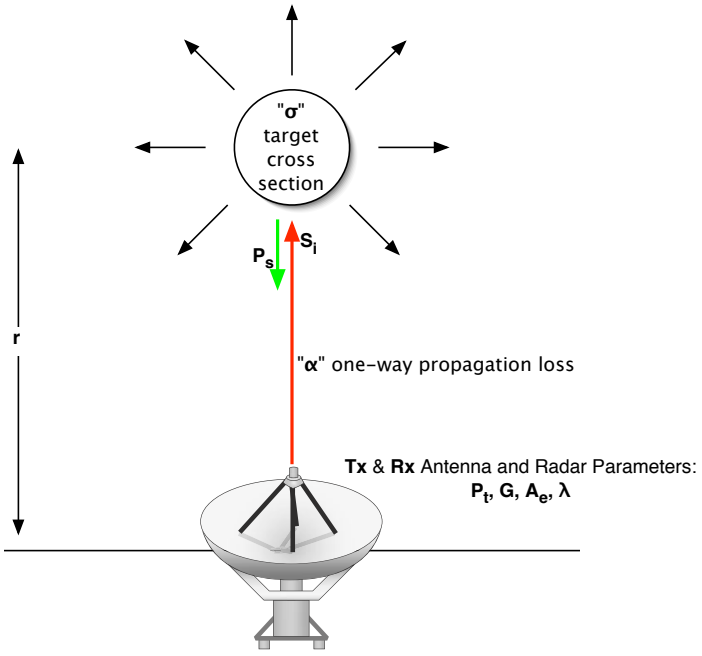

$$P_r = \frac{P_t G^2 \sigma \lambda^2 \alpha^2}{(4\pi)^3 r^4}$$

Figure A.9: The radar equation for a small (point) target

for the two-way radio wave propagation path.

A.3.2 Turbulent Scatter

The radar equation for a point target (Equation A.4) can be extended to apply to volume-filled atmospheric phenomena, such as a homogeneous turbulent medium, by introducing the concept of volume reflectivity, η, which has units of $m^2/m^3 = m^{-1}$. Then the radar cross section of the volume is given by $\sigma = \eta V$. The radar scattering volume can be approximated by

$$V = \pi(\frac{r \cdot \theta_{1/2}}{2})(\frac{r \cdot \phi_{1/2}}{2})\Delta r, \tag{A.5}$$

where Δr is the range resolution of the system, r is the target range, and $\theta_{1/2}$ and $\phi_{1/2}$ are the antenna full half power beamwidths in the two angular directions. When we express σ in terms of η in Equation A.4 and substitute the above expression for V, we find the so-called radar equation for turbulent scatter:

$$P_r = \frac{P_t A_e \Delta r \alpha^2}{16 r^2} \eta_{turb}. \tag{A.6}$$

A similar expression holds for incoherent scatter, which is also volume-filling scatter.

A.3.3 Edge or Fresnel Scatter

To derive the radar equation for Fresnel reflection and Fresnel, or edge scatter, we begin relating the incident and scattered signal powers (P_i and P_s, respectively) at a radar range, r, to the power reflection coefficient of an infinite size reflecting layer, $|\rho_s|^2$. We should distinguish the concepts of Fresnel reflection and Fresnel scatter. Fresnel reflection refers to scattering from a single layer or multiple layers containing variations in refractive index. Fresnel scatter is a volume scattering process that leads to specular reflections and is generally treated by means of statistical analyses. Fresnel reflection is only detectable from a region of the layer smaller than or equal to the first Fresnel radius $R_f = \sqrt{\frac{\lambda r}{2}}$, where λ is the radar wavelength and R is the distance to the target or the radar range. The scattered power is

$$P_s = P_i \cdot |\rho_s|^2 = \frac{P_t G}{4\pi r^2} \cdot \sigma \cdot |\rho_s|^2. \tag{A.7}$$

Here σ, previously the radar cross section for a point target, refers to the collection area of the incident power density, which we can express in terms of the Fresnel

radius as

$$\sigma = \pi R_f^2 = \frac{\pi \lambda r}{2}. \tag{A.8}$$

The received power, at ground level, is found after adding an extra gain term to the radar equation, a scattering gain due to the preferred direction of the specular reflection and the fact that receiving collection area at ground level, $A_{2r} = 2\pi\lambda r$, increases by a factor of 4 relative to the collection area at the target range, σ (see Figure A.10). The new scattering gain (relative to an isotropic radiation pattern) is defined as

$$G_s = \frac{4\pi r^2}{A_{2r}} = \frac{2r}{\lambda}. \tag{A.9}$$

The equation for received power takes the form

$$P_r = \frac{P_s G_s A_e}{4\pi r^2}. \tag{A.10}$$

Substituting the expressions for P_s and G_s in A.10, we obtain the radar equation for Fresnel reflection or edge scatter

$$P_r = \frac{P_t A_e^2 |\rho_s|^2}{4\lambda^2 r^2}. \tag{A.11}$$

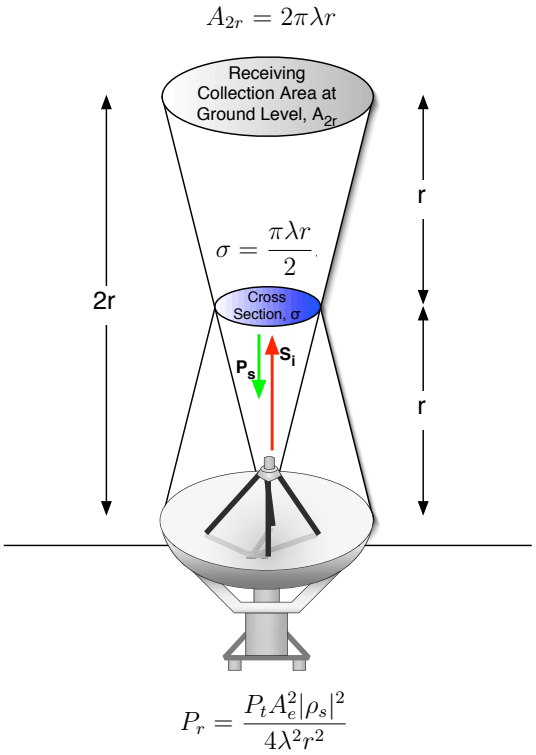

Figure A.10: The radar equation for edge scatter

A.4 Reflection Coefficient Derivation

In this section we derive an expression for the total reflection coefficient, $\rho(r_o)$, due to a single edge in electron density, or a finite number of edges, occurring within the different radar range gates. For that purpose we divide the rocket measured data in segments of length determined by the radar resolution. For example, a 10 km electron density profile would result in 10 of such segments for a radar resolution of $\Delta r = 1$ km. In that way, we can predict the amount of backscattered, or received, power as a function of altitude, $P_r(r_o)$, produced by PMSE and/or any other type of layered phenomena. The radar received power is directly proportional to the total power reflection coefficient of the medium, $|\rho(r_o)|^2$, as described in Equation 4.27. The radar reflection coefficient as a function of altitude is generally expressed by the integral equation

$$\rho(r_o) = -j(\frac{2\pi r_e}{k}) \int_{-\infty}^{+\infty} N_e(\xi) e^{-(\frac{\xi^2}{4\sigma_r^2})} e^{-2jk\xi} d\xi, \tag{A.12}$$

where $\xi = (z - r_o)$ is the distance from the center of the range gate, and $N_e(\xi)$ is a function describing the dependency of electron density in space. r_e, k, and σ_r, are the classical electron radius, radar wavenumber, and the second moment of the range weighting function, respectively [Doviak and Zrnic, 1984]. We can parameterize the rocket electron density data, $N_e(\xi)$, using Wavelet basis functions, i.e., Canny functions, by means of the reconstruction formula

$$N_e(\xi) = \sum_{b=1}^{N} \sum_{i=1}^{M} A_i \psi_{i,b}(\xi), \tag{A.13}$$

where A_i are coefficients obtained from the Wavelet transform and $\psi_{i,b}$ are the appropriate Canny functions [Alcala et al., 2001b]. The summation over i represents the dilation in wavelet scale size, and the summation over b represents a translation in space or altitude. The Canny function, the first derivative of a Gaussian

function, is given by

$$\psi_{i,b} = -\pi^{-1/4}\sqrt{2^{(1-i)}}(\frac{\xi - \xi_b}{L_i})e^{-(\xi-\xi_b)^2/2L_i^2}, \tag{A.14}$$

where ξ_b is the offset of the wavelet basis function from the center of the range window, $L_i = 2^i\Delta x$ is the wavelet scale size, and Δx is the instrument sampling distance. Substituting Equations A.13 and A.14 in A.12, we obtain

$$\rho(r_o) = j\pi^{-1/4}(\frac{2\pi r_e}{k})\sum_{b=1}^{N}\sum_{i=1}^{M}(\frac{A_i}{L_i})\sqrt{2^{(1-i)}}e^{-\xi_b^2/2L_i^2}\int_{-\infty}^{+\infty}(\xi - \xi_b)e^{-(a\xi^2+2b\xi)}d\xi \tag{A.15}$$

where $a = \frac{1}{2L_i^2} + \frac{1}{4\sigma_r^2}$ and $b = \frac{-\xi_b}{L_i} + 2jk$. We can separate the integrand of Equation A.15 into two functions involving exponentials, one multiplied by ξ and the other by ξ_b, and apply the integral equation: $\int_{-\infty}^{+\infty} e^{-(ax^2+2bx)}dx = -\sqrt{\frac{\pi}{a}e^{b^2/a}}$, to obtain the following expression

$$\rho(r_o) = j\pi^{1/4}(\frac{4\pi r_e}{k})\sum_{b=1}^{N}\sum_{i=1}^{M}A_i\sqrt{\frac{\beta_i}{2^i}}[(1-\beta_i)\xi_b + 2j\beta_i(kL_i^2)] \times E, \tag{A.16}$$

where

$$E = e^{-(1-\beta_i)(\xi_b^2/2L_i^2)}e^{-2\beta_i(kL_i)^2}e^{-2j\beta_i(k\xi_b)} \tag{A.17}$$

and

$$\beta_i = \frac{4\sigma_r^2}{4\sigma_r^2 + 2L_i^2}. \tag{A.18}$$

β_i represents the effect of the range weighting function to the radar scattering. Figure A.11 illustrates the dependency of the power reflection coefficient, square of Equation A.16, on normalized scale size, L_i/λ, for a single edge of electron density centered at the radar range window, $\xi_b = 0$. Notice how the power reflection coefficient maximizes for $L_i/\lambda \sim 0.1125$. For all the frequencies considered in our work, the most significant scale size contributing to radio backscatter is much smaller than the extent of the range resolution, allowing us to assume $\beta_i \to 1$. As

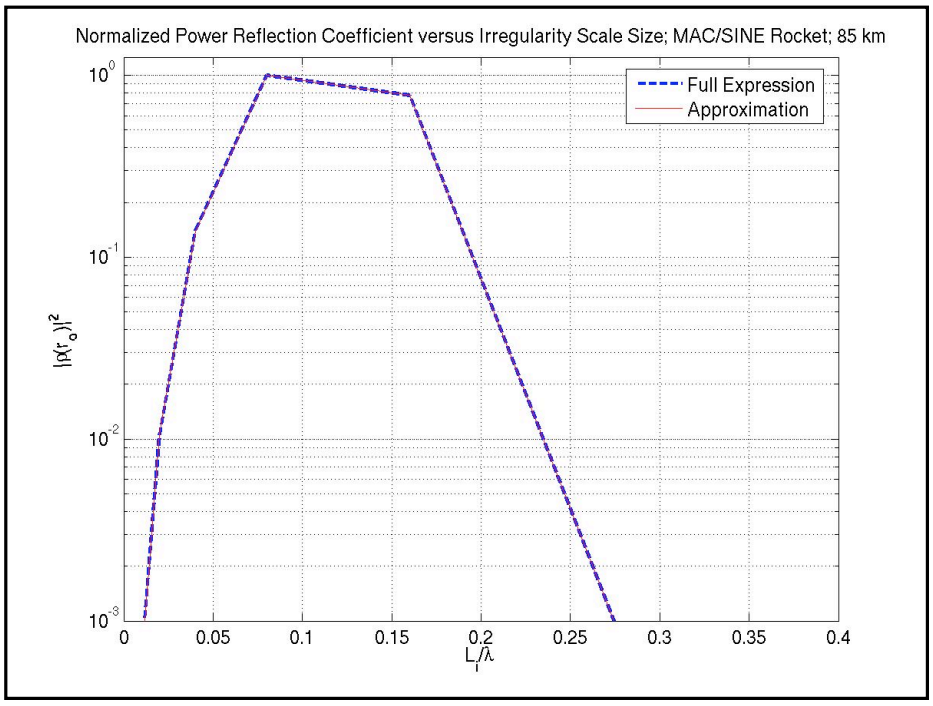

Figure A.11: Normalized power reflection coefficient as a function of scale size for an edge of electron density centered at the radar range window. λ is the radar Bragg length.

an example, for a 5 MHz (HF) radar system with pulse width $\tau = 10\ \mu s$, the most important scale size contributing to radio scatter is $L_i = 0.1125\lambda = 3.375$ m and $\sigma_r = 0.35(\frac{c\tau}{2}) = 525$ m. The final expression for the reflection coefficient is

$$\rho_b(r_o) = -\pi^{-1/4}(8\pi r_e)\sum_{i=1}^{M}\frac{A_i L_i^2}{\sqrt{2^i}}e^{-2(kL_i)^2}. \tag{A.19}$$

In the above expression, we have skipped the phase term of the form e^{-2jx}.

Table A.9: DYANA Rocket Analyzed Data

Range Center (km)	Wavelet Scalogram	Reflectivity Plot
81	X	X
82	X	X
83	X	X
84	X	X
85	X	X
86	X	X
87	X	X
88	X	X

DYANA: March 11, 1990, 2042 UT at Norway.

A.5 Rocket Wavelet Analyses

In this section we show plots of complete wavelet analyses performed on DYANA and MAC/SINE rocket measurements of electron density. Tables A.9 and A.10 summarize the analyzed data segments for each rocket flight. Each set of 2-plots consists of a 1 km electron density data segment (top panel) accompanied by its corresponding wavelet scalogram and/or signal energy distribution as a function of space (x-axis, km) and scale size (y-axis, m). The wavelet coefficients, displayed as 2-dimensional images, were normalized to the scale size, or row, maxima in order to facilitate the data visualization. We use the de-normalized wavelet coefficients, corresponding to edges in space, to reconstruct the profile contributing to specular reflections in the radar signal.

Table A.10: MAC/SINE Rocket Analyzed Data

Range Center (km)	Wavelet Scalogram	Reflectivity Plot
81	X	X
82	X	X
83	X	X
84	X	X
85	X	X
86	X	X
87	X	X
88	X	X

MAC/SINE: July 14, 1987; 0929 UT at Norway.

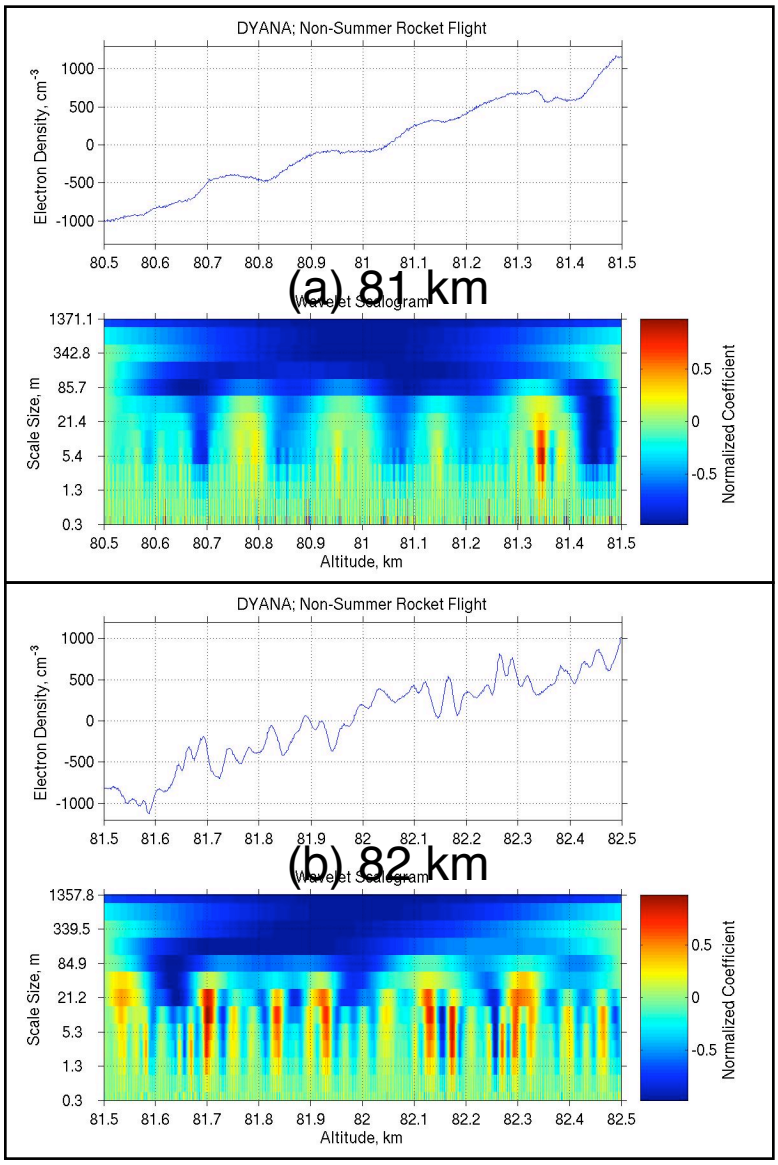

Figure A.12: DYANA Electron Density and Wavelet Scalogram: (a) 81 km, (b) 82 km

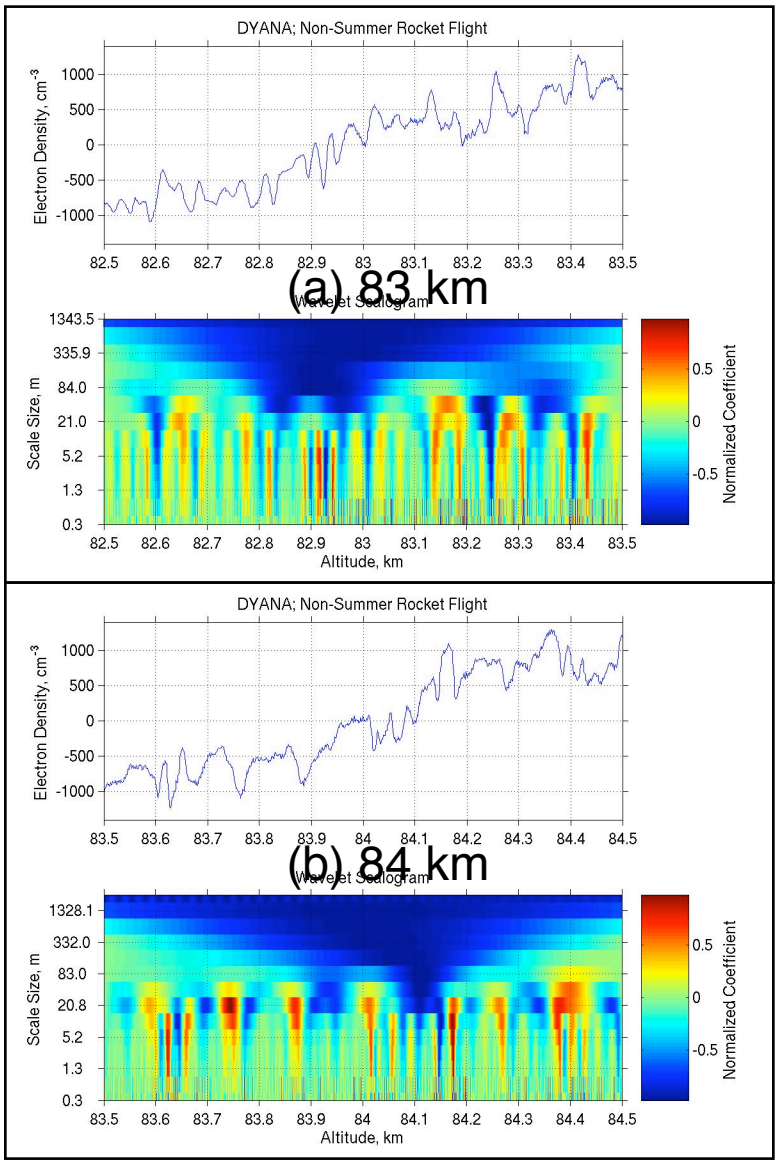

Figure A.13: DYANA Electron Density and Wavelet Scalogram: (a) 83 km, (b) 84 km

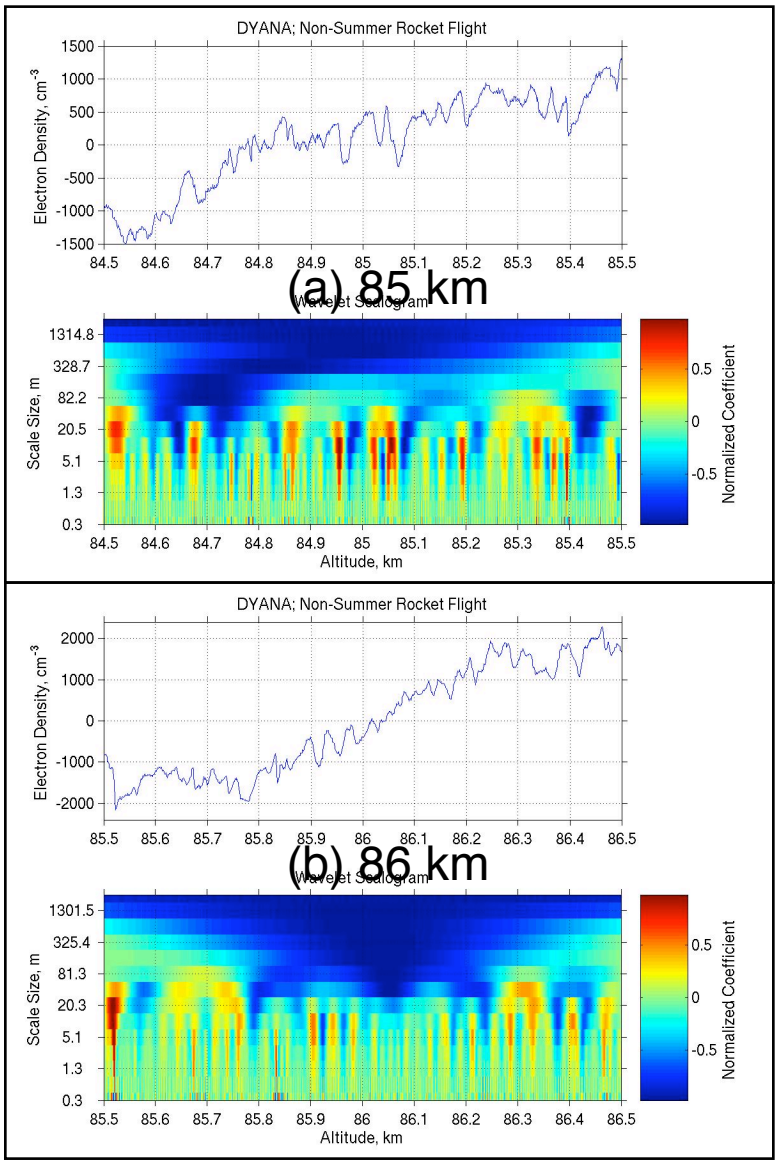

Figure A.14: DYANA Electron Density and Wavelet Scalogram: (a) 85 km, (b) 86 km

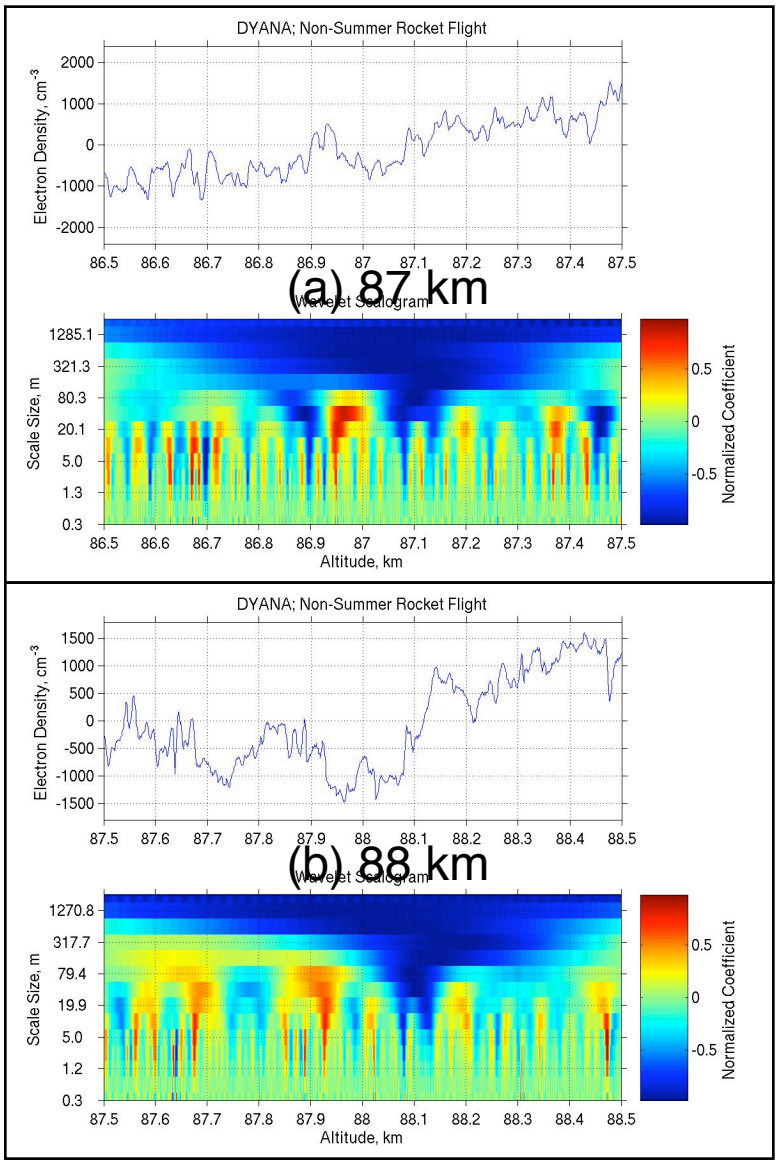

Figure A.15: DYANA Electron Density and Wavelet Scalogram: (a) 87 km, (b) 88 km

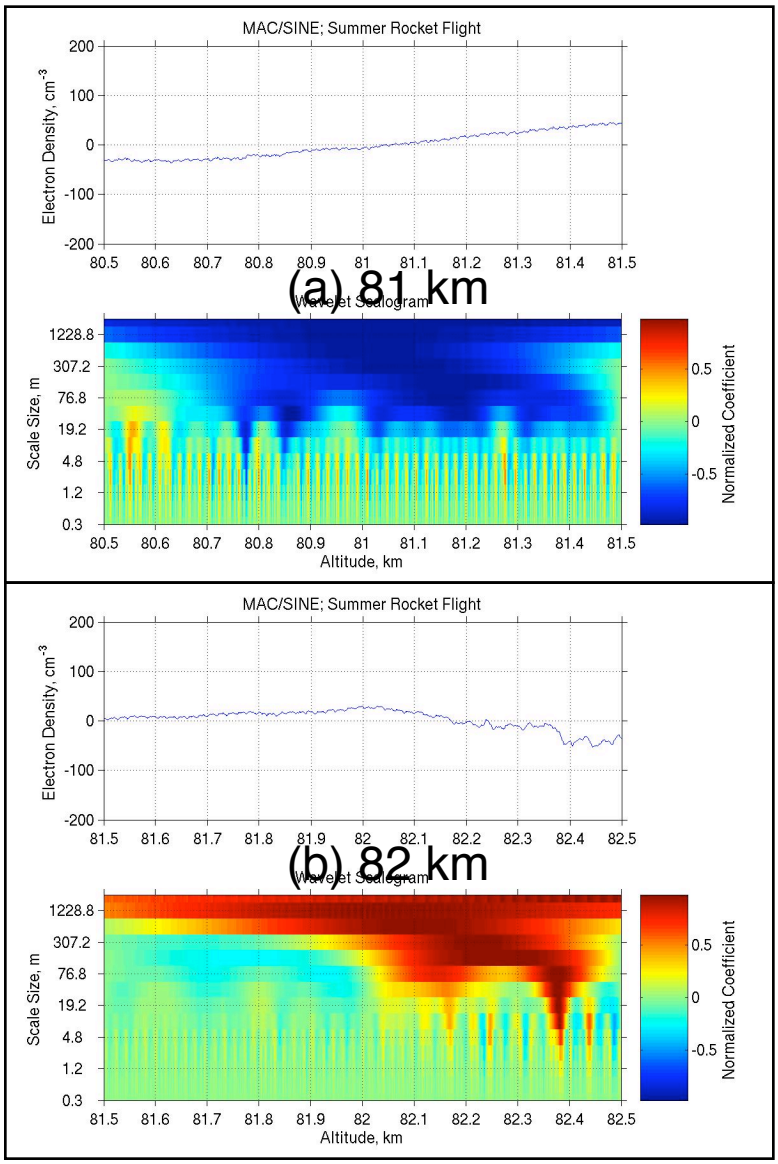

Figure A.16: MAC/SINE Electron Density and Wavelet Scalogram: (a) 81 km, (b) 82 km

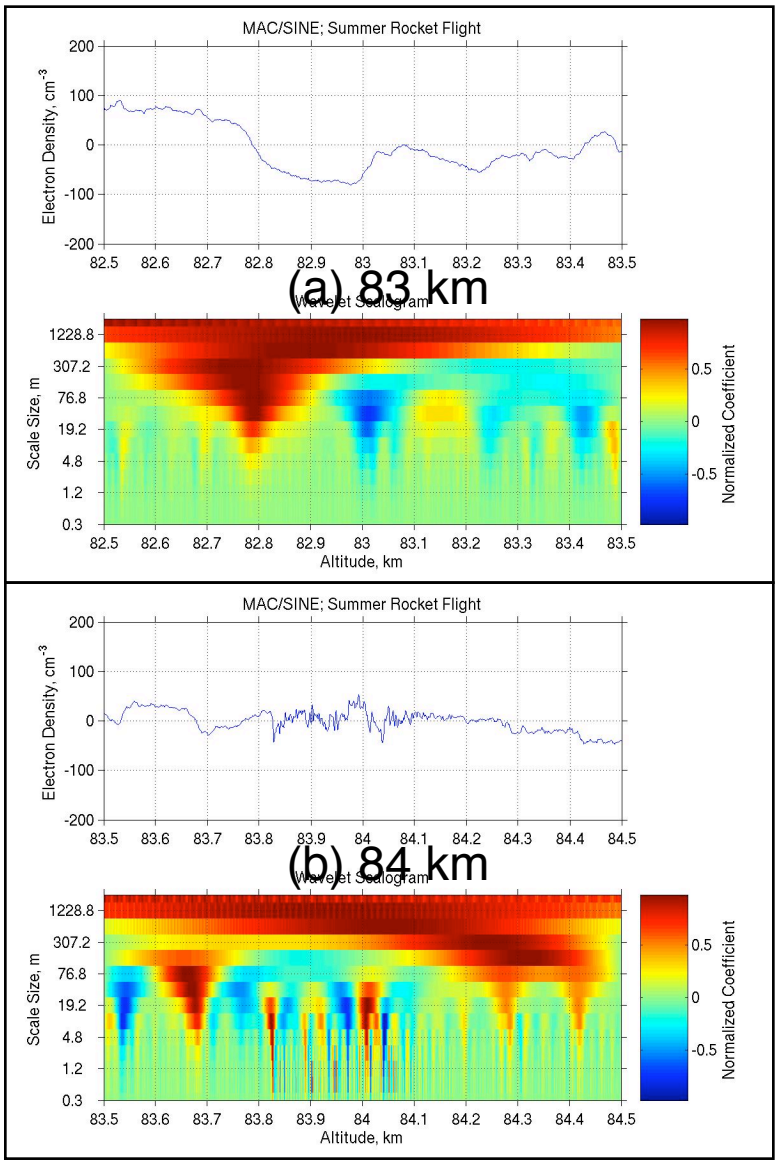

Figure A.17: MAC/SINE Electron Density and Wavelet Scalogram: (a) 83 km, (b) 84 km

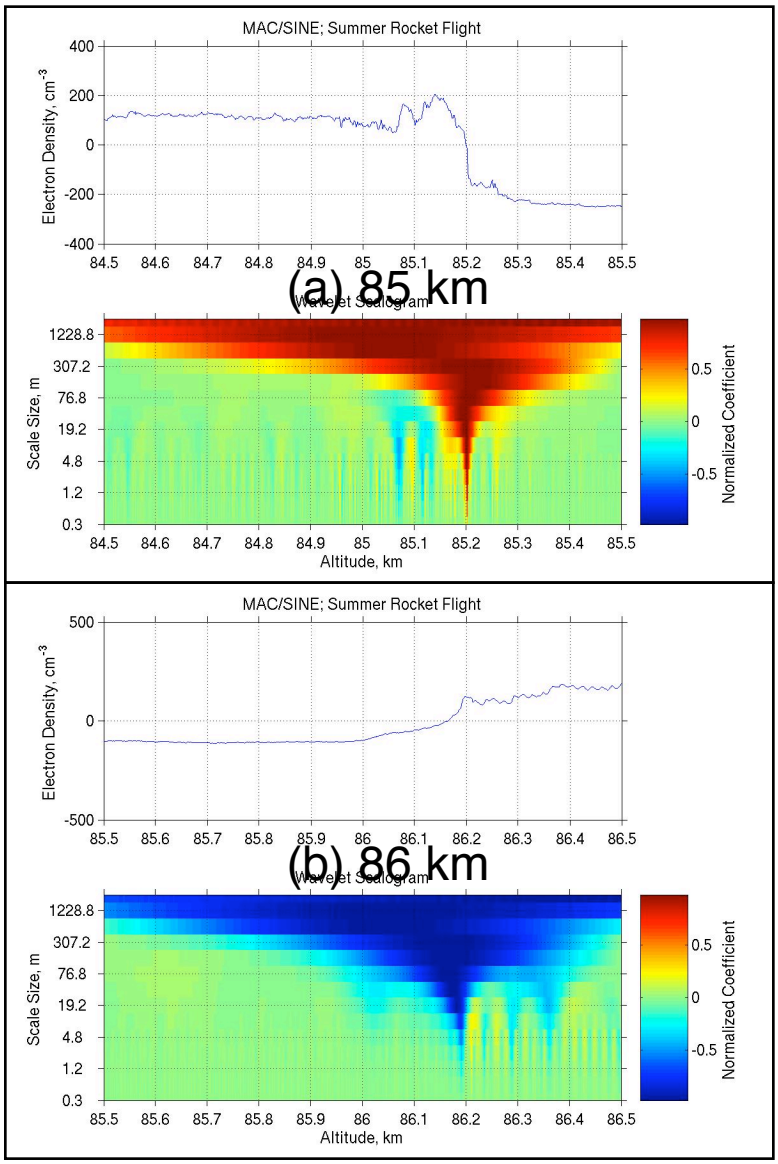

Figure A.18: MAC/SINE Electron Density and Wavelet Scalogram: (a) 85 km, (b) 86 km

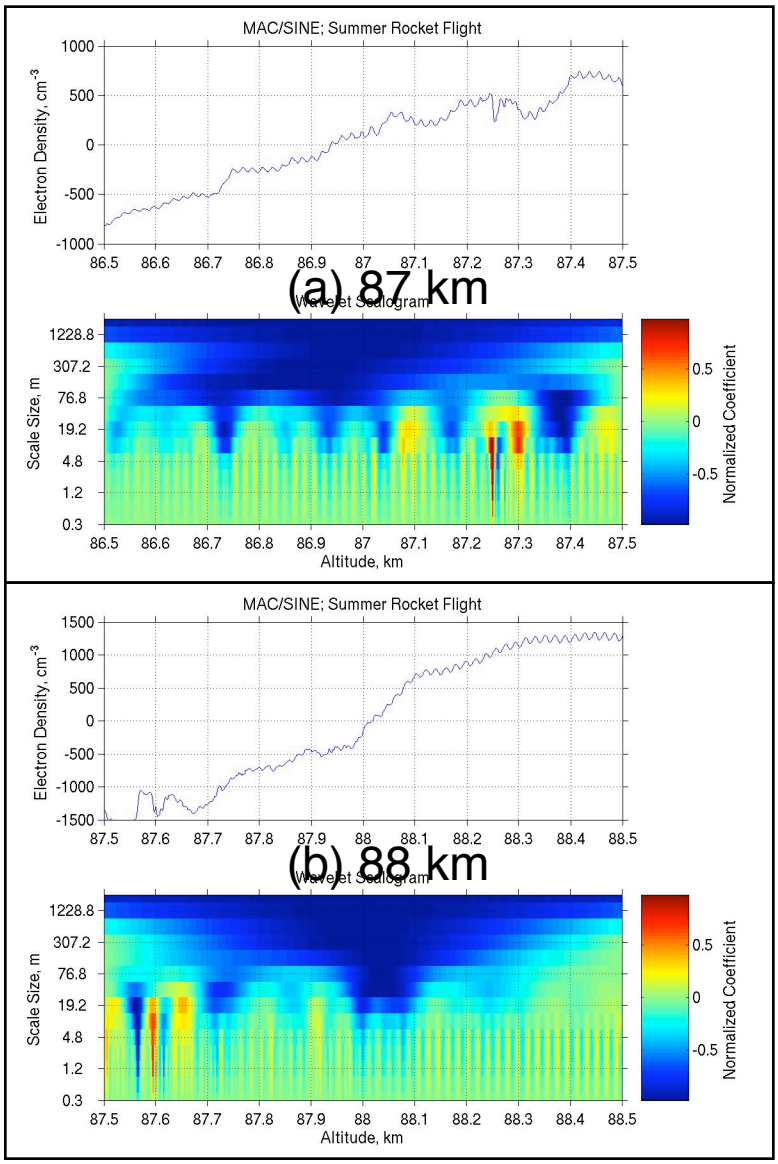

Figure A.19: MAC/SINE Electron Density and Wavelet Scalogram: (a) 87 km, (b) 88 km

A.6 Radar Reflectivity Estimates

Figures A.20 to A.27 show a complete set of plots of radar reflectivity (m^{-1}) versus wavenumber (rad/m) derived from the DYANA (summer) and MAC/SINE (winter) rocket flights. Each plot displays the results obtained from an analyzed 1 km segment of electron density between 80 and 90 km. The contributions for turbulent and edge scattering mechanisms are plotted separately, in addition to the Driscoll and Kennedy scattering model for S_c=1 (winter) and S_c=100 (summer). Both signal components were found using the scattering formulas derived in Chapter 4.

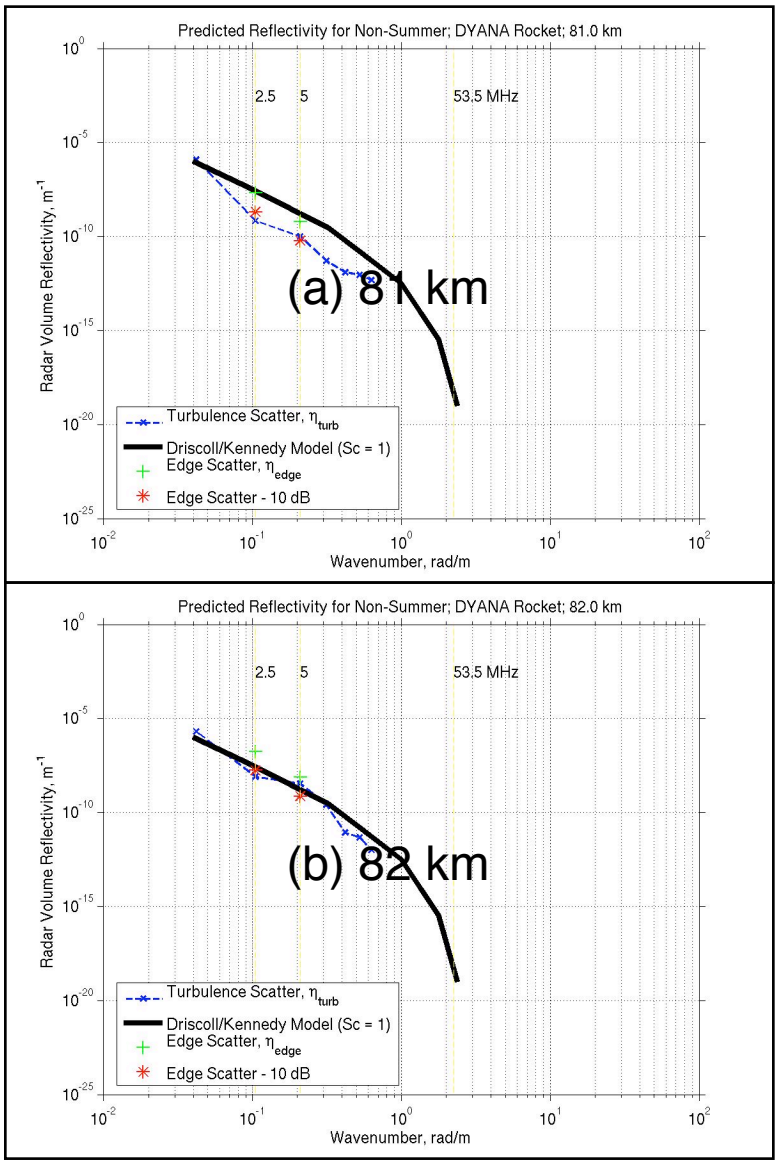

Figure A.20: Radar reflectivity versus wavenumber for DYANA: (a) 81 km, (b) 82 km

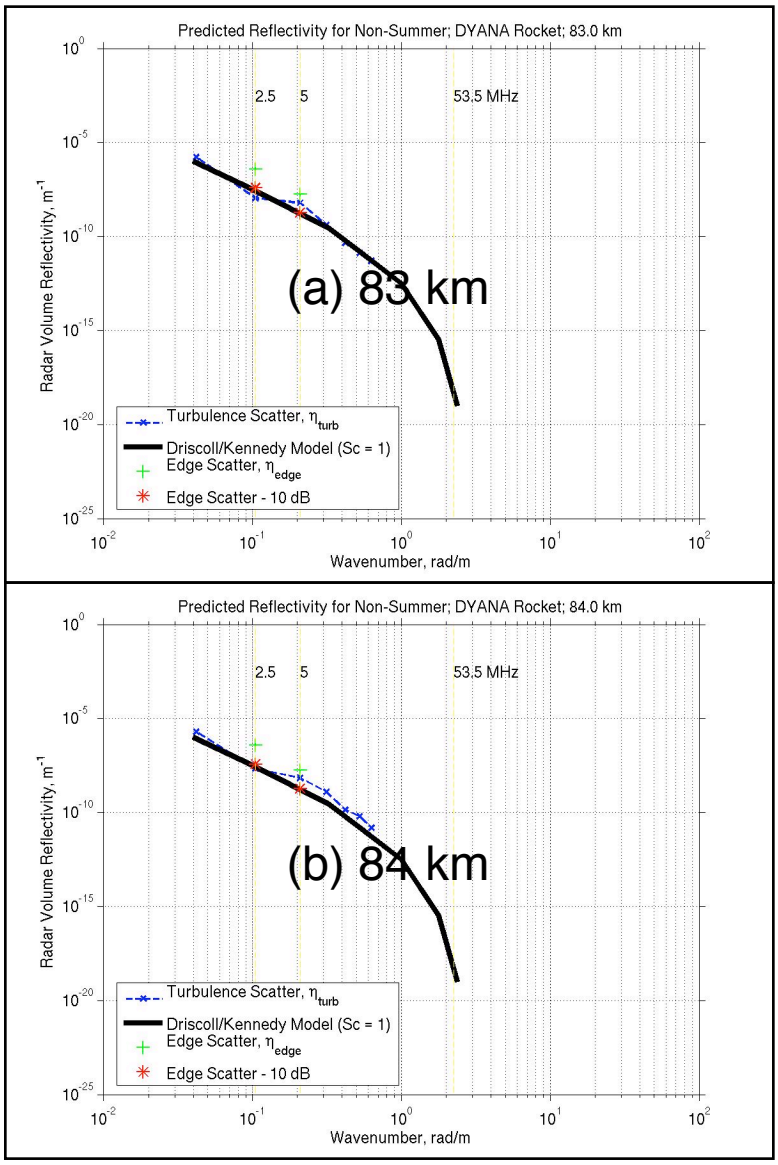

Figure A.21: Radar reflectivity versus wavenumber for DYANA: (a) 83 km, (b) 84 km

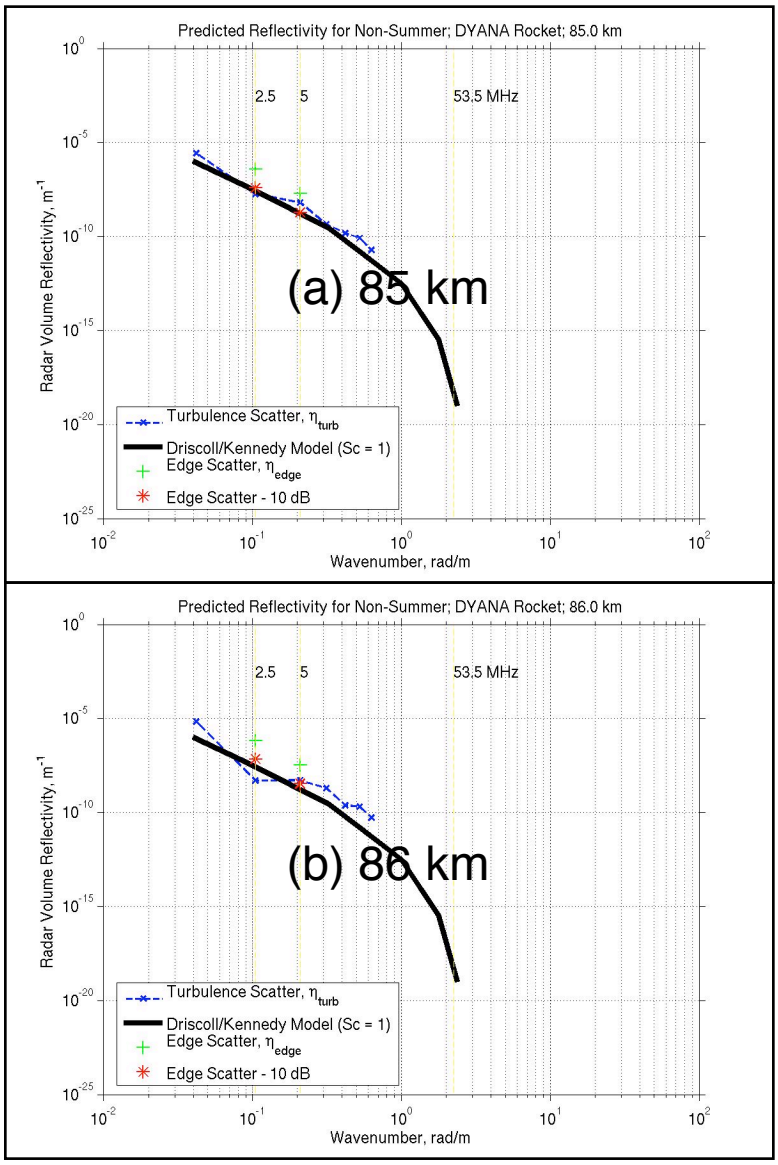

Figure A.22: Radar reflectivity versus wavenumber for DYANA: (a) 85 km, (b) 86 km

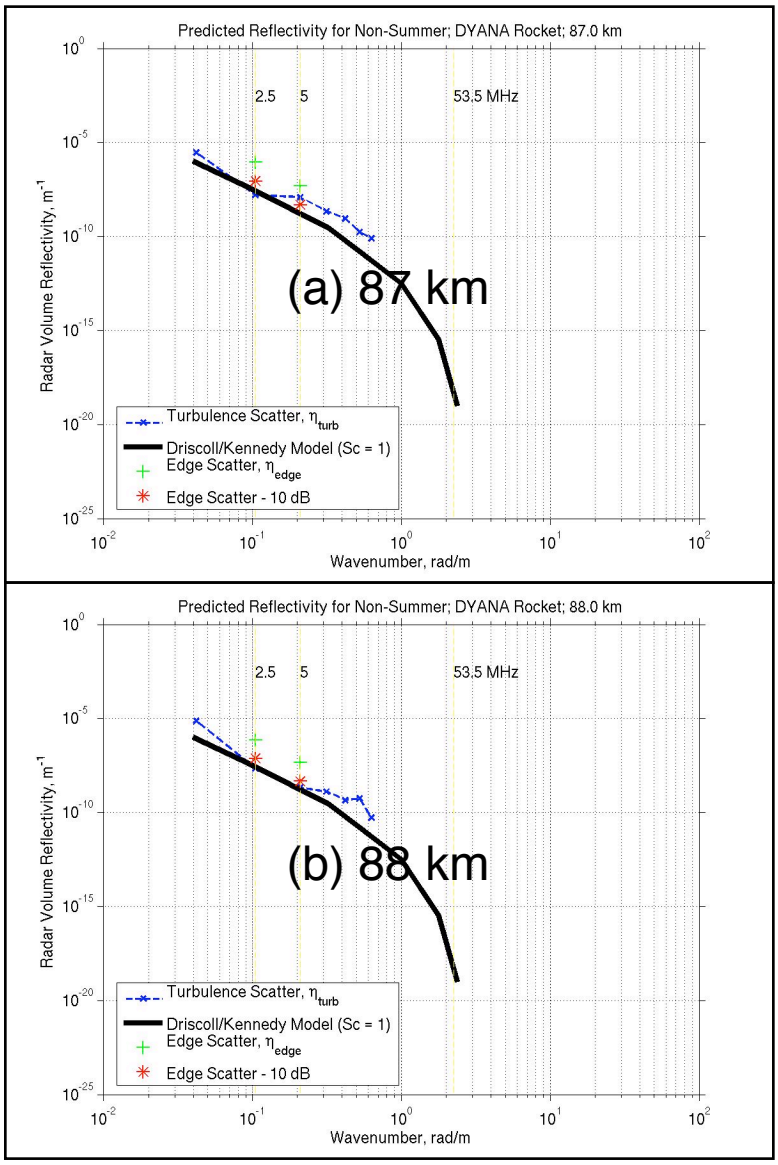

Figure A.23: Radar reflectivity versus wavenumber for DYANA: (a) 87 km, (b) 88 km

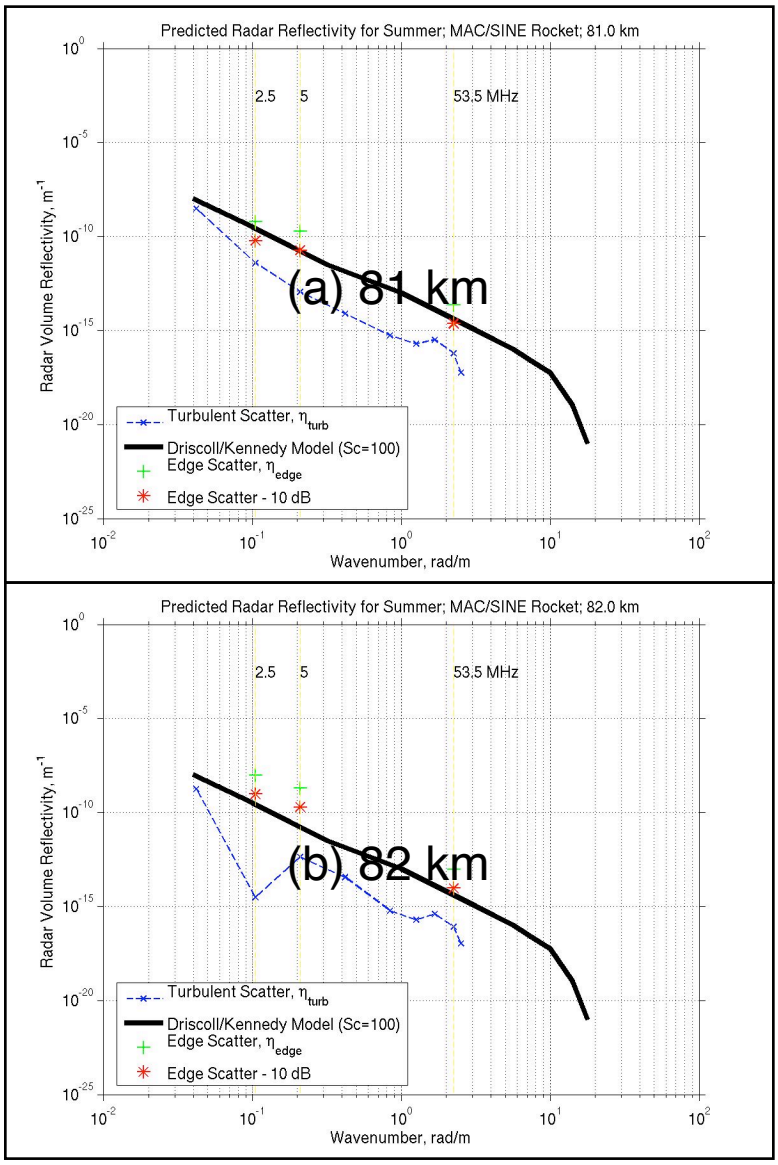

Figure A.24: Radar reflectivity versus wavenumber for MAC/SINE: (a) 81 km, (b) 82 km

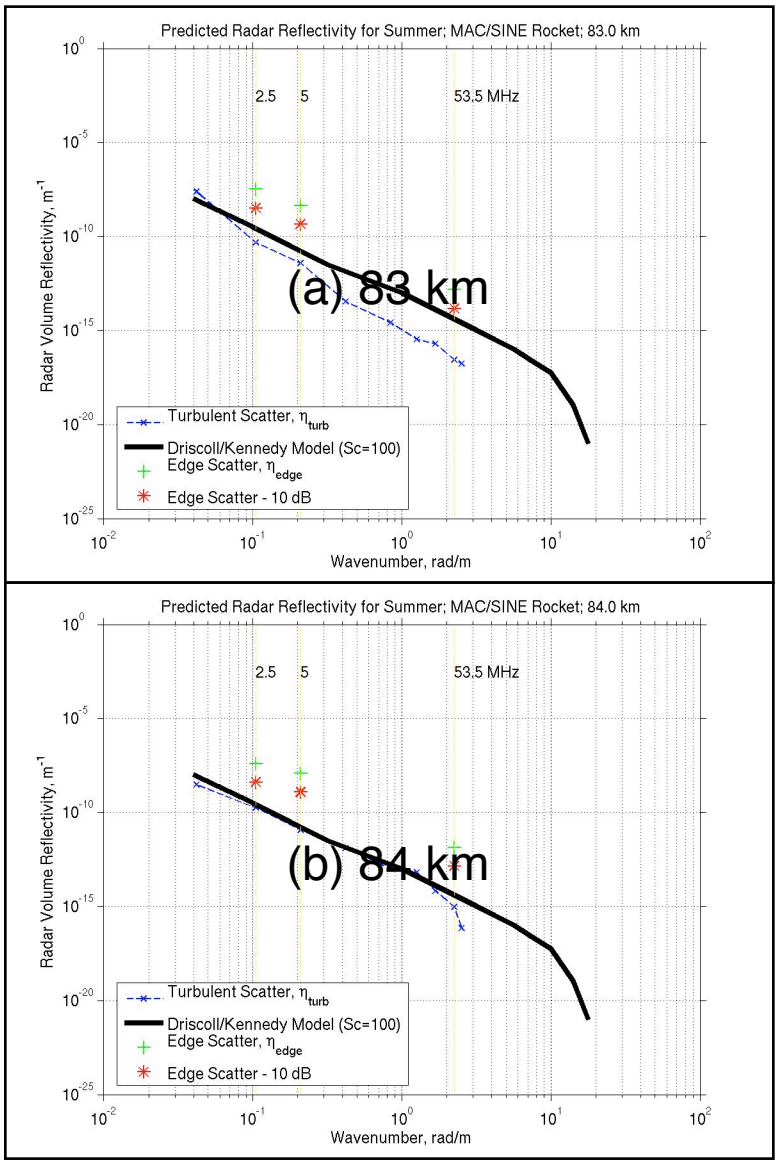

Figure A.25: Radar reflectivity versus wavenumber for MAC/SINE: (a) 83 km, (b) 84 km

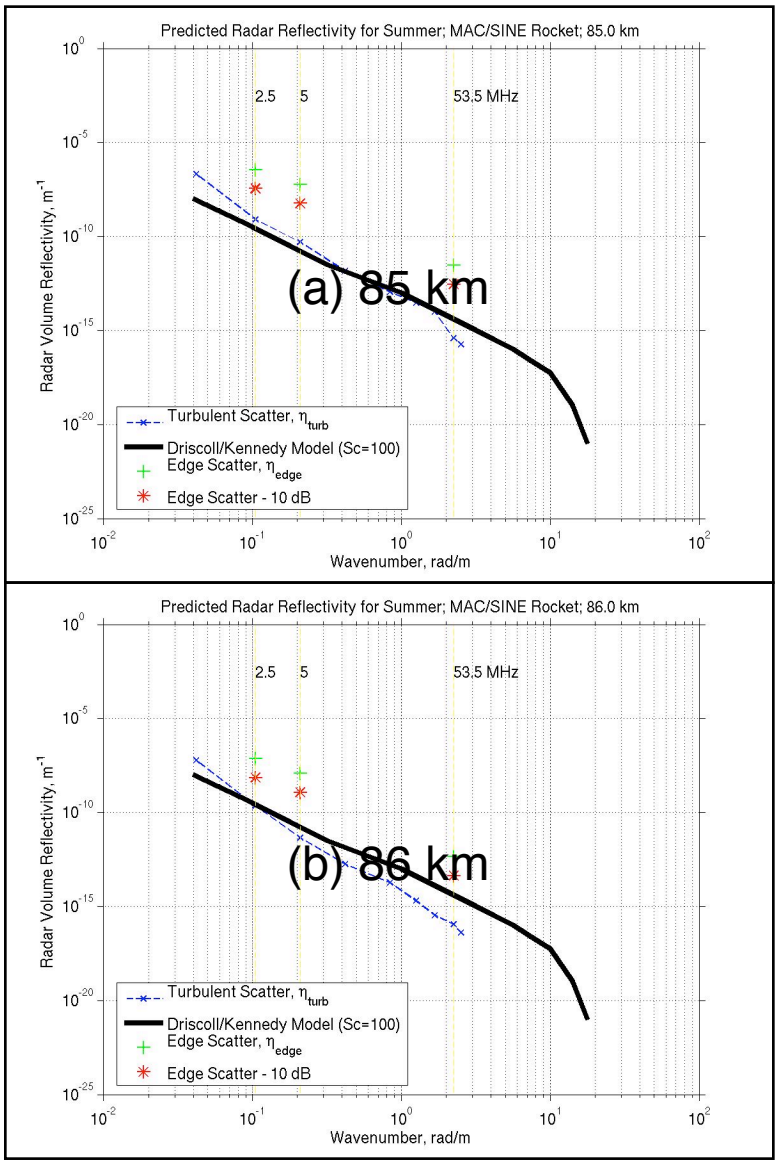

Figure A.26: Radar reflectivity versus wavenumber for MAC/SINE: (a) 85 km, (b) 86 km

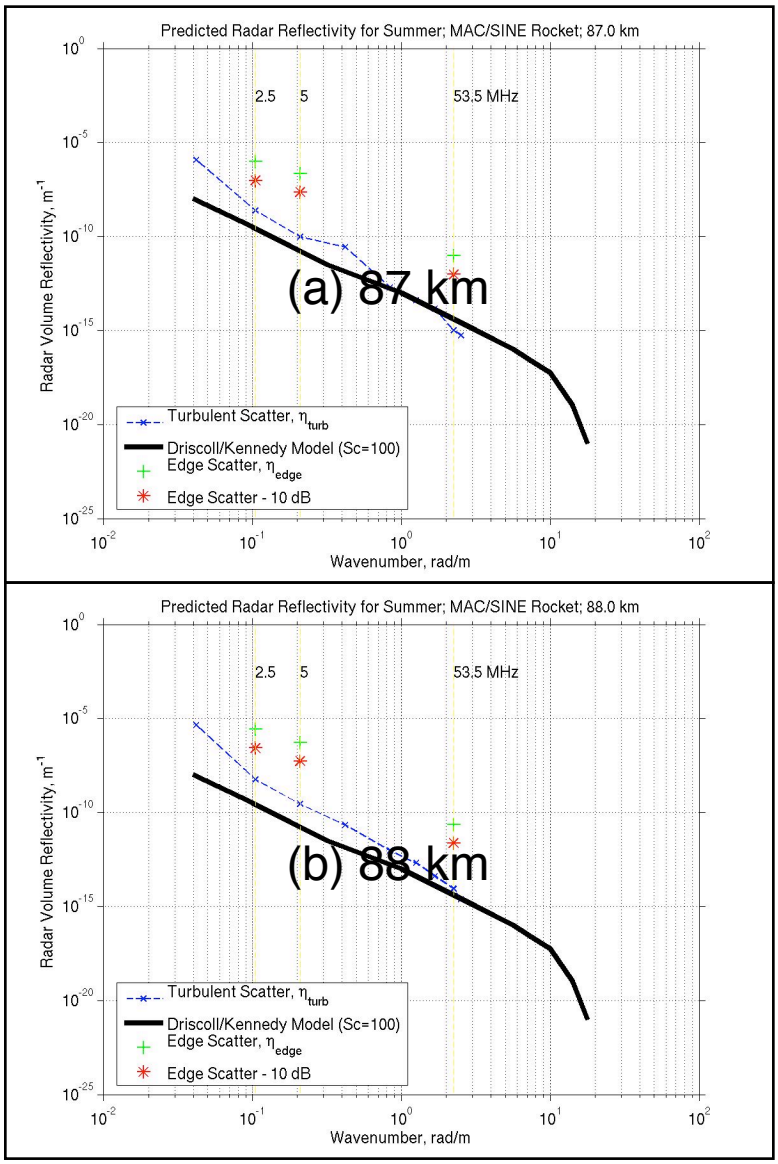

Figure A.27: Radar reflectivity versus wavenumber for MAC/SINE: (a) 87 km, (b) 88 km

BIBLIOGRAPHY

[Alcala et al., 2001a] Alcala, C. M., Kelley, M. C., and J. C. Ulwick, Nonturbulent layers in the polar summer mesosphere, 1. Detection of sharp gradients using wavelet analysis, *Radio Sci., 36,* 891-903, 2001a.

[Alcala et al., 2001b] Alcala, C. M., Kelley, M. C., and J. C. Ulwick, Nonturbulent layers in the polar summer mesosphere, 2. Appication of wavelet analysis to VHF scattering, *Radio Sci., 36,* 875-890, 2001b.

[Amos, 2006] Amos, J., Mission to target highest clouds, *BBC News*, 2006.

[Backhouse, 1885] Backhouse, T. W., The luminous cirrus cloud of June and July, *Meteorol. Mag., 20,*, 133, 1885.

[Balsley et al., 1983] Balsley, B. B., Ecklund W. L., and D. C. Fritts, VHF Echoes from the High-Latitude Mesosphere and Lower Thermosphere: Observations and Interpretations, *J. Atm. Sci., 40, 10,* 2451-2466, 1983.

[Balsley et al., 1993] Balsley, B. B., Woodman R. F., Sarango M., Urbina J., Rodriguez R., Ragaini E., and J. Carey, Southern-hemisphere PMSE: Where are they?, *Geophys. Res. Lett., 20,* 1983-1985, 1993.

[Balsley et al., 1995] Balsley, B. B., Woodman R. F., Sarango M., Rodriguez R., Urbina J., Ragaini E., Carey J., Huaman M., and A. Giraldez, On the lack of southern hemisphere polar mesosphere summer echoes, *J. Geophys. Res., 100,* 11,685-11,693, 1995.

[Batchelor, 1959] Batchelor, G. K., Small-scale variation of convected quantities like temperature in a turbulent fluid, 1, *J. Fluid Mech., 5,* 113, 1959.

[Bean and Dutton, 1968] Bean, B. R., and E. J. Dutton, *Radio Meteorology,* Dover, New York, 435 pp., 1968.

[Blix, 1988] Blix, T. A., In-situ studies of turbulence in the middle atmosphere by means of electrostatic ion probes, *NDRE/PUBL-88/1002,* Norw. Def. Res. Estab., Kjeller, 1988.

[Bremer et al., 1996] Bremer, J., Hoffmann P., Manson A., Meek C., Rűster R., and W. Singer, PMSE observations at three different frequencies in northern Europe during summer 1994, *Ann. Geophys., 14,* 1317-1327, 1996.

[Briggs and Vincent, 1973] Briggs, B. H., and R. A. Vincent, Some theoretical considerations on remote probing of weakly scattering irregularities, *Aust. J. Phys., 26,* 805-814, 1973.

[Canny, 1986] Canny, J., A computational approach to edge detection, *IEEE Trans. Pattern Anal. Mach. Intel., 8,* 679-698, 1986.

[Chen et al., 2001] Chen, C. Y., Kelley, M. C., and D. L. Walters, Wavelet analysis of high-resolution temperature data with applications to radio wave scattering, *Radio Sci., 36,* 905-926, 2001.

[Chilson et al., 2000] Chilson, P. B., Belova E., Rietveld, M., Kirkwood S., and U.-P. Hoppe, First artificially induced modulation of PMSE using the EISCAT heating facility, *Geophys. Res. Lett., 27,* 3801-3804, 2000.

[Cho et al., 1992a] Cho, J. Y. N., Kelley M. C., and C. J. Heinselman, Enhancement of Thomson scatter by charged aerosols in the polar mesosphere: Measurements with a 1.29-GHz radar, *Geophys. Res. Lett., 19,* 1097, 1992.

[Cho et al., 1992b] Cho, J. Y. N., Hall T. M., and M. C. Kelley, On the role of charged aerosols in polar mesosphere summer echoes, *J. Geophys. Res., 97,* 875, 1992b.

[Cho and Kelley, 1993] Cho, J. Y. N., and M. C. Kelley, Polar mesosphere summer radar echoes: Observations and current theories, *Rev. Geophys., 31,* 243-265, 1993.

[Cho et al., 1993] Cho, J. Y. N., Swartz W. E., Kelley M. C., and C. A. Miller, CUPRI observations of PMSE during Salvo B of NLC-92: Evidence of both partial reflection and turbulent scatter, *Geophys. Res. Lett., 20,* 2291-2294, 1993.

[Cho and Röttger, 1997] Cho, J. Y. N., and J. Röttger, An updated review of polar mesosphere summer echoes: Observation, theory, and their relationship to noctilucent clouds and subvisible aerosols, *J. Geophys. Res., 102,* 2001-2020, 1997.

[Collis et al., 1994] Collis, P. N., Rietveld, M. T., and A. P. van Eyken, Dual-beam observations by the EISCAT radars during PMSE conditions, *Adv. Space Res., 14(9),* 149-152, 1994.

[Collins et al., 2003] Collins, R. L., Kelley M. C., Nicolls M., Ramos C., Hou T., Stern T., Mizutani K., and T. Itabe, Simultaneous lidar observations of a noctilucent cloud and an internal wave in the polar mesosphere, *J. Geophys. Res., 108(D8),* 8435-8442, 2003.

[Craig, 2002] Craig, K. H., *Propagation of Radiowaves,* Institution of Engineering and Technology, UK, L. W. Barclay (Ed), 456 pp., 2002.

[Czechowsky et al., 1988] Czechowsky, P., Reid I. M., and Rüster R., VHF radar measurements of the aspect sensitivity of the summer polar mesopause echoes over Andenes (69degN, 16degE), Norway *J. Geophys. Res., 15,* 1259, 1988.

[Czechowsky et al., 1989] Czechowsky, P., Reid I. M., Rüster R., and G. Schmidt, VHF radar echoes observed in the summer and winter polar mesosphere over Andoya, Norway, *J. Geophys. Res., 94,* 5199, 1989.

[Doviak and Zrnic, 1984] Doviak, R. J., and D. S. Zrnic, Reflection and scatter formula for anisotropically turbulent air, *Radio Sci., 19,* 325-336, 1984.

[Ecklund and Balsley, 1981] Ecklund, W. L., and B. B. Balsley, Long-term observations of the Arctic mesosphere with the MST radar at Poker Flat, Alaska, *J. Geophys. Res., 86,* 7775-7780, 1981.

[Fritts et al., 1988] Fritts, D. C., Smith S. A., Balsley B. B., and C. R. Philbrick, Evidence of gravity wave saturation and local turbulence production in the summer mesosphere and lower thermosphere during the STATE experiment, *J. Geophys. Res., 93,* 7015-7025, 1988.

[Gadsden, 1990] Gadsden, M., A secular change in noctilucent cloud occurrence, *J. Atmos. Terr. Phys., 52,* 247-251, 1990.

[Gage and Green, 1978] Gage, K. S., and J. L. Green, Evidence for specular reflection from monostatic VHF radar observations of the stratosphere, *Radio Sci., 13,* 991-1001.

[Gage and Balsley, 1980] Gage, K. S., and B. B. Balsley, On the scattering and reflection mechanisms contributing to clear air radar echoes from the troposphere, stratosphere, and mesosphere, *Radio Sci., 15,* 243-257, 1980.

[Gage et al., 1981] Gage, K. S., Balsley B. B., and J. L. Green, Fresnel scattering model for the specular echoes observed by VHF radar, *Radio Sci., 16,* 1447-1453, 1981.

[Gelinas et al., 1998] Gelinas, L. J., Lynch, K. A., Kelley, M. C., Collins, S., Baker, S., Zhou, Q., and J. S. Friedman, First observation of meteoritic charged dust in the tropical mesosphere, *Geophys. Res. Lett., 25,* 40474050, 1998.

[Gelinas et al., 2005] Gelinas, L. J., Lynch, K. A., Kelley, M. C., Collins, R. L., Widholm, M., MacDonald, E., Ulwick, J., and P. Mace, Mesospheric charged dust layer: Implications for neutral chemistry, *J. Geophys. Res., 110,*, A01310, 2005.

[Hall, 1991] Hall, T. M., Radar observations and dynamics of the polar summer mesosphere, Ph.D. thesis, Cornell Univ., Ithaca, N.Y., 1991.

[Hargreaves, 1992] Hargreaves, J. K, *The Solar Terrestrial Environment*, Cambridge University Press, 1992.

[Havnes et al., 1990] Havnes, O., de Angelis U., Bingham C. K., Goertz C. K., Morfill G. E., and V. Tsytovich, On the role of dust in the summer mesopause, *J. Atmos. Terr. Phys., 52,* 637, 1990.

[Havnes et al., 2001] Havnes, O., Brattli A., Aslaksen T., Singer W., Latteck R., Blix T., Thrane E., and J. Trϕim, First common volume observations of layered plasma structures and polar mesospheric summer echoes by rocket and radar, *Geophys. Res. Lett., 28,* 8, 14191422, 2001.

[Havnes et al., 2003] Havnes, O., La Hoz C., Naesheim L., and M. Rietveld, First observations of the PMSE overshoot effect and its use for investigating the conditions in the summer mesosphere, *Geophys. Res. Letter, 30 (23),* 2229, 2003.

[Hocking and Vincent, 1982] Hocking, W. K., and R. A. Vincent, Comparative observations of D region HF partial reflections at 2 and 6 MHz, *J. Geophys. Res., 87,* 7615-7624, 1982.

[Hocking and Röttger, 1983] Hocking, W. K., and J. Röttger, Pulse length dependence of radar signal strength for Fresnel backscatter, *Radio Sci., 18,* 1312-1324, 1983.

[Hocking, 1985] Hocking, W. K., Measurement of turbulent energy dissipation rates in the middle atmosphere by radar techniques: A review, *Radio Sci., 20,* 6, 1403-1422, 1985.

[Hocking, 1986] Hocking, W. K., Observation and measurement of turbulence in the middle atmosphere with a VHF radar, *J. Atmos. Terr. Phys., 48,* 655-670, 1986.

[Hocking, 1987] Hocking, W. K., Radar studies of small-scale structure in the upper and middle atmosphere and lower ionosphere, *Adv. Space Res., 7,* 327-338, 1987.

[Hocking et al., 1990] Hocking, W. K., Fukao S., Tsuda T., Yamamoto M., Sato T., and S. Kato, Aspect sensitivity of stratospheric VHF radio wave scatterers, particularly above 15 km altitude, *Radio Sci., 25,* 4, 613-627, 1990.

[Hocking, 2002] Hocking, W. K., What the Radar sees, *Third International School on Atmospheric Radar/ICTP*, Trieste, Italy, 2002.

[Hocking, 2003] Hocking, W. K., Evidence for viscosity, thermal conduction and diffusion waves in the Earth's atmosphere, *Review of Scientific Instruments, 74(1),* 420-426, 2003.

[Holton, 1983] Holton, J. R., The influence of gravity wave breaking on the general circulation of the middle atmosphere, *J. Atmos. Sci., 40,* 40, 2497, 1983.

[Hoppe et al., 1988] Hoppe, U.-P., Hall C., and J. Röttger, First observations of summer polar mesospheric backscatter with a 224-MHz radar, *Geophys. Res. Lett., 15,* 28, 1988.

[Huaman, 1998] Huaman, M., *Polar Mesosphere Summer Echoes (PMSE): Some factors related to their occurrence and possible causes for inter-hemispheric differences,* Ph.D thesis, University of Colorado, Boulder, CO., 1998.

[Hunten et al., 1980] Hunten, D. M., Turco R. P., and O. B. Toon, Smoke and dust particles of meteoric origin in the mesosphere and stratosphere, *J. Atmos. Sci., 37,* 1342-1357, 1980.

[Inhester et al., 1990] Inhester, B., Ulwick J., Cho J., Kelley M. C., and G. Schmidt, Consistency of rocket and radar electron density observations: Implications about the anisotropy of mesospheric turbulence, *J. Atmos. Terr. Phys., 52,* 855-873, 1990.

[Jesse, 1887] Jesse, O., Die Höhe der leuchtenden (silbernen) Wolken, *Meteorol. Z., 4,* 424, 1887.

[Karashtin et al., 1997] Karashtin, A. N., Shlyugaev Y.V., Abramov V.I., Belov I.F., Berezin I.V., Bychkov V.V., Eryshev E.B., and G.P. Komrakov, First HF radar measurements of summer mesopause echoes at SURA, *Ann. Geophys., 15,* 935-941, 1997.

[Kelley et al., 1987] Kelley, M. C., Farley D., and J. Röttger, The effect of cluster ions on anomalous VHF backscatter from the summer polar mesosphere, *Geophys. Res. Lett., 14,* 1031-1034, 1987.

[Kelley and Ulwick, 1988] Kelley, M., and J. Ulwick, Large- and small-scale organization of electrons in the high-latitude mesosphere: Implications of the STATE data, *J. Geophys. Res., 93,* 7001-7008, 1988.

[Kelley et al., 1990] Kelley M. C., Ulwick J. C., Röttger J., Inhester B., Hall T., and T. Blix, Intense turbulence in the polar mesosphere: Rocket and radar measurements, *J. Atmos. Terr. Phys., 52,* 875, 1990.

[Kelley et al., 2002] Kelley M. C., Huaman M., Chen C. Y., Ramos C., Djuth F. T., and E. Kennedy, Polar mesosphere summer echo observations at HF frequencies using the HAARP Gakona Ionospheric Observatory, *Geophys. Res. Lett., 29,* 1029, 2002.

[Kelley, 2004] Kelley M. C., A new explanation for long duration meteor radar echoes: Persistent charged dust trains, *Radio Sci., 39,* 2015, 2004.

[Kelley, 2006] Kelley, M. C., *The Earth's Ionosphere*, 2nd edition, in press, 2006.

[Kirkwood et al., 1995] Kirkwood, S., Cho J. Y. N., Hall C. M., Hoppe U. -P., Murtagh D. P., Stegman J., Swartz W. E., van Eyken A. P., Wannberg G., and G. Witt, A comparison of PMSE and other ground-based observations during the NLC-91 campaign, *J. Atmos. Terr, Phys., 57,* 35-44, 1995.

[Lübken and von Zahn, 1991] Lübken, F.-J. and U. von Zahn, Thermal structure of the mesopause region at polar latitudes, *J. Geophys. Res., 96*(D11), 20,84120,857, 1991.

[Lübken et al., 1993] Lübken, F.-J., Lehmacher G., Blix T. A., Hoppe U. -P., Thrane E. V., Cho J. Y. N., and W. E. Swartz, First in-situ observations of neutral and plasma density fluctuations within a PMSE layer, *Geophys. Res. Lett., 20,* 2311-2314, 1993.

[Luhmann et al., 1983] Luhmann, J. G., Johnson R. M., Baron M. J., Balsley B. B., and A. C. Riddle, Observations of the high-latitude ionosphere with the Poker Flat MST radar: Analyses using simultaneous Chatanika radar measurements, *J. Geophys. Res., 88,* 10,239, 1983.

[Murayama et al., 2000] Murayama, Y., Igarashi K., Rice D. D., Watkins B. J., Collins R. L., Mizutani K., Saito Y., and S. Kainuma, Medium Frequency Radars in Japan and Alaska for Upper Atmosphere Observations, *IEICE Trans. Commun., E-83-B, 9,* 1996-2003, 2000.

[Offermann, 1994] Offermann, D., The DYANA campaign: a survey, *J. Atmos. Terr. Phys., 56,* 1639-1657, 1994.

[Ogawa et al., 2002] Ogawa, T., Nishitani N., Sato N., Yamagishi H., and A. S. Yukimatu, Upper mesosphere summer echoes detected with the Antartic Syowa HF radar, *Geophys. Res. Lett., 29(7),* 1029, 2002.

[Olivero and Thomas, 1986] Olivero, J. J., and G. E. Thomas, Climatology of polar mesospheric clouds, *J. Atmos. Sci., 43,* 1263, 1986.

[Phillips, 2003] Phillips, T., Strange Clouds, *Science@NASA*, 2003.

[Rapp et al., 2003] Rapp, M., Lübken F. -J., and T. A. Blix, Small scale density variations of electrons and charged particles in the vicinity of polar mesosphere summer echoes, *Atmos. Chem. Phys., 3,* 1399-1407, 2003.

[Rapp and Lübken, 2004] Rapp, M., and F. -J. Lübken, Polar mesosphere summer echoes (PMSE): review of observations and current understanding, *Atmos. Chem. Phys., 4,* 2601-2633, 2004.

[Reid et al., 1988] Reid, I. M., Rüster R., Czechowsky P., and G. Schmidt, VHF radar measurements of momentum flux in the summer polar mesosphere over Andenes (69^{o}N, 16^{o}E), Norway, *Geophys. Res. Lett., 15,*1263, 1988.

[Reid, 1990] Reid, G. C., Ice particles and electron "bite-outs" at the summer polar mesopause, *J. Geophys. Res., 95,* 13,891, 1990.

[Rosinski and Snow, 1961] Rosinski, J., and Snow R. H., Secondary particulate matter from meteor vapor, *J. Meteor., 18,* 736-745, 1961.

[Röttger and Liu, 1978] Röttger, J., and C. H. Liu, Partial reflection and scattering of VHF radar signals from the clear atmosphere, *Geophys. Res. Lett., 5,* 357-360, 1978.

[Röttger et al., 1988] Röttger, J., C., La Hoz, M. C. Kelley, U.-P. Hoppe, and C. Hall, The structure and dynamics of polar mesosphere summer echoes observed with the EISCAT 224-MHz radar, *Geophys. Res. Lett., 15,*1353, 1988.

[Röttger et al., 1990] Röttger, J., Rietveld M. T., La Hoz C., Hall T., Kelley M. C., and W. E. Swartz, Polar mesosphere summer echoes observed with the EISCAT 933-MHz radar and the CUPRI 46.9-MHz radar, their similarity to 224-MHz radar echoes and their relation to turbulence and electron density profiles, *Radio Sci., 25,* 671, 1990.

[Röttger and La Hoz, 1990] Röttger, J., and C. La Hoz, Characteristics of polar mesosphere summer echoes (PMSE) observed with the EISCAT 224-MHz radar and possible explanations of their origin, *J. Atmos. Terr. Phys., 52,* 893, 1990.

[Röttger, 2002] Röttger, J., Fundamentals of Atmospheric and Ionospheric Radar, *Third International School on Atmospheric Radar/ICTP*, Trieste, Italy, 2002.

[Røyrvik and Smith, 1984] Røyrvik, O., and L. Smith, Comparison of mesospheric VHF radar echoes and rocket probe electron concentration measurements, *J. Geophys. Res., 89,* 9014-9022, 1984.

[Schmidlin, 1992] Schmidlin, F. J., First observation of mesopause temperatures lower than 100 K, *Geophys. Res. Lett., 19,* 1643, 1992.

[Stroud et al., 1959] Stroud, W. G., W. Nordberg, W., Bandeen, W. R., Bartman F. L., and P. Titus, Rocket-grenade observation of atmospheric heating in the Artic, *J. Geophys, Res., 64,*, 1342, 1959.

[Tatarskii, 1971] Tatarskii, V. I., *The Effects of the Turbulent Atmosphere on Wave Propagation, Is. Program for Sci. Transl.,* Jerusalem, 1971.

[Thomas et al., 1989] Thomas, G. E., Olivero J. J., Jensen E. J., Schrőder W., and O. B. Toon, Relation between increasing methane and the presence of ice clouds at the mesopause, *Nature, 338,* 490, 1989.

[Thomas, 1991] Thomas, G. E., Mesospheric clouds and the physics of the mesopause region, *Rev. Geophys., 29,* 553, 1991.

[Thomas et al., 1992] Thomas, L., Astin I., and Prichard I. T., The characteristics of VHF echoes from the summer mesopause region at mid-latitudes, *J. Atmos. Terr. Phys., 54,* 969-977, 1992.

[Thomas, 1996] Thomas, G. E., Is the polar mesosphere the miner's canary of global change?, *Adv. Space Res., 18,* (3) 149-158, 1996.

[Thomas et al., 2003] Thomas, G. E., Olivero J. J., DeLand M., and E. P. Shettle, A response to the Article by U. von Zahn, "Are noctilucent clouds truly a miner's canary for global change?", *Eos, 84 (36),* 352-353, 2003.

[Thrane et al., 1981] Thrane, E. V., Grandal B., Fla T., and A. Brekke, Fine structure in the ionospheric d-region, *Nature, 292,* 221-223, 1981.

[Thrane et al., 1994] Thrane, E. V., Blix T. A., Hoppe U. -P. , Lübken F. -J., Hillert W., Lehmacher G., and D. C. Fritts, A study of small-scale waves and turbulence in the mesosphere using simultaneous in-situ observations of neutral gas and plasma fluctuations, *J. Atmos. Terr. Phys., 56,* 1797-1808, 1994.

[Ulwick et al., 1988] Ulwick J. C., Baker K., Kelley M. C., Balsley B., and W. Ecklund, Comparison of simultaneous MST radar and electron density probe measurements during STATE, *J. Geophys. Res., 93,* 6989-7000, 1988.

[Ulwick et al., 1993] Ulwick J. C., Kelley M. C., Alcala C. M., Blix T. A., and E. V. Thrane, Evidence for two different structuring and scattering mechanisms and the associated role of aerosols in the polar summer mesosphere, *Geophys. Res. Lett., 20,* 2307-2310, 1993.

[von Zahn and Bremer, 1999] von Zahn, U., and J. Bremer, Simultaneous and common-volume observations of noctilucent clouds and polar mesosphere summer echoes, *Geophys, Res, Lett., 26,* 1521-1524, 1999.

[von Zahn, 2003] von Zahn, U., Are noctilucent clouds truly a "miner's canary" for global change?", *Eos, 84,* 261-264, 2003.

[Werne and Fritts, 1999] Werne J., and D. Fritts, Stratified shear turbulence: Evolution and statistics, *Geophys. Res. Lett., 26,* 439-442, 1999.

[Witt, 1962] Witt, G., Height, structure, and displacements of noctilucent clouds, *Tellus, 14,* 1-18, 1962.